

MEMS-Actuated Carbon Fibers

Rachel Zoll



Electrical Engineering and Computer Sciences
University of California at Berkeley

Technical Report No. UCB/EECS-2019-166

<http://www2.eecs.berkeley.edu/Pubs/TechRpts/2019/EECS-2019-166.html>

December 1, 2019

Copyright © 2019, by the author(s).
All rights reserved.

Permission to make digital or hard copies of all or part of this work for personal or classroom use is granted without fee provided that copies are not made or distributed for profit or commercial advantage and that copies bear this notice and the full citation on the first page. To copy otherwise, to republish, to post on servers or to redistribute to lists, requires prior specific permission.

MEMS-Actuated Carbon Fibers

by Rachel S. Zoll

Research Project

Submitted to the Department of Electrical Engineering and Computer Sciences,
University of California at Berkeley, in partial satisfaction of the requirements for the
degree of **Master of Science, Plan II.**

Approval for the Report and Comprehensive Examination:

Committee:

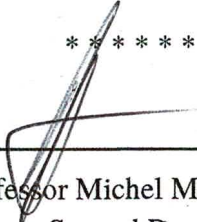


Professor Kristofer S.J. Pister
Research Advisor

5/14/19

(Date)

* * * * *



Professor Michel M. Maharbiz
Second Reader

5/10/2019

(Date)

Abstract

MEMS-Actuated Carbon Fibers

by

Rachel Sara Zoll

Master of Science in Engineering - Electrical Engineering and Computer Sciences
University of California, Berkeley
Professor Kristofer S.J. Pister, Chair

This thesis presents a MEMS actuator capable of extruding or pulling itself along a sub-10 μm diameter carbon fiber. The compact silicon microfabricated MEMS actuator can extrude fibers over many millimeters of distance with micron-level precision and is powered externally via high-voltage control signals.

One specific application demonstrated in this work is the insertion of microelectrodes for cortical neural recording. Microwire and microelectrode arrays used for cortical neural recording typically consist of tens to hundreds of recording sites, but often only a fraction of these sites are in close enough proximity to firing neurons to record single-unit activity. The device is shown to precisely insert a carbon fiber recording electrode to a controllable depth into an agar brain phantom. The device is also capable of recording an artificial neural signal in saline. This technique provides a platform generalizable to many microwire-style recording electrodes which elicit minimal to no adverse biological response.

This ‘extrusion and pulling’ capability may enable microrobots to create the surface on which they move, by carrying around filament and extruding it to form arbitrary shapes with micron-level resolution. Initial work is demonstrated towards the realization of a silicon microrobot which can climb or inch along a pre-existing ‘tightrope’ strut. The final sections of this work discuss the high-level vision and assembly steps needed to integrate MEMS actuators with other MEMS and circuit (CMOS, etc) payloads to realize a fully autonomous inchworm robot that can carry, arbitrarily form, and crawl along its own tether.

Contents

1	Keywords	10
2	Introduction	10
3	MEMS-Actuated Microelectrode for Neural Recording	10
3.1	Background on Neural Recording	10
3.2	Theoretical Insertion Force	12
3.2.1	Motivation for Design Space Exploration	12
3.2.2	Beam Buckling Theory	12
3.2.3	Biological Insertion Forces	14
3.2.4	Effect of Probe Material	15
3.2.5	Effect of Probe Radius	16
3.2.6	Takeaways from Theoretical Insertion Force Analysis	16
3.3	Neural Actuator Design	17
3.3.1	High-Level Design Motivation	17
3.3.2	Choice of Microelectrode Material	17
3.3.3	Choice of Actuator and Comparison to Existing Actuators	17
3.3.4	Force Output and Velocity of Insertion	18
3.3.5	Fiber Insertion	18
3.3.6	Recording	21
3.4	Experimental Methods	23
3.4.1	SOI Fabrication	23
3.4.2	Assembly	24
3.4.2.1	Wiring	24
3.4.2.2	Loading a Fiber	26
3.4.3	Setup for Penetration into Agar	28
3.4.4	Setup for Electrical Impedance Spectroscopy	29
3.4.5	Setup for Recording Dummy Neural Signals	30
3.5	Experimental Results	30
3.5.1	Penetration into Agar	30
3.5.2	Electrical Impedance Spectroscopy	32
3.5.3	Recording of Dummy Neural Signals	34
3.6	Conclusions and Future Work	34
4	Fiber Pusher Characterization and Improvements	35
4.1	Farthest Push in Air	35
4.2	Motivation for Improvements	36
4.3	Angled Arm Optimization	36
4.4	Stationary Gripper Arm	39
4.5	Wirebond Placement	41
5	Inchworm Robot	41
5.1	Electrostatic ‘Inchworm’ Inchworm	41
5.2	Mass and Power Budget	42
5.2.1	Gap Closing Actuator Force Output	42
5.2.2	Solar Cell Operating Points	44

5.2.2.1	Equation 1: IV curve of the solar panel	44
5.2.2.2	Equation 2: $I = CVf$	45
5.2.2.3	Constraint 1: $V > V_{pi}$	46
5.2.2.4	Constraint 2: $f > f_{operate}$	46
5.2.3	Inchworm Motor Integration Operating Points	47
5.3	Suggestions for Integration	48
5.3.1	Crawling with External Power and Control	49
5.3.2	Crawling with On-board Power and Control	50
5.3.3	Ascending and Descending	52
6	Flipchip Bonder	54
6.1	Use Cases	54
6.1.1	Comparison to Wafer Bonding	55
6.1.2	Specific Design Examples	56
6.1.2.1	Prevention of Silicon Out-of-Plane Buckling	56
6.1.2.2	Protection from Debris	57
6.1.2.3	Enclosure for Untethered Silicon Structures	57
6.1.2.4	Containment of Non-Silicon Design Elements	58
6.2	Design Considerations	59
6.2.1	Flipchip Bonder Design Considerations	59
6.2.2	Flipchip Bonder Design Options	62
6.2.2.1	Cover Material	62
6.2.2.2	Cutting Method	62
6.2.2.3	Attach Method	64
6.2.2.4	Flipchip Bonder Attach Tools	64
7	Lessons Learned and Protips	64
8	Future Directions	66
9	Conclusion	66
10	References	67
11	Appendix	71
11.1	Arduino Code and Waveforms	71
11.2	LCR Impedance Measurements	73
11.2.1	Keysight Data Collection Automation	73
11.2.2	MATLAB plotting	74
11.3	Weight and Force Estimates, Inchworm Pusher	76

List of Figures

3.1	The entire neural frontend setup, including the physical electrode implementation (focus of this work), mixed signal frontend, and model for diagnosis and data recording.	11
3.2	Left: Insertion of a microwire array with recording sites at a fixed relative position within the array. Right: Insertion of individual electrodes to independent depths.	11
3.3	Key design parameters of the probe are shown, including E , I , K , and L .	12
3.4	Insertion force vs compression curve for a single neural probe. Reproduced with permission from [1]. Copyright 2018, IOP Publishing.	13
3.5	Illustration of critical buckling regions.	14
3.6	Illustration of critical buckling regions for probes with commonly-used materials.	15
3.7	Illustration of critical buckling regions for probes of different radii.	16
3.8	Left: Equivalent circuit models of the device. During fiber insertion (3.3.5) (top), the electrostatic actuator pushes the fiber forwards in the channel. During recording (3.3.6) (bottom), neural signals are captured by closing all four angled arms until they contact the carbon fiber. Electrically connected segments have been labelled and highlighted. “A”, green, represents the silicon traces and angled arms which contact the carbon fiber; “B”, orange, represents the carbon fiber channel and substrate. Right: Image of the device, with inset shown at bottom.	19
3.9	V_{actuate} , highlighted in yellow, is applied to one set of capacitive fingers.	20
3.10	Silicon angled arms and one set of capacitive fingers are grounded. Green, and highlighted in yellow in both diagrams.	20
3.11	The substrate, highlighted in yellow, is grounded to prevent released silicon structures from electrostatically pulling in to the substrate.	21
3.12	V_{actuate} , in yellow, is maintained across the capacitive fingers such that all four angled arms make contact with the carbon fiber.	21
3.13	The signal pad “A” is used to record the signal.	22
3.14	Substrate and carbon fiber channel (orange, also highlighted in yellow) are left floating.	22
3.15	2-mask SOI fabrication process with two etch steps and a release step.	23
3.16	Die photo of the MEMS actuator next to a US penny. The chip is 4.5 mm x 3.5 mm, and has a mass of 22 mg.	24
3.17	Fully assembled MEMS chip with wired components shown. Included are the interposers, high voltage and ground signal wires, wirebonds, and silver epoxy substrate grounding wire.	25
3.18	Fully assembled MEMS chip with wired components shown. Shown are the interposer, wirebonds, and MEMS chip.	26
3.19	Micromanipulator with inset showing bent, silicone-coated probe tip with carbon fiber attached.	26
3.20	Reference x-y-z axes displayed alongside microscope view of a carbon fiber loaded in the chip.	27
3.21	Left: Microscope view of a carbon fiber loaded into the channel, with reference cross-section A–A’ shown. Middle: Cross-section cartoon of a fiber in the channel. Colors correspond to the SOI fabrication layers as shown in Fig. 3.15. Right: Bird’s eye view SEM of carbon fiber loaded in the channel and gripped by two angled arms.	28
3.22	The MEMS actuator and a 7.2 μm diameter carbon fiber inserted approximately 400 μm into the agar brain phantom.	29

3.23	Diagram depicting the total path impedance components in red. Note that only one of the silicon traces is highlighted in the diagram while in reality there are two traces that form the signal path. Similarly, only one of the four angled arms is highlighted in the diagram while in reality, four angled arms contact the fiber.	30
3.24	The MEMS actuator and a 7.2 μm diameter carbon fiber inserted approximately 400 μm into the agar brain phantom.	31
3.25	Closeup shot of the carbon fiber inserted into agar.	31
3.26	Multiple close-up shots showing the insertion of a 7.2 μm diameter carbon fiber into the brain phantom. The red dash indicates the same position on the carbon fiber between frames.	32
3.27	Electrical impedance spectroscopy for a single electrode. The microelectrode is held in place by two angled arms. Upper plot shows impedance magnitude; lower plot shows impedance phase. Different colors represent different actuation voltages applied to the electrostatic fingers. Impedance is dominated by the resistance of the silicon traces.	33
3.28	Playback of multi-unit activity (blue) is recorded by the carbon fiber microelectrode (red) in 1X PBS. The data was sampled at 125 kHz and a ten sample moving average filter was used to smooth the data.	34
4.1	Fiber extended 1.5 mm and 5.9 mm, respectively.	35
4.2	Fiber extended 7 mm.	36
4.3	Schematic of generic test structure used in optimization of gripper arm geometry. As pictured test structures consist of three primary regions: a Vernier gauge and carbon fiber mounting region, which are identical across all structures, and a test region, which varies based on the property of interest.	37
4.4	Diagram of test regions for each of the four test structures. The spacing between gripping arms, angle at which the arms contact the fiber, thickness of the arms, and pawl widths are tested in separate test structures.	37
4.5	Silver epoxy application to pawl width test structure.	38
4.6	Damage sustained in carbon fiber mounting regions upon gluing failures, as demonstrated in channel spacing and arm angle test structures.	39
4.7	Passivated carbon fiber with exposed tip for recording.	39
4.8	Passive gripping structure, with structure indicated by arrows.	40
4.9	Active gripping structure, with arms, funnel, and motors indicated by arrows.	40
5.1	Cartoon diagram of the carbon fiber inchworm robot.	41
5.2	Cartoon diagram of the carbon fiber inchworm robot inching forwards (or backwards, depending on how you look at it). The external HV signals and control module are not depicted in this diagram.	42
5.3	Theoretical force vs voltage curve for a gap closing actuator with dimensions as listed in Table 4. The operating point at 55 V and 1 mN is annotated by the black lines.	44
5.4	Zappy2 solar cell I-V curve and power curve. The maximum powerpoint of 323 μW at 104 V is indicated by the vertical line.	45
5.5	Frequency operating points which correspond to valid points on the solar cell IV curve.	46
5.6	Frequency operating points which correspond to valid points on the solar cell IV curve.	47
5.7	Free body diagram of the setup.	47
5.8	Carbon fiber suspended from chip, with silicon platform at right.	49
5.9	Carbon fiber glued to silicon platform.	49
5.10	Block diagram showing the electrical connections between the three chips needed to make an autonomous microrobot.	50

5.11	Cartoon diagram of the carbon fiber inchworm robot.	50
5.12	Block diagram showing the electrical connections between the three chips needed to make an autonomous microrobot.	51
5.13	Block diagram showing details of all connections between the three chips.	51
5.14	Concept diagram of mechanisms used for descending. Note the purple sticky pad, gray surface at top, pink area highlighting the actuators, and blue area highlighting the fiber chamber and area for fiber un/furling mechanisms.	53
5.15	Concept diagram of descending.	53
6.1	Left: Cartoon diagram indicating the components and placement of experimental samples in the flipchip bonder. Note the computer monitor displays an overlay of the mylar plastic cover (top substrate) and inchworm motor chip (bottom substrate). Right: Picture diagram indicating the components and placement of experimental samples in the flipchip bonder. The yellow arrow at the right indicates the vacuum-suction pickup arm which will pick up the top substrate. The purple arrow at the left indicates the vacuum base plate where the bottom substrate is positioned.	55
6.2	Left: Picture of vertical fin assembled into rotary slot mechanism. Middle: Layout diagram; gray arrows indicate direction of motion of rotary slot mechanism. Right: An inset of the middle image, with possible coverslip placement over the central pin joint indicated by the blue rectangle.	56
6.3	Left: Single-legged silicon walking robot [2] and silicon screens and linkages used to prevent out-of-plane motion, with possible coverslip placement shown in blue. Right: Silicon walking hexapod [2], with possible coverslip placement shown in blue.	57
6.4	Left: The silicon jumper with possible coverslip placement shown in blue.	57
6.5	Example of an untethered structure and possible coverslip placement (shown in blue) to prevent untethered structure from floating away.	58
6.6	Dried polyacrylamide is hydrated inside a silicon channel. The silica cover, highlighted in blue, contains the liquid hydrogel inside the silicon channel. Reproduced and modified with permission from [3].	58
6.7	A carbon fiber travels within the silicon channel. The mylar cover, shown in blue, prevents the carbon fiber from falling out of plane and exiting the channel.	59
6.8	Representative image of a coverslip placed and attached to a silicon die with UV cureable epoxy. Relative size of the glue dabs is indicated by the white arrows.	60
6.9	Zoom-in shot of a coverslip placed and attached to a silicon die with UV cureable epoxy. Note the glue wicking into nearby silicon traces and electrostatic actuator fingers.	60
6.10	Left: A cover is placed at a 0° orientation. Right: A cover is placed at a 45° rotation to cover the entirety of the motors. Note that a trapezoidal-shaped coverslip may have been more ideal in this case, as it is difficult to place the rectangular-shaped coverslip without covering the wirebond pads.	61
6.11	Left: The smaller coverslip ruins visibility of devices which are directly under the edge of the coverslip, highlighted in red. Right: The larger coverslip is placed such that its edge, highlighted in green, only impedes visibility of dummy silicon area. Note the microscratches on the cover surfaces in both images.	61
6.12	Left: 5mil mylar film flipchip bonded onto silicon. Right: 2mil kapton flipchip bonded onto silicon.	62

6.13	Left: Tolerance test cut patterns. “c”, “s”, and “e” refer to the laser cutter’s different cutting styles: vector <u>c</u> ut (red), vector <u>s</u> core (black), and raster <u>e</u> ngrave (blue). Right: Results of using the laser cutter with the tolerance cut patterns. Only the vector cut singulated coverslips entirely.	63
6.14	Double-sided tape helps to keep the plastic in place while the laser cutter and vacuum are on. It also helps to keep the coverslips from floating away after they’ve been cut. Left: 1.2 mm x 1.5 mm coverslips on 5mil mylar. Right: 1.2 mm x 1.5 mm coverslips on 2mil kapton.	63
7.1	Example inventory of one set of chips.	65
11.1	Waveforms produced by the arduino code. Note the anti-phase between Channel 1 and Channel 2, which have a frequency of 15 Hz.	71

List of Tables

1	Insertion forces for various biological tissues	15
2	Comparison of commonly used neural probe materials and their Young’s moduli	16
3	Comparison to existing actuator mechanisms	18
4	Geometry of the gap closing actuator array	43
5	Nominal gap closing actuator operating forces at 55V	43
6	Mass and force requirements for autonomous microrobot	48

Acknowledgements

This work would not have been possible without the help of many who have supported me throughout my studies.

I would like to thank the UC Berkeley EECS Department, the Berkeley Sensor & Actuator Center, and the Chan Zuckerberg Biohub for providing funding during this project. All fabrication was performed at the UC Berkeley Marvell Nanolab. Thank you also to the members of the EECS staff, particularly **Shirley Salanio**, **Susanne Kauer**, **Audrey Sillers**, and **Nicole McIntyre**. The BWRC and BSAC staff members, particularly **Candy Corpus**, **James Dunn**, and **Richard Lossing**, also provided support and guidance.

First and foremost, I would like to thank my primary advisor, **Professor Kristofer Pister**, for his endless enthusiasm, thoughtfulness, and belief in the innate curiosity and abilities of every student. Without him, this journey likely would never have started. I would also like to thank my other faculty advisors, **Professor Michel Maharbiz** and **Professor Rikky Muller**, for providing technical guidance, advice on how to improve my research process, and ideas on a myriad of topics.

Thanks also goes to **Professor Vladimir Stojanovic** for allowing me to join his research group while I was still gaining my research legs as an undergraduate. **Professor Babak Ayazifar** was tremendously supportive and creative in helping me to brainstorm my career trajectory.

Fellow colleagues **Craig Schindler** and **Travis Massey** helped me carve out a meaningful research path, and were always willing to lend an ear whenever I had problems. I would like to acknowledge **Craig Schindler** for helping to read drafts and brainstorm new ideas, and **Aniket Tolpadi** for allowing me to include a portion of our results together in the “Fiber Pushers improvements” section.

More senior Pister lab members of the jumping, flying, walking, and swimming kinds - **Joseph Greenspun**, **Daniel Drew**, **Daniel Contreras**, **Hani Gomez**, **Brian Kilberg**, **Nathan Lambert**, and **Ryan Shih** - helped design intelligent ways to fabricate and interact with robots on a small scale, and graciously shared that wisdom with me.

Thank you also goes to Pister lab members of the circuit variety - **Fil Maksimovic**, **Brad Wheeler**, **David Burnett**, **Lydia Lee**, **Alex Moreno**, and **Osama Khan** - who were always willing to lend a hand (or brain) to debug issues. Their sense of humor has kept me on my toes.

Many students from the Maharbiz lab and BWRC were also present and willing to offer design insights from a different angle - **Konlin Shen**, **David Piech**, **Oliver Chen**, **Alyssa Zhou**, **Tom Zajdel**, **Mauricio Bustamante**, and **Jordan Edmunds**.

My parents, **Michael Zoll** and **Judith Zoll**, along with our slowly rotating crew of cats and dog(s), have been instrumental in providing me with a loving and supportive environment.

Last but not least, thanks goes to **Edward Wang**, who has always encouraged me to think outside the box and to appreciate life for all that it is. Thanks for going on roadtrips to just about everywhere with me. Onwards to our next adventure!

1 Keywords

Carbon fiber, MEMS actuators, silicon microrobots, neural recording, microelectrodes

2 Introduction

Micro-electro-mechanical systems (MEMS) are systems consisting of miniaturized mechanisms controlled and driven by electrical circuits. Popularized in the popular imagination as “nanotechnology”, MEMS systems are ubiquitous in our everyday lives in the form of sensors such as accelerometers and gyroscopes.

The type of MEMS mechanism that will be presented in this thesis is a mechanism for actuating (pushing/pulling) carbon fibers. This mechanism enables micron-scale, fine-grained control of thin carbon fibers. Manipulation of fibers at this scale unlocks applications in neural recording, arbitrary movement of microrobots in free space, and beyond.

Microwire and microelectrode arrays used for cortical neural recording typically consist of tens to hundreds of recording sites, but often only a fraction of these sites are in close enough proximity to firing neurons to record single-unit activity. Recent work has demonstrated precise, depth-controllable mechanisms for the insertion of single neural recording electrodes, but these methods are mostly only capable of inserting electrodes which elicit adverse biological response. We present an electrostatic-based actuator capable of inserting individual carbon fiber microelectrodes which elicit minimal to no adverse biological response. The device is shown to insert a carbon fiber recording electrode into an agar brain phantom and can record an artificial neural signal in saline. This technique provides a platform generalizable to many microwire-style recording electrodes.

While previous work has focused on jumping [4], flying [5], and walking microrobots [2], an interesting class of microrobots that hasn’t been actively explored are microrobots that create the surface on which they move. Microrobots could build useful structures in which they later move around, much like a spider [6]. Similar to how spiders produce different types of silk depending on the application, a microrobot could build arbitrary structures out of different materials that are sticky, dry, hydrophobic/philic, elastic, etc. The microrobot could first deploy a structural support, followed by additional structures with different material properties.

The rest of this thesis will be organized as follows. Section 3 discusses the applications, theory, design, and results of a MEMS-actuated microelectrode for neural recording. Section 4 discusses design optimizations of the classic inchworm motor that are specific to fiber pusher applications. Section 5 introduces a new microrobot application for the fiber pusher platform, including mass and power budget calculations and suggestions for future integration with control and power circuitry. Section 6 discusses the use of a flipchip bonder specifically for MEMS structures, and includes a thorough analysis of different use cases, design considerations such as the bonding material and attachment method, and specific suggestions to achieve successful bonds. Finally, sections 7,8, and 9 conclude the thesis and explain future work and high-level lessons learned.

3 MEMS-Actuated Microelectrode for Neural Recording

3.1 Background on Neural Recording

Intracortical microelectrodes for neural recording are a powerful tool for capturing the activity of individual neurons, enabling further understanding of neural patterns that could indicate underlying disease, aid in fundamental neuroscience research, and enable brain-machine interface technologies.

At a high level (see Fig. 3.1), the entire intracortical microelectrode recording setup consists of a physical electrode, mixed signal frontend amplification hardware, conversion to the digital domain, and diagnosis with a machine model or by a physician.

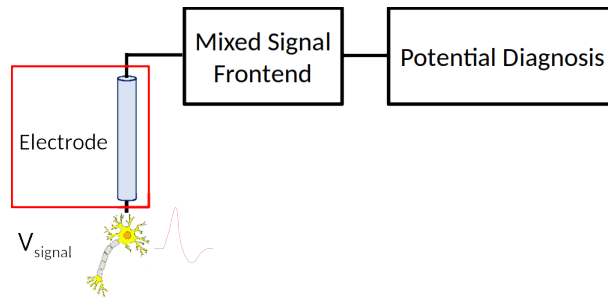


Figure 3.1: The entire neural frontend setup, including the physical electrode implementation (focus of this work), mixed signal frontend, and model for diagnosis and data recording.

The implantation depth of an electrode affects the quality of the recorded data. Current state-of-the-art electrode arrays consist of several tens to hundreds of recording sites [7–10]. Neural recording arrays are typically implanted to a target depth in a given region of interest. Minor adjustments are then made to the array’s depth or position to maximize the number of recorded units across the array; still, many sites may not detect active units. Devices such as the Utah array and tungsten microwire arrays are limited in that all recording sites are at a fixed relative position within the array (see Fig. 3.2, left). Upon implantation, individual recording sites cannot be independently inserted to unique depths to maximize recorded unit activity on each electrode [11, 12].



Figure 3.2: Left: Insertion of a microwire array with recording sites at a fixed relative position within the array. Right: Insertion of individual electrodes to independent depths.

The choice of electrode material also affects the recorded signal quality as well as the biological response [13]. Recent work has suggested that recording electrodes with cross-sections on the order of single-digit microns do not show significant evidence of neuronal loss, gliosis, or macrophage activation [8, 14–17]. Several carbon fiber microwire neural recording arrays have been developed with electrodes on such a scale, but none yet affords independent depth control of individual recording electrodes [9, 18–20].

Hence, an ideal recording platform would enable actuation of implanted electrodes with small cross-sections (such as carbon fibers) to independent depths in order to maximize signal-to-noise ratio (SNR) or until an otherwise desirable spiking unit is located [21] (see Fig. 3.2, right). During initial

electrode placement, these microdrives may alternate between inserting and recording neuronal activity from the electrode, providing surgeons with real-time feedback indicating optimal placement depth [22, 23].

We report an electrostatic-based MEMS carbon fiber actuator capable of inserting electrodes to a variable depth with $1\ \mu\text{m}$ - $2\ \mu\text{m}$ precision. This mechanism is capable of inserting $7.2\ \mu\text{m}$ carbon fiber recording electrodes which do not elicit glial scarring [8, 14]. Although this work demonstrates insertion of single electrodes, the electrostatic actuator mechanisms could be fabricated as arrays, enabling increased channel count. The actuators are controlled via a set of voltage signals generated using an Arduino Uno.

Knowledge gained through use of this technology can help inform further therapeutic assessments and decisions made by the medical community. This insertion mechanism could also be used by researchers investigating the peripheral nervous system (PNS), by informing our understanding, characterization, and treatment of damage.

3.2 Theoretical Insertion Force

3.2.1 Motivation for Design Space Exploration

Before we dive more into the experimental setup and specific design parameters, it is helpful to first discuss the probe design tradeoffs at a high level. What makes a good probe? How do design choices such as the probe length, material, and radius affect how easily the probe will insert into biological tissues? How stiff are biological tissues? How does this stiffness vary across different neural regions? When does a probe break?

3.2.2 Beam Buckling Theory

To calculate the critical buckling force of a given beam, we use Euler’s critical load formula, Eq. 1. This formula specifies the maximum amount of force that can be applied to a beam before it will buckle or deform laterally. The key parameters are the Young’s modulus of the material (E), the probe’s 2nd moment of area or ‘area moment of inertia’ (I), its effective length factor which depends on the beam end constraints (K), and the unsupported beam length (L). Note that we use the terms ‘probe’ and ‘beam’ interchangeably in these sections, as they both refer to the microelectrode of interest. These parameters are shown in Fig. 3.3.

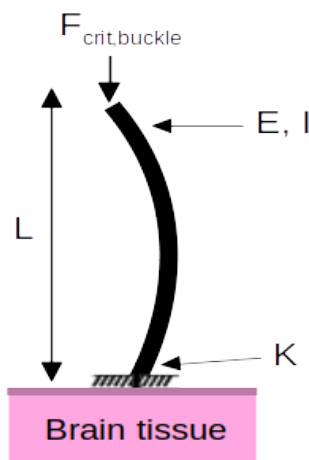


Figure 3.3: Key design parameters of the probe are shown, including E , I , K , and L .

$$F_{\text{crit,buckle}} = \frac{\pi^2 EI}{(KL)^2} \quad (1)$$

Plugging in for the 2nd moment of area of a cylindrical electrode along the radial direction, and setting $K = 2$ under the assumption that the beam has fixed-free boundary conditions as in [14] and [18], we derive Eq. 2. Note that the beam's weight is assumed to be negligible. The beam's cross-sectional area (factored into the calculation of I) is assumed to be constant along the length of the beam.

$$F_{\text{crit,buckle}} = \frac{\pi^2 EI}{(KL)^2} = \frac{\pi^2 E(\frac{\pi}{4}r^4)}{(KL)^2} = \frac{\pi^3 Er^4}{16L^2} \quad (2)$$

Realistically, L is probably a more complex function depending on the depth of the probe in the brain. Given how our particular beams (carbon fibers) function in practice, a fixed-guided boundary condition for K might be more accurate, as tissue dimpling means the fiber is no longer free to move laterally at the contact point (i.e. the fiber is constrained to being upright due to tissue dimpling).¹

With the knowledge that $F_{\text{crit,buckle}}$ varies as $\frac{1}{L^2}$, it is best to minimize the unsupported beam length, i.e. the distance from the actuation force to the tissue. The beam will insert into tissue if the maximum compression force it can withstand before bending (its $F_{\text{crit,buckle}}$) is larger than the force required to penetrate the tissue (F_{insert}). Similarly, the beam will buckle as opposed to inserting if its maximum compression force $F_{\text{crit,buckle}}$ is less than the tissue penetration force, F_{insert} . Assuming the probe doesn't buckle upon insertion, F_{insert} also represents the amount of force that the actuator must be able to produce and translate to the probe to overcome the tissue resistance.

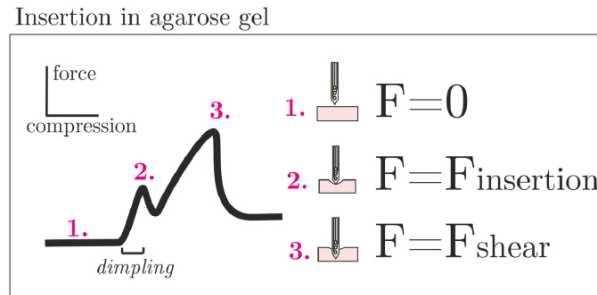


Figure 3.4: Insertion force vs compression curve for a single neural probe. Reproduced with permission from [1]. Copyright 2018, IOP Publishing.

As discussed in [1, 24], the greatest force that a probe must withstand is during insertion. As shown in Fig. 3.4, once the probe successfully dimples and then penetrates the tissue, there is a precipitous drop in shear force (label 2). The shear force gradually increases again as the probe is inserted deeper into the tissue (label 2-3). Eventually the probe buckles and breaks within the tissue. In this section, we focus on the insertion force required to penetrate the tissue.

¹Thanks to **Travis Massey** and **David Piech** for their comments on the interpretation of K .

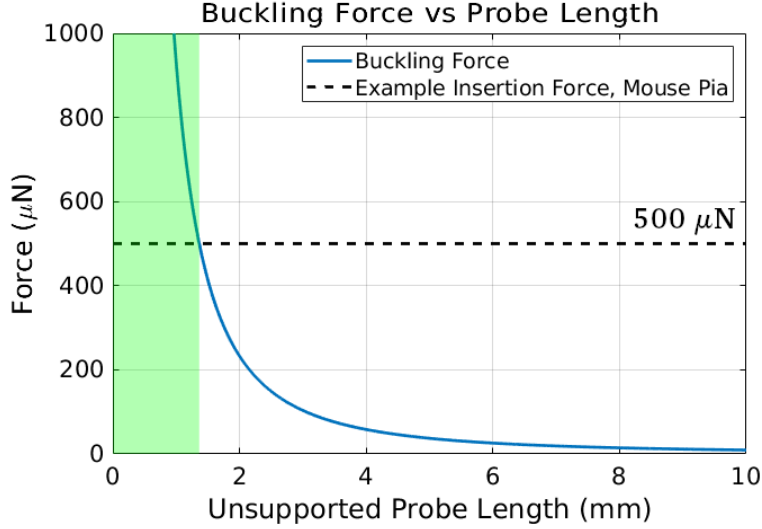


Figure 3.5: Illustration of critical buckling regions.

To demonstrate the required forces graphically, we use Fig. 3.5 as an example. On the y-axis is the maximum compression force that the probe can withstand, $F_{\text{crit,buckle}}$, and on the x-axis is the probe’s unsupported length. The solid blue line represents the buckling force of a $7\ \mu\text{m}$ radius probe with Young’s modulus of 200 GPa. The black horizontal dashed line represents a realistic mouse pia penetration force of $500\ \mu\text{N}$. Everywhere where the probe will insert rather than buckle is shaded in green. The probe will buckle for unsupported probe lengths to the right of the shaded region. We see that the maximum unsupported probe length for this probe is $1.7\ \mu\text{m}$.

Now that we’ve analyzed a probe with unsupported length L , radius r , and Young’s modulus E , we can analyze how a given probe might interact with various biological tissues, each with different insertion force F_{insert} .

3.2.3 Biological Insertion Forces

The forces required to penetrate the dura mater, pia mater, and white and grey matter, are listed in the summary table (see Table 1). These values provide a very rough estimate of the insertion forces required to penetrate through key regions. Note that they are still highly variable even for the same region, i.e. rat pia. The measurements do not account for more localized inhomogeneities and non-idealities in tissue structure. An example of how to make these tissue insertion force measurements can be found in [25], where force load cells were attached to microelectrodes. The microelectrodes were then implanted by a computer-controlled micromanipulator, and the forces simultaneously recorded.

Also note that the dura is typically incised during surgery and would not need to be penetrated by an electrode or actuator.

Table 1: Insertion forces for various biological tissues

Animal Model	Region inserting into	F_{insert} (mN)
1 Human [26]	Gyri (already incised pia)	0-50
2 Rat [25]	Pia	0.62
	Further insertion, gray matter (<2 mm)	0.87 (compressive force)
	Fully advanced, constant depth	0.5
	Retraction	0.54 (tensile force)
3 Rat [27]	Breaking dura	28.0 ± 14.4
	Breaking pia	1.53 ± 0.67
4 Phantom (agarose gel & polyethylene foil pia & dura mater) model of cow and lamb [28]	In vitro, in vivo pia & dura	40 (avg. over all materials)

3.2.4 Effect of Probe Material

We now turn to a different design variable, the probe material. To better understand how the probe’s material affects its ability to penetrate the grey matter, we analyze five common probe materials: polyamide, glass, silicon, carbon fiber, and tungsten. Each has a distinct modulus of elasticity, and all are considered to be relatively biocompatible. Note that it would not be feasible to fabricate these probes to have exactly identical geometries (circular cross-sectional, radius, thickness, etc), due to limitations in fabrication methodologies [28].

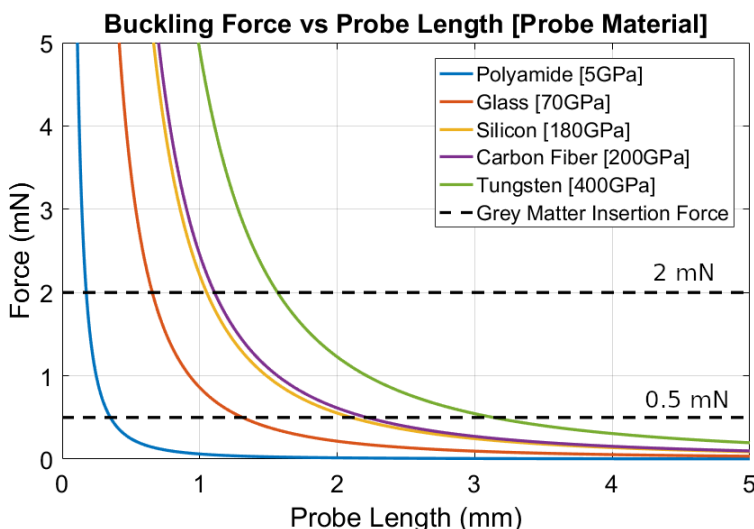


Figure 3.6: Illustration of critical buckling regions for probes with commonly-used materials.

In Fig. 3.6 we demonstrate the maximum compression forces for each of the probes, each of radius $4.7 \mu\text{m}$. Each of the colored lines represent a different probe material. For the fixed-radius

probes, the tungsten probes are able to withstand the most force before buckling. As can be seen in Table 2, the polyamide probe’s modulus of elasticity (5 GPa) most closely matches that of the pia mater (100 MPa) [28].

While this analysis provides a good high-level intuition of the buckling forces each probe is able to withstand, in reality, we use carbon fiber probes for reasons discussed in the [neural pusher background \(3.1\)](#) and [design requirements \(3.3.1\)](#) sections.

Table 2: Comparison of commonly used neural probe materials and their Young’s moduli

Probe Material	Young’s Modulus (GPa)
Polyamide	5
Glass	70
Silicon	180
Carbon Fiber	200
Tungsten	400

3.2.5 Effect of Probe Radius

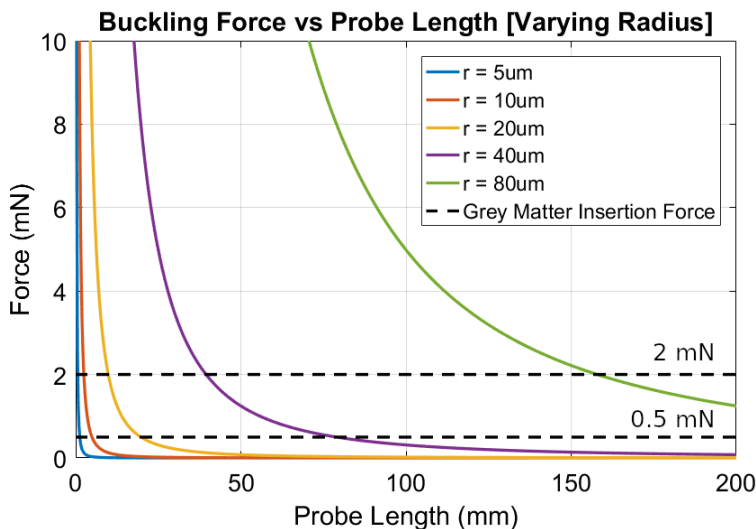


Figure 3.7: Illustration of critical buckling regions for probes of different radii.

Similarly, by increasing the probe radius, it is possible to design a probe with lengths approaching those required for deep brain stimulation (DBS) applications (around 10 cm-50 cm). For instance, a 160 mm-long probe (16 cm) with $E=200$ GPa and $r=80 \mu\text{m}$ is able to withstand the required 2 mN of insertion force (Fig. 3.7). Since the force required to buckle a probe decreases by a power of four with respect to increasing radius, probe radius is a very effective design parameter.

Increasing the probe radius is a design parameter which trades off between recording resolution across the area of interest and probe length.

3.2.6 Takeaways from Theoretical Insertion Force Analysis

From this section, we learned that the ideal beam, or microelectrode, would have higher Young’s modulus, larger radius, and a shorter unsupported length to avoid buckling. However, some of these

requirements are in opposition to the goal of recording across a large area of biological tissue while causing minimal tissue damage. For instance, the ideal microelectrode would have lower Young’s modulus to match more closely with that of the tissue, and a smaller radius to cause less tissue damage. In the next section we will discuss the probes that were ultimately chosen for this work. We will also discuss the actuators used to advance the probes into biological tissue.

3.3 Neural Actuator Design

3.3.1 High-Level Design Motivation

At a high-level, our actuator should be capable of inserting a biocompatible electrode that causes little to no adverse biological response. The actuator should also be capable of inserting the electrodes with micron-level precision so that they are able to record from target structures on a given neuron. The next few subsections of thesis will go into detail about the choice of microelectrode material and actuator.

3.3.2 Choice of Microelectrode Material

The ideal microelectrode material would be biocompatible and minimally damaging to biological tissue. In this work we chose to use carbon fiber electrodes, which have previously been shown to elicit minimal adverse biological response [8, 14, 19]. Tissue histologies following a two-week implantation of carbon fiber electrodes in tissue show that these carbon fiber microelectrodes, of diameter less than 10 μm , have significantly reduced neuronal loss, gliosis, and macrophage activation as compared to traditional silicon electrodes [14]. The reduction in tissue damage can be attributed to the reduction in electrode diameter as well as improved matching of the electrode Young’s modulus to that of biological tissue. Our carbon fibers were 7 μm in diameter, as that was what was readily available commercially. Other works have used custom-fabricated carbon fiber electrodes and are able to achieve even smaller diameters.

3.3.3 Choice of Actuator and Comparison to Existing Actuators

Recent studies have demonstrated fluidic, DC microdrive, thermal, and electrostatic microactuators capable of inserting 12 μm -150 μm diameter electrodes with depth precision ranging from 1 μm -25 μm [22, 23, 29–32]. Only Vitale et al.’s work demonstrates insertion of electrodes sufficiently fine to minimize the adverse biological response; however, their fluidic pumps could make insertion of large quantities of electrodes difficult [29]. In comparison with thermal actuators, the actuation method presented here does not exhibit any thermal heating [23]. Although Otchy et. al’s microdrive system was able to achieve 1 μm depth precision, each microelectrode in the implanted tetrode is 200 μm in diameter and unable to be independently placed apart from each of the other microelectrodes within the tetrode [32, 33].

Table 3 presents a comparison between these actuators and the electrostatic actuator designed in this work. Presented are the probe diameter, step resolution, maximum vertical displacement of the recording probe, and estimated volume of the actuator assembly that would be in close contact with the biological tissue during insertion. Of particular interest for this work are the probe diameter and step resolution. The step resolution of the electrostatic actuator we designed (1 μm -2 μm) is sufficiently small to target individual structures on a given neuron. The maximum displacement of the probe is still large enough to be able to target many different sub-populations of neurons.

Table 3: Comparison to existing actuator mechanisms

Actuation Type	Probe \varnothing (μm)	Step resolution (μm)	Max displacement (mm)	Volume (mm^3)
Fluidic [29]	12	16	4.5	36
DC microdrive [32]	~ 75	unknown	5	78
Thermal [23, 34]	~ 50	8.8	2	0.6
Electrostatic [22]	50	1	2	0.8
Electrostatic - this work	7.2	1-2	0.4-7.0	2.2

3.3.4 Force Output and Velocity of Insertion

The force and velocity of insertion can be controlled depending on the application. Previous literature shows that the insertion speed does not result in a difference in tissue damage, although these results differ drastically depending on the region of insertion [35]. For details on how the operating voltage and frequency affect the force and velocity of insertion, refer to the section on [mass and power budget](#) (section 5.2).

3.3.5 Fiber Insertion

We designed a MEMS actuator containing an electrostatic motor with angled arms, as in [36, 37]. The electrostatic motors presented here are capable of producing millinewton forces over many millimeters of travel [36–39], sufficient for the penetration forces (calculated to be on the order of hundreds of micronewtons for this electrode style) and depths necessary for most applications [8, 9, 14]. In prior work, these actuators have been used to advance 7.2 μm carbon fibers in air, but have not been characterized for their mechanical insertion and electrical characteristics in the context of neural recording [37].

Each actuation cycle of the electrostatic motor pushes the fiber a small distance. Motion is achieved by applying voltage to an interdigitated set of capacitive fingers. Initially, one set of fingers is grounded, while the other set is held at V_{actuate} . This electrostatic force causes the interdigitated capacitive fingers to pull in towards one another, in turn pushing out a set of flexible angled arms which grip the carbon fiber. To disengage the flexible arms from the carbon fiber, both sets of capacitive fingers are grounded and a spring pulls the capacitive fingers apart.²

By using two such actuators to perform a cyclic motion in which the angled arms come into contact with the carbon fiber, move it forwards one step, disengage, and return to their initial position, the motor accumulates small steps which eventually advance the microelectrode over a large distance. For more details on actuation, see [36].

Thinking about this insertion sequence more abstractly, the process is similar to that of a person climbing a vertical hanging rope at a gym. Initially, the climber’s hands are both gripping the rope. Next, the climber releases one hand from the rope and places it higher on the rope. This process is repeated many times until eventually the climber reaches the top of the rope.

Fig. 3.8 shows equivalent circuit diagrams (left) and corresponding images of the device (right) with electrically connected segments labelled and highlighted. In these diagrams, the green highlighted regions indicate the signal path from the wirebond pads, through the silicon traces, to the

²Please refer to the [appendix \(11.1\)](#) for the Arduino code and corresponding waveform outputs used to drive the electrostatic motors.

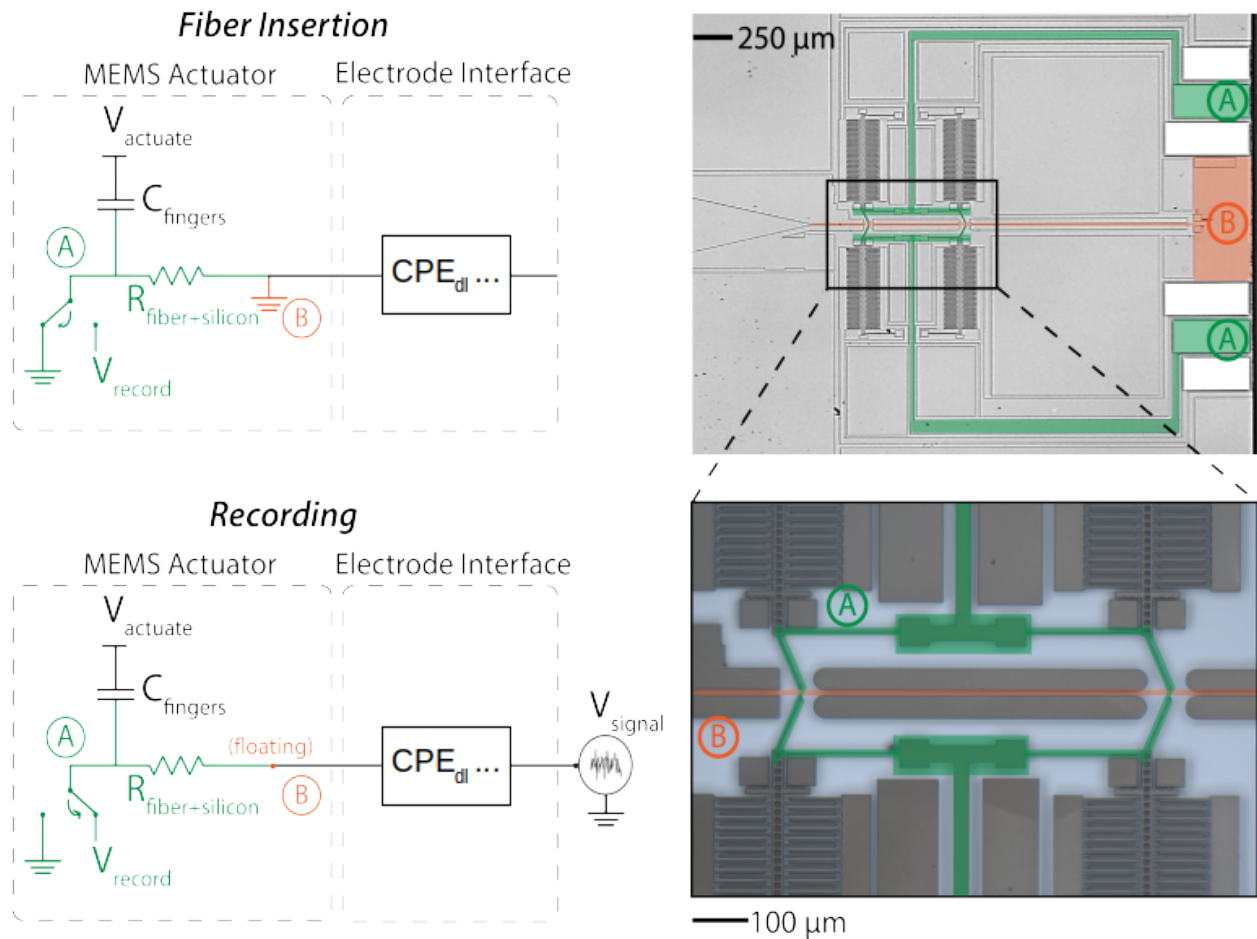


Figure 3.8: Left: Equivalent circuit models of the device. During **fiber insertion** (3.3.5) (top), the electrostatic actuator pushes the fiber forwards in the channel. During **recording** (3.3.6) (bottom), neural signals are captured by closing all four angled arms until they contact the carbon fiber. Electrically connected segments have been labelled and highlighted. “A”, green, represents the silicon traces and angled arms which contact the carbon fiber; “B”, orange, represents the carbon fiber channel and substrate. Right: Image of the device, with inset shown at bottom.

angled arms which contact the carbon fiber. The orange highlighted regions indicate the substrate connection and location of a carbon fiber within the channel. The bottom right insets show the silicon traces and angled arms (green) which come in contact with the fiber, nominally held in place in the fiber channel (orange). When no voltage is applied to the actuator motor, the carbon fiber is not in contact with any silicon structure other than the substrate.

During insertion of a fiber, one set of capacitive fingers alternates between $V_{actuate}$ and ground, dictating whether the angled arms are in contact with or disengaged from the carbon fiber (Fig. 3.9).

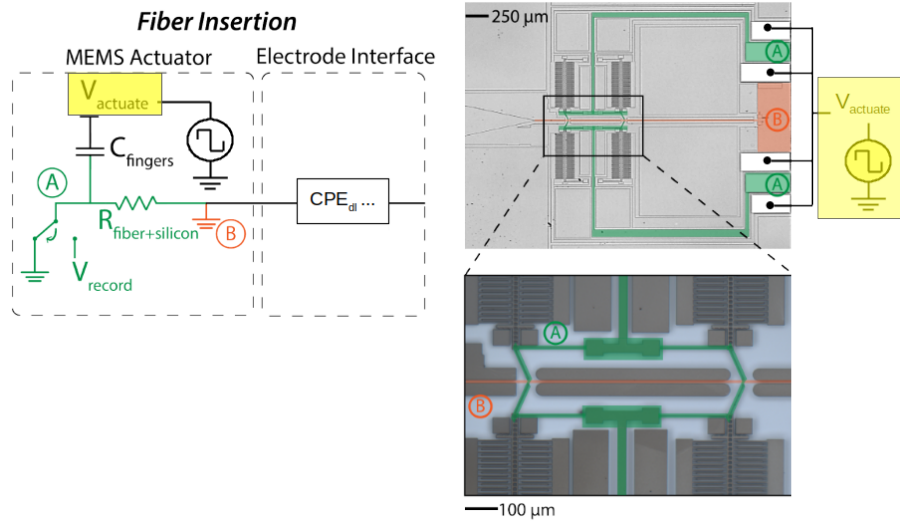


Figure 3.9: $V_{actuate}$, highlighted in yellow, is applied to one set of capacitive fingers.

The silicon angled arms and the other set of capacitive fingers in each actuator are tied to ground to enable proper operation of the motors (highlighted in green, “A”, Fig. 3.10).

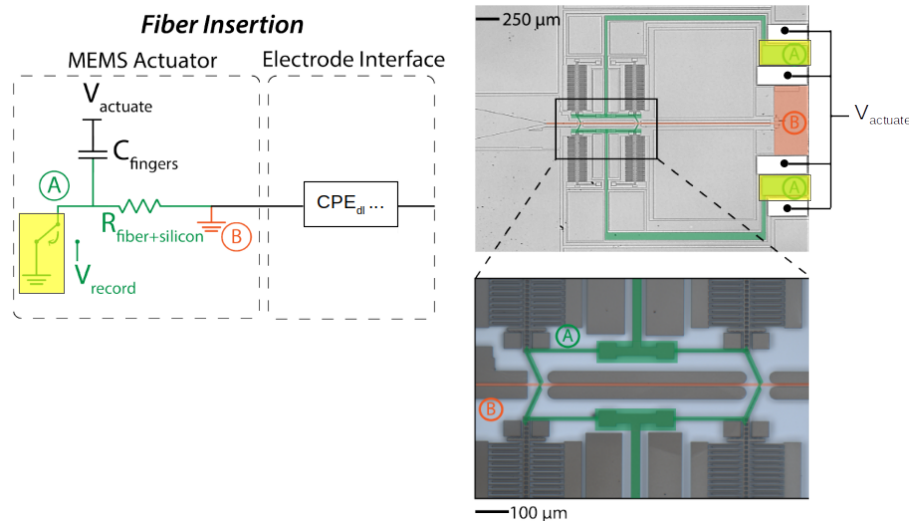


Figure 3.10: Silicon angled arms and one set of capacitive fingers are grounded. Green, and highlighted in yellow in both diagrams.

The substrate (highlighted in orange, “B”) is also grounded to prevent released silicon structures

from electrostatically pulling in to the substrate (Fig. 3.11). We are aware that this node (orange, “B”) must always be kept away from the instrumentation nodes so that there is no leakage path for current into biological tissue.

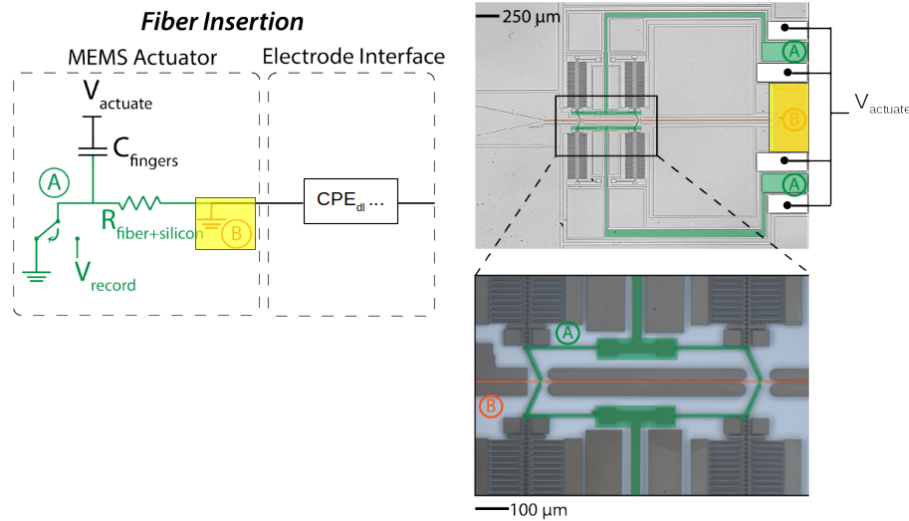


Figure 3.11: The substrate, highlighted in yellow, is grounded to prevent released silicon structures from electrostatically pulling in to the substrate.

3.3.6 Recording

When recording signals from the electrode (Fig. 3.12), all four angled arms make contact with the carbon fiber when a high voltage, V_{actuate} , is maintained across the capacitive fingers. These silicon arms, along with the corresponding silicon routing, form a signal path with which to record the neural signal.

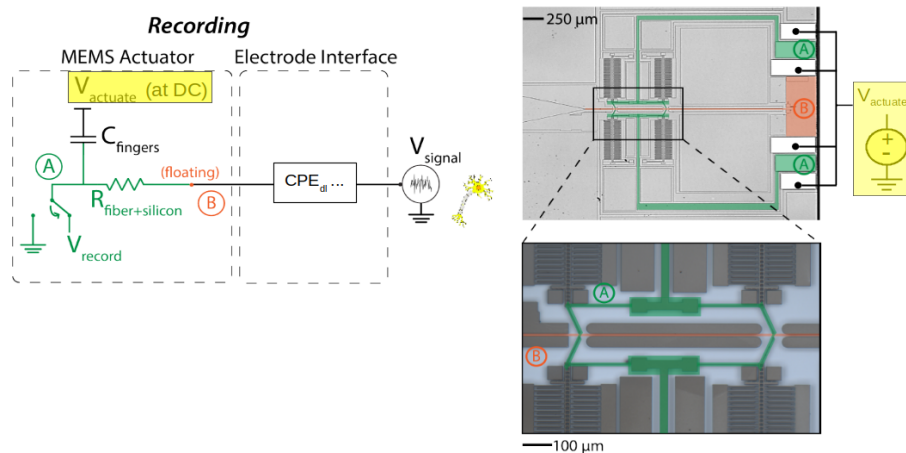


Figure 3.12: V_{actuate} , in yellow, is maintained across the capacitive fingers such that all four angled arms make contact with the carbon fiber.

The path of impedance for this signal, from the tip of the carbon fiber in contact with the electrolyte to the external sensor circuitry wire-bonded to the die, includes: double-layer constant

phase element CPE_{dl} at the electrode-electrolyte interface; carbon fiber impedance $R_{\text{fiber+silicon}}$; contact resistance between the carbon fiber and silicon angled arms; silicon traces; and wire bonds (all included in $R_{\text{fiber+silicon}}$).

The electrophysiological potential is recorded from the signal pad (green, “A”) versus a reference electrode (Fig. 3.13).

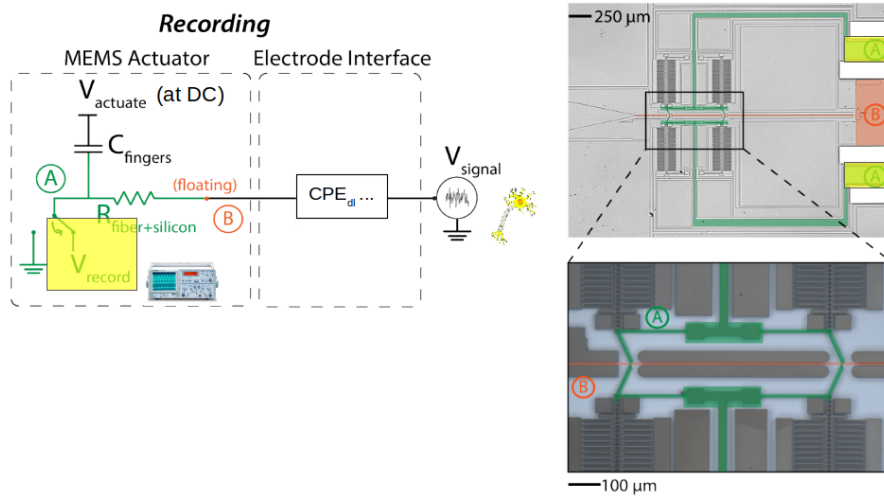


Figure 3.13: The signal pad “A” is used to record the signal.

The substrate and carbon fiber channel (orange, “B”) are left floating to prevent grounding of the recorded signal (Fig. 3.14). Although the voltage difference between the sets of capacitive fingers becomes $V_{\text{actuate}} - V_{\text{signal}}$ due to the micro-to-millivolt amplitude of neural recordings, this voltage is still sufficient to allow the angled arms to grip the fiber.

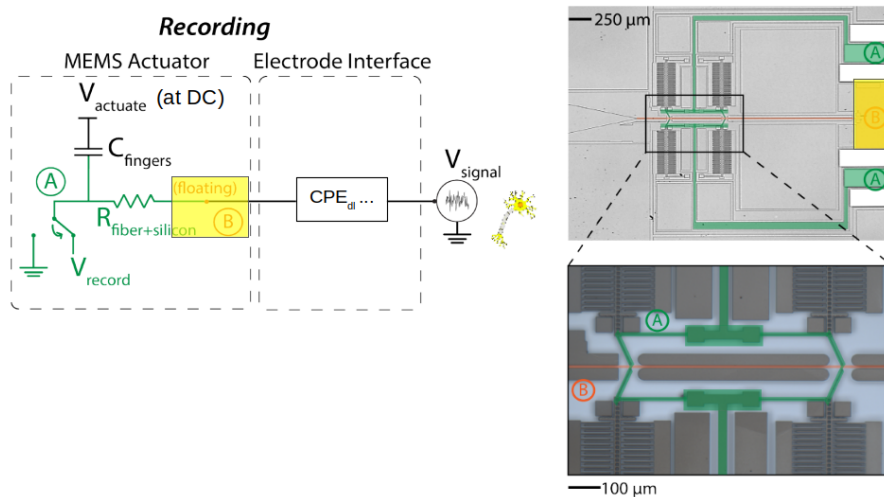


Figure 3.14: Substrate and carbon fiber channel (orange, also highlighted in yellow) are left floating.

3.4 Experimental Methods

3.4.1 SOI Fabrication

The MEMS actuator was fabricated with a two-mask silicon-on-insulator (SOI) process (Fig. 3.15). Commercial SOI wafers consisting of a silicon substrate (550 μm), buried oxide layer (2 μm), and a device silicon layer (40 μm , 3250 Ω/\square), were used for all devices. First, aluminium was evaporated onto the wirebond sites to improve bond adhesion. Device silicon was lithographically patterned and etched using a deep reactive ion etch (DRIE). A subsequently patterned through-etch of the silicon substrate layer, also via DRIE, served to singulate the devices. Finally, a timed vapor HF etch was used to release the structures. The fabrication process steps are shown in Fig. 3.15, and the resulting fabricated device is shown next to a penny for size comparison in Fig. 3.16.

The resulting chip is 4.5 mm by 3.5 mm, and has a mass of 22 mg. The actuator/motor area is approximately 1.5 mm².

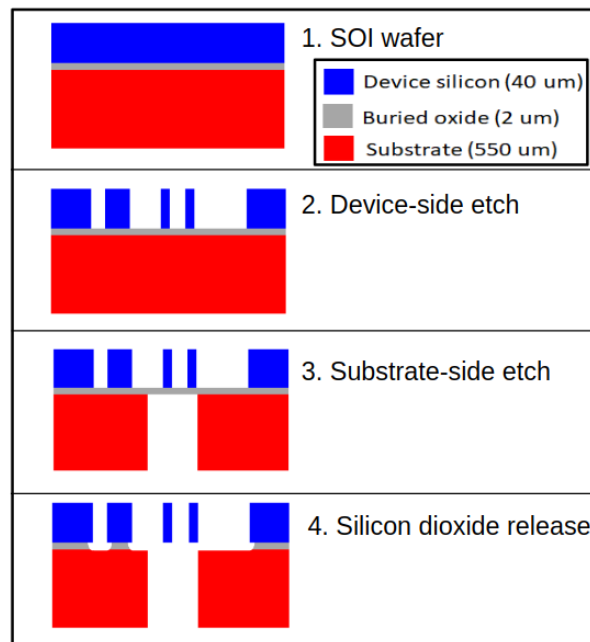


Figure 3.15: 2-mask SOI fabrication process with two etch steps and a release step.

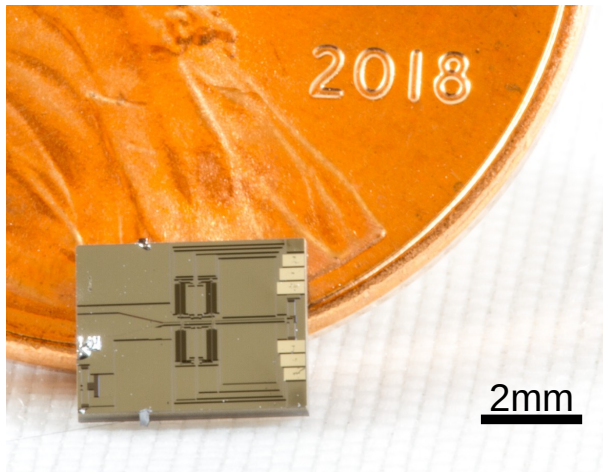


Figure 3.16: Die photo of the MEMS actuator next to a US penny. The chip is 4.5 mm x 3.5 mm, and has a mass of 22 mg.

3.4.2 Assembly

3.4.2.1 Wiring Although it would be possible to perform these steps out-of-order, it is easiest to follow the sequence described below as it has been proven to work. The fully assembled MEMS chip is shown in Fig. 3.17. A closer view of the fully assembled MEMS chip is shown in Fig. 3.18.

1. Cut a sample carrier to size. For my setup, I cut a glass slide down to 3 cm by 10 cm. I would suggest using something that's easier to cut, such as clear acrylic which could be cut in a laser cutter. With this option, you could also etch in placemarkers for where the chip and interposer should be glued.
2. Solder wires to the interposer.³ For these motors you'll need two high voltage wires and a ground wire for the actuators. Later you'll affix the substrate grounding wire to the silver epoxy. For each solder joint, be sure to leave some exposed metal area so there is room to wirebond to them later. A fine-tipped soldering iron will probably make your life easier here.⁴ I used to use two interposers, but it's easier to just use one and wirebond directly to the same interposer that you solder to.
3. Glue the interposer to the sample carrier. I would also recommend putting superglue over the solder joints to prevent the wires from disconnecting from the interposer during testing. Again, be sure to not get glue on the rest of the interposer or you won't have room to wirebond.
4. Silver epoxy the MEMS chip to the sample carrier. Use tape to mask off where you want the silver epoxy to be on the sample carrier. Plan to place the MEMS chip as close as possible to the interposer so your wirebonds can be shorter. Place a thin layer of silver epoxy where the chip will go, and make sure it is even/smooth so that it's easier to image under the microscope later. Take care to prevent silver epoxy from getting on the gold-coated interposers; you'll likely short multiple signal paths together if you do. Leave additional silver epoxy on the

³For the interposer, I used the Molex P/N 0150150433 (CABLE FFC 33POS 0.30MM) Gold-coated interposers work the best, otherwise the wirebonder doesn't bond to them.

⁴Metcal soldering irons are fantastic. There's hopefully one floating around your lab somewhere. A good Metcal fine-tip soldering tip to have on-hand is the Thermaltronics M7CH006 Chisel 30deg 0.6mm, Micro Fine.

opposite side of the interposer so you have room to place the substrate grounding wire. Place the substrate grounding wire, and place kapton or another insulating tape on top of it for mechanical stress relief. Place the MEMS chip on the silver epoxy area.

5. Cure the epoxy by placing the entire chip carrier on a hotplate at 150°C for 10 min. Take care not to let the wires touch the hotplate or the insulation will melt.
6. Wirebond the chip. Plan out where your wirebonds will go. Practice wirebonding using a dummy chip first. When wirebonding, take care not to let your large signal wires cause the sample carrier to get knocked off the wirebonder stage. I suggest taping the wires to the side of the chuck to keep them out of the way while wirebonding. Wirebond from the interposer to the chip. Generally speaking, the wirebonds have better adhesion on gold than on silicon, so will tend not to rip out as easily as if you had started the wirebond on the silicon side. Align the sample carrier so that the MEMS chip is directly over top of one of the vacuum holes of the wirebonder chuck. This will make it easier to perform wirebonding.
7. Flipchip bond a coverslip over the actuators and channel (optional but highly recommended). Plan out how large the coverslip should be so that it covers the entire motor and channel and doesn't impede visibility of any important structures. See the [flipchip bonder](#) and [flipchip considerations](#) sections (6 and 6.2.2.4) for further instructions on choosing, generating, and placing the coverslip.
8. Prime a fiber for insertion. See the [next section](#) for more details (3.4.2).

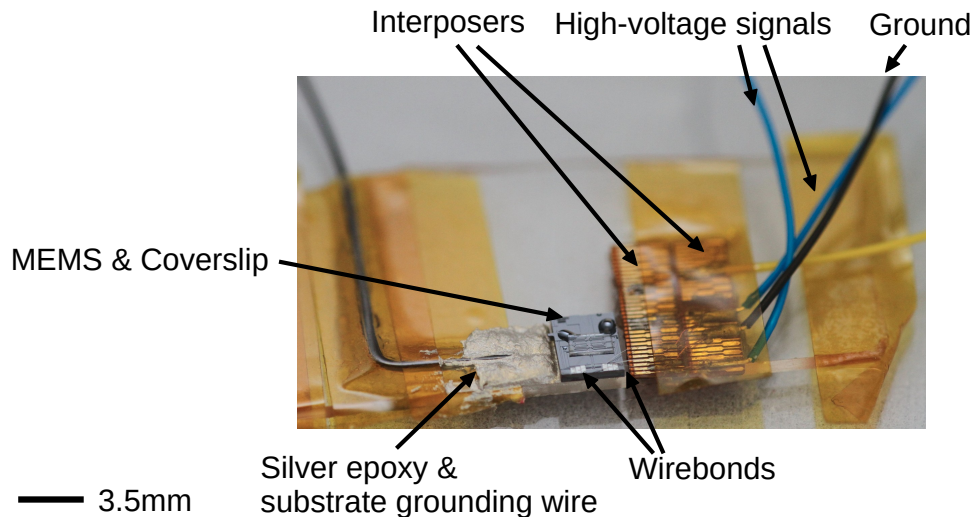


Figure 3.17: Fully assembled MEMS chip with wired components shown. Included are the interposers, high voltage and ground signal wires, wirebonds, and silver epoxy substrate grounding wire.

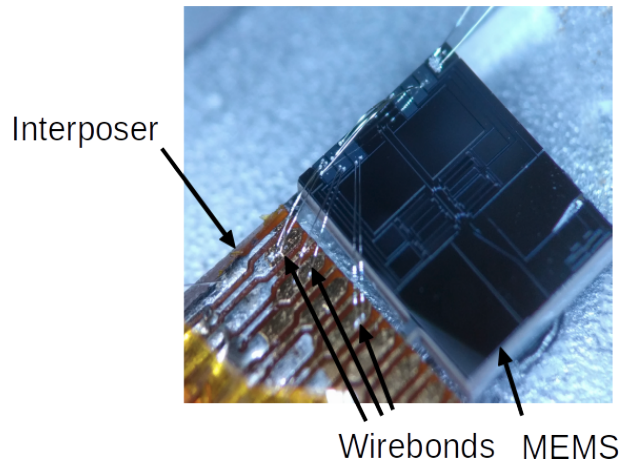


Figure 3.18: Fully assembled MEMS chip with wired components shown. Shown are the interposer, wirebonds, and MEMS chip.

3.4.2.2 Loading a Fiber After fabricating the devices, the carbon fiber is carefully loaded into the channel by hand. First, the entire chip assembly, including glass slide surface, grounding wire, MEMS chip, gold interposers, and wirebonds, is mounted on a vacuum chuck to provide stability during fiber insertion. Using a pair of plastic tweezers so as to prevent electrostatic attraction with the fiber, a single fiber is carefully selected from the larger pile of fibers. The fiber is then aligned to a silicone-coated tungsten micromanipulator probe tip, and temporarily adhered to the side of the probe tip. Note that the silicone-coated probe tip can be constructed by first bending a new probe tip with pliers so that it is parallel to the plane of the MEMS chip (verify by temporarily placing it in the micromanipulator), and then lightly dipping in silicone adhesive and squeegeeing most of the silicone off with your fingers while wearing latex gloves. Leave the wet silicone-coated probetips to dry overnight and they should be ready for use when the silicone has dried completely. See Fig. 3.19 to see an example of a silicone-coated probe tip with fiber attached properly.

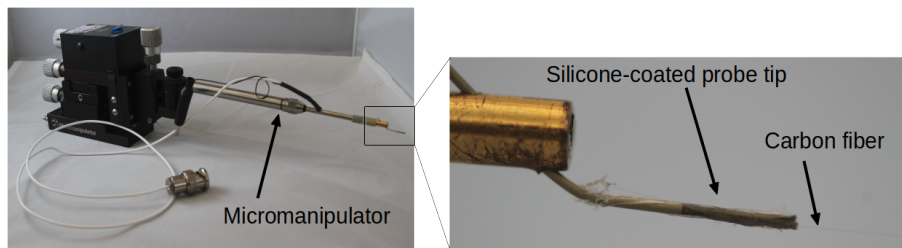


Figure 3.19: Micromanipulator with inset showing bent, silicone-coated probe tip with carbon fiber attached.

I had the best results when only ~8 mm-10 mm of carbon fiber extended beyond the edge of the probe tip, otherwise the carbon fiber was too floppy and became difficult to align due to the slight air currents in the probe station cubby. At this point, the carbon fiber-loaded probe tip assembly can be aligned to the left of the device layer funnel, lowered to the correct z-height above the chip, and inserted into the channel using the x-y manipulators. Refer to Fig. 3.20 for a reference cartoon of the orientation axes. The carbon fiber is in the correct z-plane with the silicon channel if it appears in-focus under the microscope. Make sure to leave enough x-translation on the micromanipulator so that you can advance the carbon fiber forwards a few millimeters within the channel, until it is in

contact with both sets of angled arms. Once the carbon fiber is advanced past both sets of angled arms, you are ready to release the carbon fiber from the probe tip.

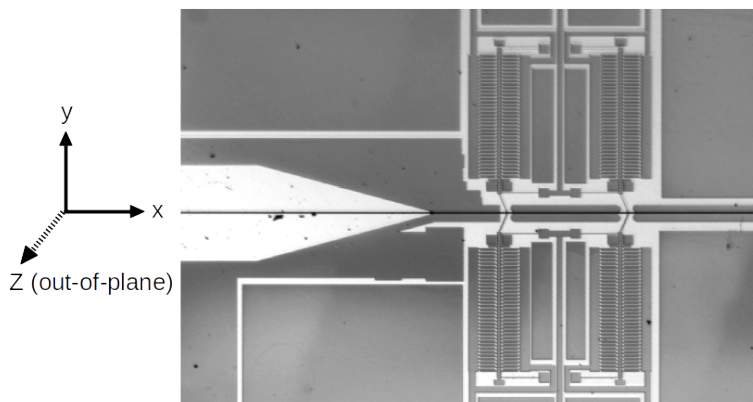


Figure 3.20: Reference x-y-z axes displayed alongside microscope view of a carbon fiber loaded in the chip.

The procedure for this next step depends on whether or not you have placed a coverslip on top of the channel to prevent the fiber from falling out. See the [flipchip bonder](#) section (6) for more details on placing a coverslip on top of the channel.

1. If you do not have a coverslip on top of the channel, expect this step to fail a few times before it is successful. **I cannot recommend using the coverslip enough - it will probably save you hours of hassle!** With no coverslip in place, the carbon fiber is very prone to falling up and out in the z-plane, necessitating you to de-advance the micromanipulator in the x direction and try again. To release the carbon fiber from the probe tip, try bringing the probe tip down in the y-direction. Depending on how you've placed the carbon fiber on the probe tip (on the farther side of the probe tip, along the side as opposed to the top or bottom of the probe tip is probably easier), if you continue to bring the probe tip down in the y-direction, the fiber will eventually catch against the square corner of funnel and begin to detach/ peel away from the probe tip. For this step, make sure to leave enough y-translation in the micromanipulator so you can advance the probe tip downwards all of the way to peel it away from the carbon fiber. If you are lucky, the carbon fiber should now be sticking straight out of the silicon channel with the probe tip far away and detached. Carefully remove the probe tip and micromanipulator from your setup now so that it doesn't accidentally become reattached. See Fig. 3.21 for an example of what the setup should look like after this step.
2. If you *do* have a coverslip in place, this step will be a lot easier. Simply raise the probe tip in the z-direction using the micromanipulator and the carbon fiber should peel away from the probe tip. The final result is the same - the carbon fiber should now be sticking straight out of the silicon channel with the probe tip far away and detached. Carefully remove the micromanipulator / probe tip from your setup now so that it doesn't accidentally become reattached.

See Fig. 3.21 for an example of what the setup should look like after the fiber has successfully been inserted into the channel. A cartoon cross-section of the device with a carbon fiber loaded is shown in Fig. 3.21, middle. For reference, a SEM of a bird's eye view of the device with a carbon fiber loaded is shown in Fig. 3.21, right.

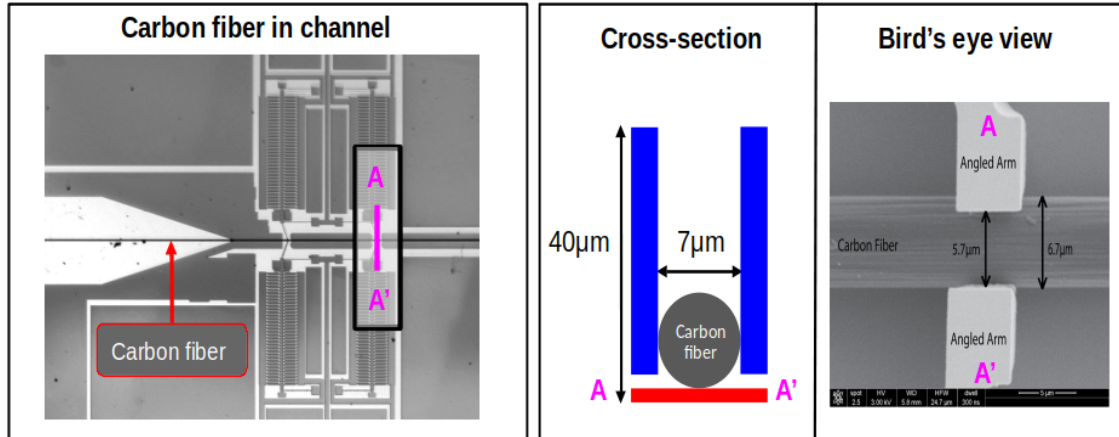


Figure 3.21: Left: Microscope view of a carbon fiber loaded into the channel, with reference cross-section A–A' shown. Middle: Cross-section cartoon of a fiber in the channel. Colors correspond to the SOI fabrication layers as shown in Fig. 3.15. Right: Bird's eye view SEM of carbon fiber loaded in the channel and gripped by two angled arms.

The setup should now be ready for testing.

A few protips regarding the carbon fiber setup:

- The carbon fibers will be much more visible with additional light. Try using a mini spotlight or desk lamp while picking up the carbon fiber with plastic tweezers and adhering it to side of the silicone-coated probe tip.
- It can be difficult to pick up only a single carbon fiber at a time. Try placing a clump of them on a piece of white printer paper placed on or near the probe station, and picking one fiber up from the piece of paper.
- Keep a few silicone-coated probe tips handy. The silicone tends to come off over time and becomes less effective at adhering the carbon fibers in place.

3.4.3 Setup for Penetration into Agar

An agar brain phantom with 0.6% w/w concentration was chosen to mimic mechanical properties of the brain [40], and was used to test the penetration capabilities of carbon fibers driven by the MEMS actuator. As shown in Fig. 3.22, the agar was placed 400 µm from the right edge of the MEMS chip. This separation also helped to minimize possibility of contact between the electrically active wirebond pads and agar subsection.

When testing, the agar was initially too dry, which prevented the fiber from inserting. Since agar is a hydrogel, it can dry out. When it does, a tough skin forms at the surface. By putting a film of DI water over the top surface it should stay soft and fresh. On a similar note, it is a good idea to use only freshly prepared agar, not one that sat in the fridge for day(s).⁵

The fiber was advanced using the minimum voltage V_{actuate} needed to move the fiber (in the range of 20 V–70 V, typically about 55 V). This work did not attempt to prevent discharge or shorting of high-voltage nodes with biological surfaces, but is discussed in the conclusion of this study as future work.

⁵Thank you to **Travis Massey** for being my 2AM inspiration for a solution on this issue!

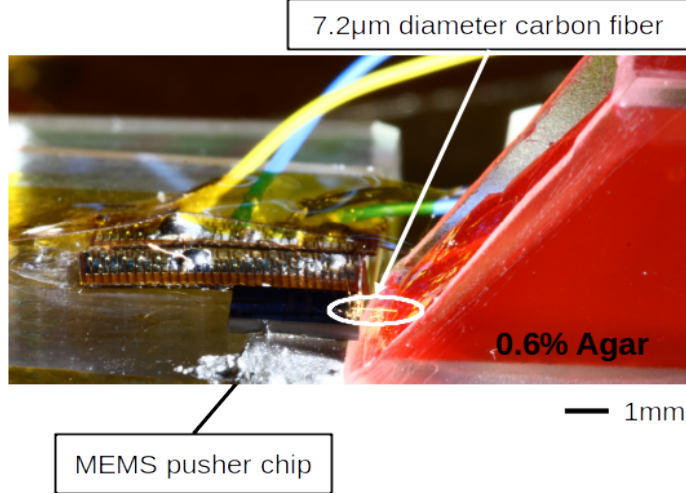


Figure 3.22: The MEMS actuator and a 7.2 μm diameter carbon fiber inserted approximately 400 μm into the agar brain phantom.

3.4.4 Setup for Electrical Impedance Spectroscopy

Electrode impedance measurements were conducted using a Keysight E4980AL precision LCR meter. Measurements were obtained by applying a $1V_{\text{rms}}$ signal of varying frequency between the MEMS signal recording pad and a tungsten electrode placed in 10X PBS. The carbon fiber which extended beyond the MEMS chip edge was also placed in the 10X PBS solution. To ensure proper electrical contact with the fiber, as would be the case during a neural recording, angled arms were kept in contact with the carbon fiber by applying a high voltage to the interdigitated fingers. Frequency was swept over 21 increments from 100Hz to 10KHz, with three measurements taken at each frequency increment and subsequently averaged. Please refer to the [Keysight automation code](#) (section 11.2.1) and [plot generation code](#) (section 11.2.2).

As discussed in the [theory of insertion](#) section (3.3.5), the total path of impedance for this signal, from the tip of the carbon fiber in contact with the electrolyte to the external sensor circuitry wire-bonded to the die, includes: double-layer constant phase element CPE_{dl} at the electrode-electrolyte interface; carbon fiber impedance R_{fiber} ; contact resistance between the carbon fiber and silicon angled arms $R_{\text{contact(fiber-Si)}}$; silicon traces R_{silicon} ; and wire bonds and wire ($R_{\text{wirebond}} + R_{\text{wire}}$). The total impedance can be formulated analytically as in Eq. 3, and is shown pictorially in Fig. 3.23. Two silicon traces and four angled arms form the signal path, helping to reduce the total path impedance.

$$R_{\text{total}} = R_{\text{fiber}} + \frac{\frac{R_{\text{contact(fiber-Si)}}}{2} + R_{\text{silicon}} + R_{\text{wirebond}} + R_{\text{wire}}}{2} \quad (3)$$

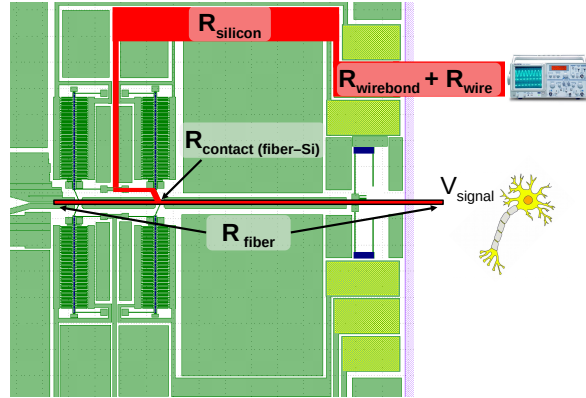


Figure 3.23: Diagram depicting the total path impedance components in red. Note that only one of the silicon traces is highlighted in the diagram while in reality there are two traces that form the signal path. Similarly, only one of the four angled arms is highlighted in the diagram while in reality, four angled arms contact the fiber.

3.4.5 Setup for Recording Dummy Neural Signals

To simulate an *in vivo* recording, a dataset previously recorded from a microwire in an awake/behaving rat motor cortex was played back over a waveform generator (Analog Discovery 2) onto a platinum “neural signal” electrode in 1X PBS.⁶ A silver reference electrode and the tip of a carbon fiber (the “recording electrode”) held by the microelectrode actuator were also placed in the PBS to form a complete circuit. Signals recorded by the microelectrode actuator were amplified using a DAM50 bio-amplifier (World Precision Instruments) and digitized using an Agilent Technologies DSO-X 3034A digital oscilloscope.

3.5 Experimental Results

3.5.1 Penetration into Agar

With $V_{\text{actuate}} = 55 \text{ V}$ applied across the interdigitated fingers at a frequency of 20 Hz, the carbon fiber was successfully able to penetrate 400 μm into an agar brain phantom (Fig. 3.24). A close-up of the carbon fiber inserted into agar is shown in Fig. 3.25. Since the fiber travelled 400 μm from the edge of the chip to the agar, the distance travelled was 400 μm in air and 400 μm in agar, for a total distance travelled of 800 μm . The motor was able to advance the fiber in 1 μm increments. This depth precision is dependent on the angled arm geometry and distance between opposing sets of the capacitive fingers, which in turn are limited by the photolithographic tools.

⁶Thanks to **David Piech** for providing the recording.



Figure 3.24: The MEMS actuator and a $7.2\ \mu\text{m}$ diameter carbon fiber inserted approximately $400\ \mu\text{m}$ into the agar brain phantom.

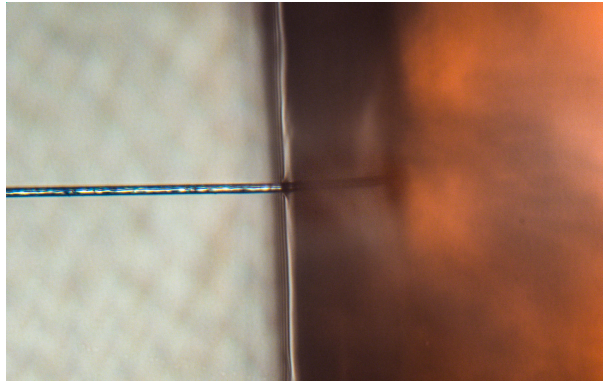


Figure 3.25: Closeup shot of the carbon fiber inserted into agar.

Theoretically, the actuator presented here can output over $1\ \text{mN}$ of force at $85\ \text{V}$, although the experimental force output was not directly measured in this study. A previous iteration of this actuator was capable of advancing a carbon fiber up to $1.8\ \text{mm}$ in air [37], and the current version has been shown to advance a carbon fiber $7\ \text{mm}$ in air (section 4.1). A higher force-output version of the actuator presented here should be able to advance a carbon fiber a similar distance into agar. At this voltage and frequency, the actuator consumes tens of microwatts of power [39].

The carbon fiber is supported on three sides: by the substrate from underneath, and on both sides by the two $40\ \mu\text{m}$ silicon sidewalls which form the fiber channel. Once the fiber advances beyond the edge of the chip and dimples the agar, it can be considered as a fixed-guided beam, as the fiber is no longer free to move laterally at the contact point [14, 18].

Fig. 3.26 shows a carbon fiber inserting into the agar brain phantom. These snapshots of an insertion event suggest that, when operated at $20\ \text{Hz}$, the motor is capable of inserting the electrode at rates up to $10.5\ \mu\text{m}/\text{s}$. This style of electrostatic motor has been shown to operate at speeds of up to $30\ \text{mm}/\text{s}$ in air when operated at $8\ \text{kHz}$ [39], providing an upper bound on the theoretical insertion speed.

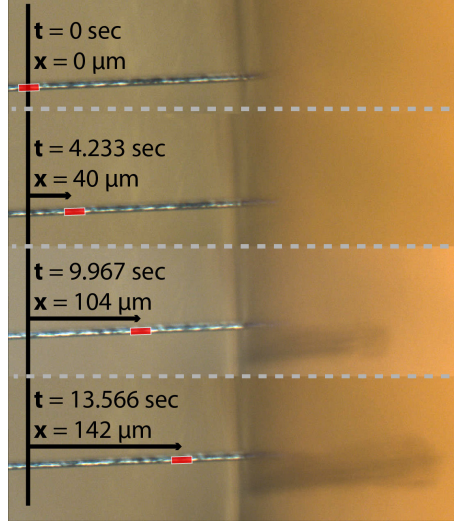


Figure 3.26: Multiple close-up shots showing the insertion of a $7.2\ \mu\text{m}$ diameter carbon fiber into the brain phantom. The red dash indicates the same position on the carbon fiber between frames.

Motor speed exhibits a linear dependence on the operating frequency of the high-voltage waveforms applied to the electrostatic fingers [39]. Slippage was observed at the interface between the carbon fiber and the silicon angled arms, although the degree to which slippage occurred was not quantified. The actuator was not able to push the carbon fiber forwards when actuated at 1 Hz, but was able to push the carbon fiber forwards when actuated at 20 Hz. Slippage can be minimized by increasing the force output of the motors either by changing the motor design or operating the electrostatic fingers at a higher voltage. Additionally, modifying the angled arm contact surface geometry or insulating portions of the fiber to increase static friction with the carbon fiber may aid in decreasing slippage, as discussed in the [angled arm](#) section (4.3).

As a side effect of working in an open, non-cleanroom workspace, small dust particles often became stuck in the channel, necessitating short bursts of repeated voltage ramping to force the fiber past dust particles. From a practical perspective, build-up of dust particles in the channel is the only aspect of this setup which prevents a single actuator from being used to advance longer or multiple electrodes. Coverslips can be used to mitigate this problem, as discussed in the [debris protection](#) section (6.1.2.2).

3.5.2 Electrical Impedance Spectroscopy

Fig. 3.27 shows the impedance spectroscopy for a single carbon fiber electrode held by two angled arms in the actuator fiber channel. Note that the magnitude of the impedance halves when four angled arms are in contact with the fiber, rather than two. The constituent components of this lumped electrode impedance include the double-layer constant phase element CPE_{dl} , impedance of the 10 mm-long carbon fiber R_{fiber} , contact resistance between the carbon fiber and the silicon angled arms, resistance of the silicon traces R_{silicon} , and resistance of the wirebonds and external wires which lead to an off-chip ADC. The resistance of the silicon traces dominated upon measuring each of the constituent impedances in isolation. Future work includes metallizing the silicon traces to reduce sheet resistance from $3250\ \Omega/\square$ with bare silicon traces to approximately $0.3\ \Omega/\square$ for 100 nm aluminum-coated traces, helping to decrease the total silicon trace resistance to approximately 1 k Ω . The total capacitance of C_{fingers} was not directly measured, but is theoretically calculated to be 6.3 pF.

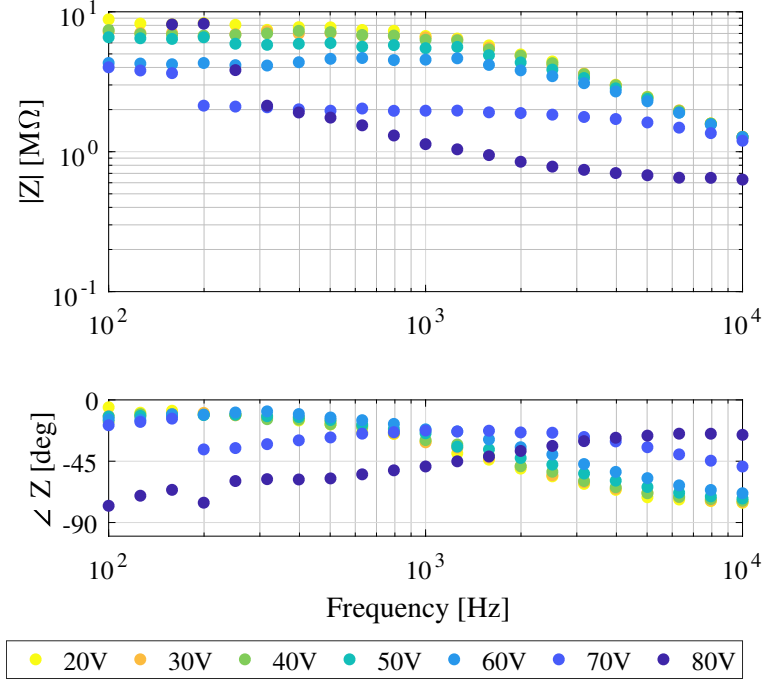


Figure 3.27: Electrical impedance spectroscopy for a single electrode. The microelectrode is held in place by two angled arms. Upper plot shows impedance magnitude; lower plot shows impedance phase. Different colors represent different actuation voltages applied to the electrostatic fingers. Impedance is dominated by the resistance of the silicon traces.

The double layer impedance between 1X PBS and a 5 mm-long, 7.2 μm -diameter fiber was approximately 15 $\text{k}\Omega$, and at low frequencies was mostly resistive in phase. At higher frequencies, the magnitude of impedance dropped to 5 $\text{k}\Omega$, which matches the 1 $\text{k}\Omega/\text{mm}$ -2 $\text{k}\Omega/\text{mm}$ expected impedance of the fiber alone. This result is a function of the electrode area exposed to electrolyte; in this case, 0.11 mm^2 . This is thousands of times larger than in a typical recording scenario in which only the tip of the carbon fiber is exposed to the electrolyte. Additionally, in a typical recording scenario the recording site would be electroplated to decrease its impedance by up to two orders of magnitude [14, 18].

Each of the silicon traces leading from the angled arms to the wirebond pads leading off chip was 10 $\text{M}\Omega$. With all four traces in parallel, the resistance drops to 2.5 $\text{M}\Omega$. The contact resistance between a single silicon pawl and the carbon fiber is on the order of 100 $\text{k}\Omega$; with four angled arms contacting the carbon fiber, the resistance decreases to 25 $\text{k}\Omega$. Overall, the electrode-electrolyte, carbon fiber, and carbon fiber-silicon contact impedances are negligible as compared to that of the silicon traces, but in a scenario in which the traces are metallized and the recording site is small, the electrode-electrolyte impedance should dominate.

Fig. 3.27 also demonstrates significant capacitive crosstalk above 10 kHz . This is likely due to the the silicon trace resistance, which can be decreased by a factor of 10,000 by metallizing the traces, pushing the crosstalk effect out to significantly higher frequencies.

As observed in the magnitude plot of Fig. 3.27, the impedance magnitude decreases as the actuation voltage increases. This is likely because the angled arms grip the fiber with greater force at greater actuation voltages, reducing the contact resistance between the angled arms and carbon fiber electrode. The impedance corresponding to an actuation voltage of 80 V shows a different characteristic profile as compared to that of all the other actuation voltages, potentially due to

nonlinear effects in the motor operation.

3.5.3 Recording of Dummy Neural Signals

To mimic *in vivo* recordings from a mouse, multi-unit activity previously recorded from a microwire in an awake/behaving rat motor cortex was played back and recorded using the microelectrode actuator in “record” mode. As seen in Fig. 3.28, the carbon fiber recording closely resembles that of the signal played back by the waveform generator. The maximum signal amplitude is 70 mV. Although some minor features seen in the waveform generator signal are lost in the carbon fiber recording, major spikes putatively corresponding to firing of the mouse neurons are still clearly visible.

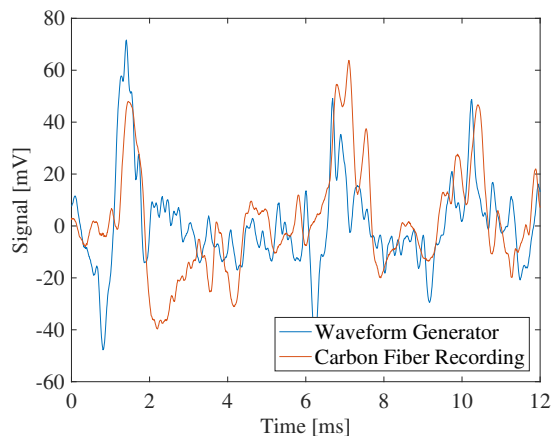


Figure 3.28: Playback of multi-unit activity (blue) is recorded by the carbon fiber microelectrode (red) in 1X PBS. The data was sampled at 125 kHz and a ten sample moving average filter was used to smooth the data.

3.6 Conclusions and Future Work

Electrostatic MEMS microelectrode actuators offer a platform to insert carbon fiber filaments into neural tissue with micron-precision. Based on our measured data, the current actuator is capable of inserting fibers up to 400 μm into an agarose brain phantom at estimated speeds of up to 10.5 $\mu\text{m}/\text{s}$. By taking advantage of previously-designed electrostatic gap closer mechanisms [36, 37, 39], this design could be developed to achieve force outputs necessary to push fibers even greater distances, with greater step precision and greater speed.

The electrical characteristics of the actuator mechanism in the “record” mode are suitable for neural recording applications. Although the current design’s impedance is dominated by the silicon traces for a net impedance of 4 $\text{M}\Omega$ -8 $\text{M}\Omega$, this overall impedance can be decreased by metallizing the silicon traces. While this study used uninsulated carbon fiber filaments, electrodes viable for recording would be insulated in parylene-C near the recording site. Additionally, electroplating poly(3,4-ethylenedioxythiophene) doped with polystyrene sulfonate (PEDOT:PSS) on the recording site would significantly reduce electrode impedance and improve recording characteristics [9, 14].

Layout area could further be minimized to allow minimum-pitch arrays of electrostatic actuator mechanisms to simultaneously position multiple 7.2 μm carbon fibers. Further, creating a bidirectional actuation mechanism would require either duplicating the existing motor or creating a mechanism to reverse the direction of angled arms.

Coating the actuator’s capacitive fingers with a non-conductive material such as alumina would prevent the high-voltage and grounded fingers from accidentally shorting together and discharging through the carbon fiber [4]. Additional packaging is necessary to isolate the electrically active wirebond pads.

This device could also be used as a general platform for flexible electrode insertion. Recently, Luan et al. used a $7\ \mu\text{m}$ carbon fiber to mechanically support $10.5\ \mu\text{m}$ by $1.5\ \mu\text{m}$ flexible recording electrodes during insertion [41]. The actuators presented in this work could be placed on the surface of the brain and used to inject the electrodes developed by Luan et al. [41]. With enlargement of the fiber channel, this device could also be used to deliver optical fibers to precise depths in the brain for optogenetics studies [42].

4 Fiber Pusher Characterization and Improvements

4.1 Farthest Push in Air

In this section we characterize the maximum length of fiber that the fiber pusher can push in air. Although there is no fundamental limit on the maximum length of fiber that can be pushed, in reality factors such as abrasion and friction of dust and loose particles, the uneven carbon fiber surface, and wear of the angled arms prevent the pusher from pushing an infinite length of fiber.

The goal of this test was to see how far the motors could push a fiber with the chip glued down. The sequence of steps to prepare a chip for testing is discussed in the [wiring](#) and [carbon fiber loading](#) sections (3.4.2.1 and 3.4.2.2). The carbon fiber we primed into the channel was 3 cm in length. The motors were operated at $\sim 30\ \text{V}$ and 15 Hz. The fiber quickly went out of the field-of-view of the microscope, so multiple videos were taken to capture the progress of the fiber.

Ultimately, the fiber was able to push 7 mm in air before stopping completely. Multiple attempts were made to “un-stick” the fiber by wiggling it on the left side with a pair of plastic tweezers. Attempts were also made to pull the fiber back out (in the opposite direction of motor actuation), but the motors would get stuck again after pushing the fiber out by 7 mm. Progression shots are shown in Fig. 4.1, and the fully-extended length of 7 mm is shown in Fig. 4.2.

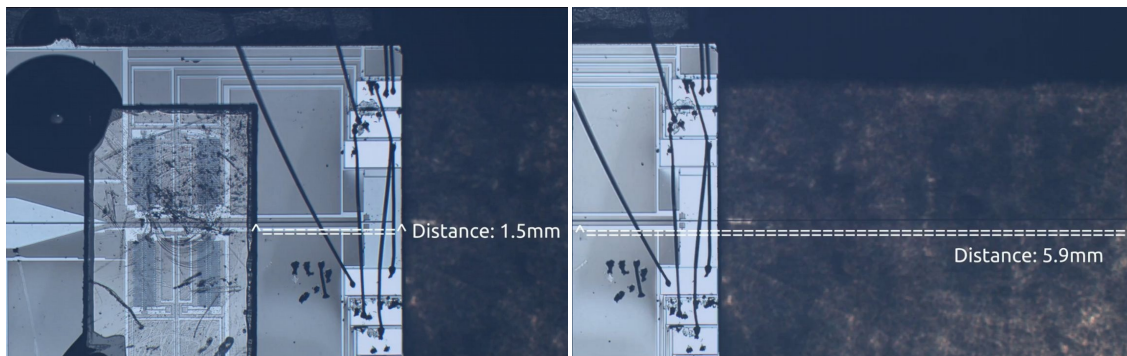


Figure 4.1: Fiber extended 1.5 mm and 5.9 mm, respectively.

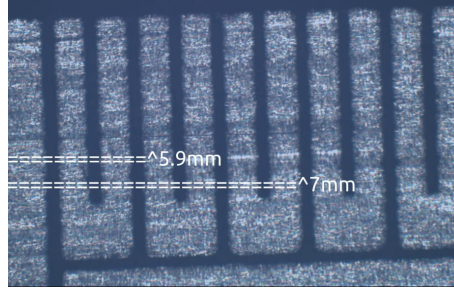


Figure 4.2: Fiber extended 7 mm.

4.2 Motivation for Improvements

This section introduces optimizations of a classical inchworm motor with passive grippers. First, the optimization of parameters of the passive angled arms, including space between gripping arms, angle of the arms, thickness of the arms, and pawl widths is explored. Second, we explore design modifications which allow for insertion and recording from a passivated carbon fiber, necessary to achieve passivation as discussed in the [neural pusher future work](#) section (3.6). While both structures and experimental setups failed for different reasons, there are still useful observations to be gained from this work.

4.3 Angled Arm Optimization ⁷

Oftentimes when advancing a carbon fiber with the MEMS actuator, the silicon angled arms will slip instead of coming into contact and pushing forwards the carbon fiber (discussed further in the [neural pusher agar insertion](#) section, 3.5.1). The amount of slipping has not yet been quantified numerically, so four geometric properties of the passive gripping arms were selected to be optimized and compared in this section: their thickness (“arm thickness”), spacing between the arms (“arm spacing”), angle at which they contact the carbon fiber (“arm angle”), and width of their contacts with the carbon fiber (“pawl width”). To this end, four separate test-related structures were devised in which each of these parameters were tested. A generic diagram of one such test structure is provided in Fig. 4.3.

⁷Thanks to **Aniket Tolpadi** for helping with testing these structures and helping to write this section of the results.

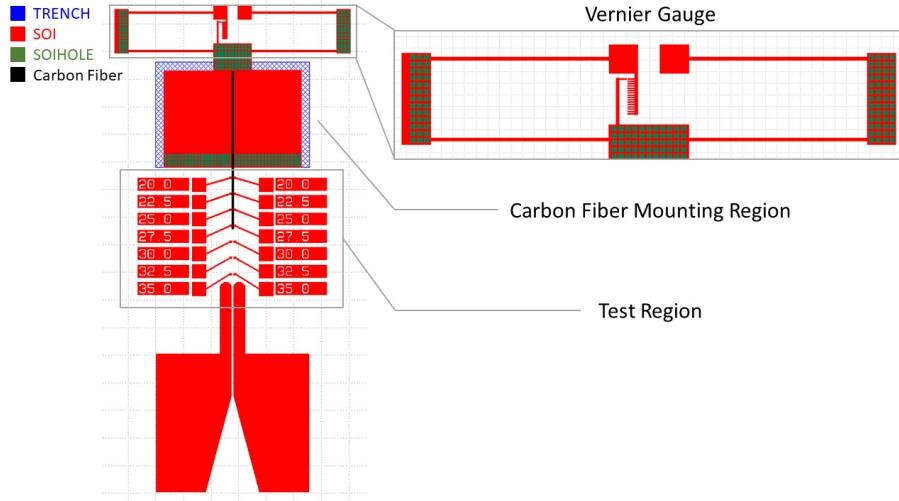


Figure 4.3: Schematic of generic test structure used in optimization of gripper arm geometry. As pictured test structures consist of three primary regions: a Vernier gauge and carbon fiber mounting region, which are identical across all structures, and a test region, which varies based on the property of interest.

As shown, there are three primary regions: the Vernier gauge, the carbon fiber mounting region, and the test region. Across all test structures, the Vernier gauge and carbon fiber mounting region are identical, while the test region is varied to investigate one of the four properties of interest. Within the test region of each test structure, there are seven pairs of gripping arms, and for each pair, the parameter of interest is iterated across a range of interest. For instance, for the arm spacing gripper test structure, the spacing between the arms ranges from $5\ \mu\text{m}$ - $8\ \mu\text{m}$, increasing by $0.5\ \mu\text{m}$ between each pair of adjacent arms. A diagram of the test regions of each of the four test structures is provided in Fig. 4.4.

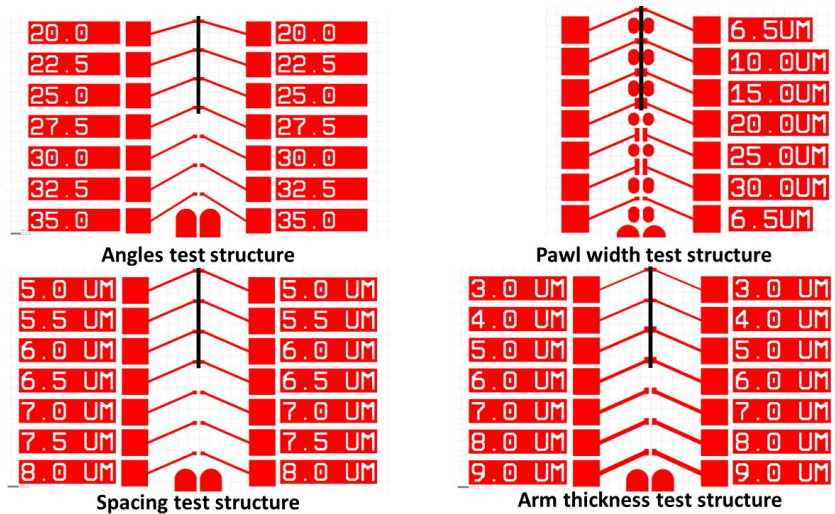


Figure 4.4: Diagram of test regions for each of the four test structures. The spacing between gripping arms, angle at which the arms contact the fiber, thickness of the arms, and pawl widths are tested in separate test structures.

During setup, a carbon fiber is fed through the funnel and test region and into the carbon fiber mounting region, where it is secured using silver epoxy. Once glued, the fiber is anchored to the mounting region, and contacts gripping arms of the test region only by friction; for this reason, its actuation provides insights regarding one of those parameters of interest. During testing, the fiber is pulled out of the test structure (downward, in the orientation of diagram being shown). During this movement, two things are intended to be monitored: the pair of gripper arms that breaks first, and the force recorded from the Vernier gauge when that pair of arms breaks.

Results from testing yielded flaws in the design of test structures that hindered the ability to collect useful data. These flaws primarily fell into the following two categories: weakness of the silicon mounting region, and the lack of a reliable method with which to pull the carbon fiber out of the structure. A secondary flaw which limited data collection was the filling of computer memory during data collection, often in the middle of collection, which caused some videos of testing to be truncated and prevented actual results from being deduced from these experiments.

First off, there were major difficulties when applying silver epoxy to bond the carbon fiber to the carbon fiber mounting region. Two approaches to this were attempted: applying the glue by hand and using a vacuum-secured apparatus to lower a needle coated with silver epoxy into the carbon fiber mounting region. When applying the glue by hand, gluing was successful in one instance, when applying the glue to a pawl width test structure (Fig. 4.5), but in all other cases, the carbon fiber mounting region broke off of the remainder of the device during glue application, preventing any tests from being run.

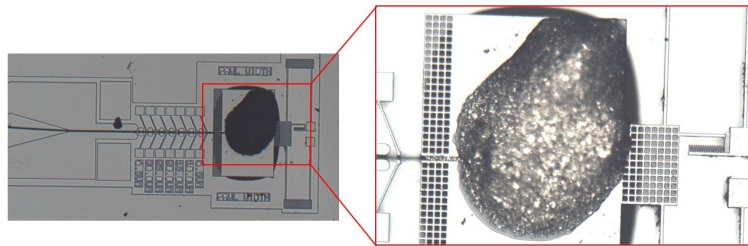


Figure 4.5: Silver epoxy application to pawl width test structure.

Some examples of the mounting region being damaged during manual glue application are shown in Fig. 4.6. Aside from the manual stage, use of the needle to mechanically apply glue to the mounting region saw a different issue arise: with this approach, difficulty was encountered in delivering a sufficient quantity of glue to the carbon fiber-mount intersection. This ultimately caused the carbon fiber to slip out of the mount during testing, even after the epoxy had cured with the application of heat. An image of this unfortunately could not be captured due to lack of disk space on the computer used for image capture. Some of these failures could be attributed to manual errors in assembly, but even so, it does appear that the carbon fiber mount needs to be made sturdier in some manner.

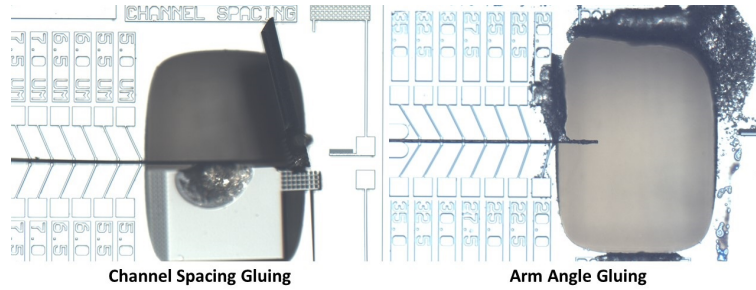


Figure 4.6: Damage sustained in carbon fiber mounting regions upon gluing failures, as demonstrated in channel spacing and arm angle test structures.

Future test structures should employ a separate carbon fiber mounting region and structure for each individual design variable and iteration of each design geometry. Otherwise, it is possible that an uneven distribution of forces during fiber pullout will skew the experimental results and our understanding of the slipping behavior. The test structures may not be as optimal for understanding how the fiber slips as it moves forwards past the arms, as the test structure applies force to the arms as the carbon fiber is moving backwards past them.

4.4 Stationary Gripper Arm

The current design enables for time-interleaved insertion of, and electrical recording from, a non-insulated (non-passivated) carbon fiber electrode. However, to avoid simultaneous recording from multiple neurons in favor of more targeted, single-neuron recording from the tip of the electrode, the length of the electrode should be passivated with material such as Parylene-c (Fig. 4.7).

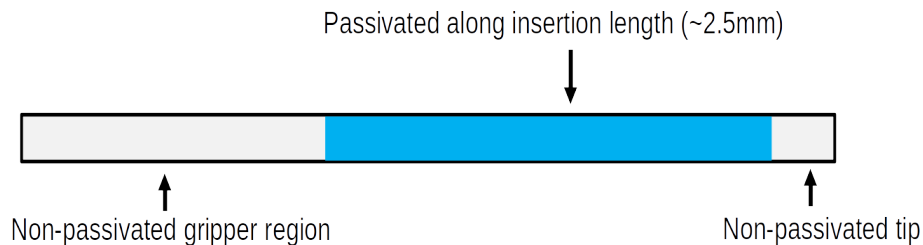


Figure 4.7: Passivated carbon fiber with exposed tip for recording.

To accommodate fibers which are passivated along the inserted length, we propose a mechanism which will be used in combination with a custom-passivated electrode. The custom-passivated electrode will only be passivated along the length of the probe to be inserted. Based on a thorough literature review of existing works which have implanted devices in animal models, ~ 2.5 mm of passivation/insertion length should be sufficient [9, 19, 41, 43–45]. The tip of the electrode will be exposed, as will the remaining length of carbon fiber.

To reflect these changes, the insertion mechanism also needs to be redesigned. We assume the traditional quad set of gap closing actuators (“inchworm motor”) will only come in contact with passivated carbon fiber during the insertion phase into tissue/agar. To record from the non-passivated section of carbon fiber, a separate set of recording arms must be added.

The benefits of the extra set of recording arms are twofold. During priming of carbon fibers into the channel, the arms can grip onto the fiber to prevent it from popping out in the z-plane or otherwise shifting in the x-y directions.

We implemented two designs for the recording arms:

1. A passive structure which nominally grips the non-passivated section of carbon fiber but allows enough slippage for the carbon fiber to move past unhindered. While this setup doesn't require additional signal routing and is thus easier to wirebond, it is probably more prone to mechanical failure due to constant contact with the carbon fiber moving past (Fig. 4.8).

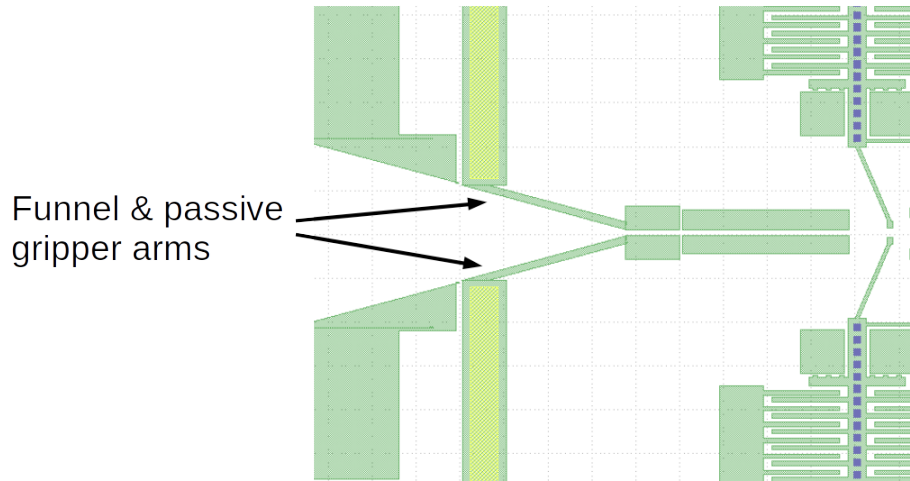


Figure 4.8: Passive gripping structure, with structure indicated by arrows.

2. An active structure which allows the recording arms to be selectively engaged or disengaged. This structure is less prone to mechanical failure as the stationary gripping arms are able to be disengaged completely from the carbon fiber, but require extra signal routing (Fig. 4.9). Note that the spring constant of the stationary gripping arm was not tested experimentally, and was not designed with a particular spring constant in mind, so may be too stiff to function properly as intended.

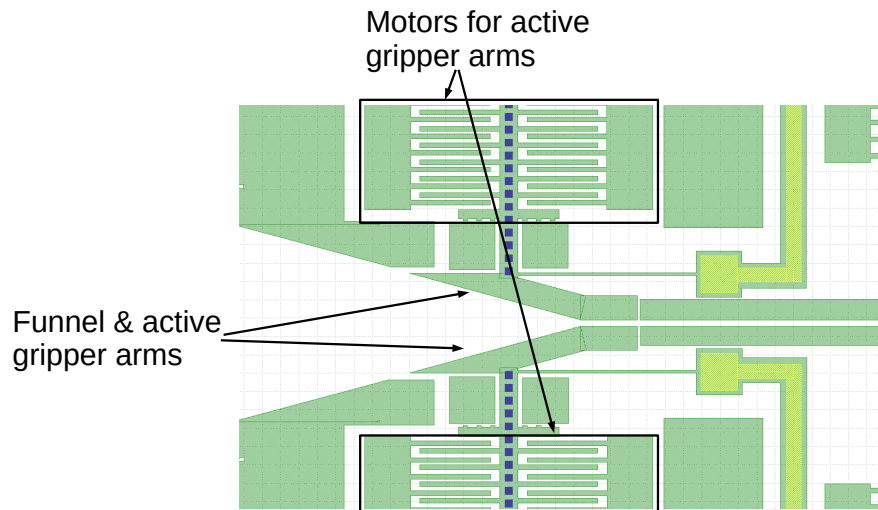


Figure 4.9: Active gripping structure, with arms, funnel, and motors indicated by arrows.

The current design exhibits a silicon “funnel” to help guide fibers towards the channel. These

new recording arms should also have a “funnel” structure to retain this behavior. As a side-effect of priming the carbon fiber, large lateral forces will be applied to the silicon recording arms. To prevent them from fracturing, they will need to be designed with spring constant and the applied force due to the carbon fiber in mind.

4.5 Wirebond Placement

Finally, wirebond pads were moved from the far right edge of the chip to the center of the chip to prevent shorting to biological materials. This optimization may be less ideal for stackups where the wirebonds would ideally be closer to the edge of the chip. Refer to the [integration suggestions](#) section for more details on integration (5.3).

5 Inchworm Robot

5.1 Electrostatic ‘Inchworm’ Inchworm

While previous work focused on jumping [4], flying [5], and walking microrobots [2], an interesting class of microrobots that hasn’t been as actively explored are microrobots that create the surface on which they move. Microrobots could build useful structures in which they later move around, much like a spider [6]. Similar to how spiders produce different types of silk depending on the application, a microrobot could build arbitrary structures out of different materials that are sticky, dry, hydrophobic/philic, elastic, etc. The microrobot could first deploy a structural support, followed by additional structures with different material properties.

In this section, we present a few ideas for the development of a complete silicon spider which can extrude a strut and then climb along it. This structure would be akin to that of a tightrope walker, with the 7 μm -diameter carbon fiber serving as the tightrope. For example, the Japanese company HiBot built a mesoscale version of a tightrope walker to inspect high-voltage power lines [46]. A concept diagram for our micro-scale robot is shown in Fig. 5.1. The tightrope could also be oriented vertically, so that the robot is climbing and descending (vertical) as opposed to moving laterally (horizontal).

The same actuator we have been discussing in previous sections could be used in a different way. By fastening down the carbon fiber, we can use the same motion that was previously used to push the fiber to allow the chip climb along it.

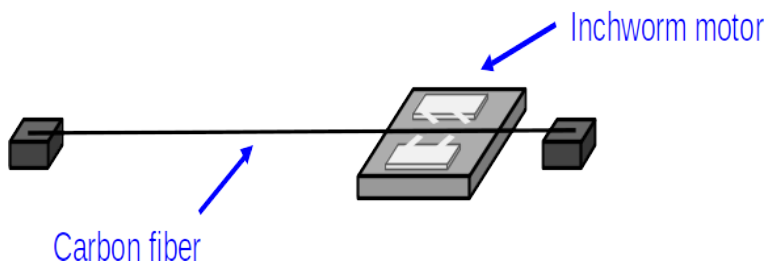


Figure 5.1: Cartoon diagram of the carbon fiber inchworm robot.

The voltage control signals produce the exact same movements that were discussed in the [neural pusher theory](#) section (3.3.5). Over time, the robot will push/pull itself along the carbon fiber, as shown in Fig. 5.2.

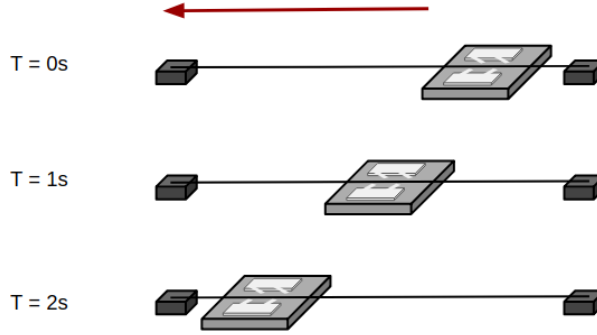


Figure 5.2: Cartoon diagram of the carbon fiber inchworm robot inching forwards (or backwards, depending on how you look at it). The external HV signals and control module are not depicted in this diagram.

A few key metrics for these robots are the length of structural support the robot can carry (which would depend on the method used to coil the structural support onto the microrobot), the distance the robot can travel autonomously (with onboard power and control), and the maximum weight the robot can travel with. Microrobots become truly useful and deployable only when they are untethered, hence the push towards developing truly autonomous microrobots.

5.2 Mass and Power Budget

We will now explore the physical constraints of the combined fiber pusher/crawler microrobot, including on-board power and control circuitry. This section attempts to answer high-level questions relating to the force output of these actuators, the total mass it could carry, and the amount of on-board power supplied by a solar cell. Using first-principles equations and experimental data recorded from microrobot-sized solar cells, we will analytically identify the ideal current, frequency, and voltage operating points for the actuators. In the [gca force output](#) subsection (5.2.1), we will discuss the force output of the gap closing actuators as it relates to different design parameters. In the [solar cell](#) subsection (5.2.2), we will discuss the I-V characteristics of the solar panel and constraints on possible operating regimes.

5.2.1 Gap Closing Actuator Force Output

The analysis below is generic to any gap closing actuator. In a few places, we list dimensions and force outputs that are specific to this design and application.

For a more thorough analysis of the components of these equations, please refer to Chapter 3 (Electrostatic Inchworm Actuators) of [2]. [36] is the original work and provides a more detailed analysis of the mechanisms. This section provides only a very high-level analysis for the purpose of mass-power budget calculations specific to this design, whereas [2] discusses each of the components of the analytical expression in much greater detail. The force provided by the motors depends on the geometry of the gap closing actuator (GCA) array: the total number of fingers in the two arrays that actuate at a given time N , overlap length of the fingers L_{ol} , silicon thickness T , initial front-gap distance when open x_0 , initial back-gap distance when open x_b , displacement of the fingers in the y-direction during actuation Y_I , and spring constant of the actuator return springs k . The force also depends on the actuation voltage V , which can be changed during experiments. The resulting equation for the force produced by the electrostatic motors in the y-direction is shown in Eq. 4.

$$F_y = \frac{1}{2} \epsilon_0 V^2 N L_{ol} T \left(\frac{1}{(x_0 - Y_I)^2} - \frac{1}{(x_b + Y_I)^2} \right) - k Y_I \quad (4)$$

k is calculated by treating the beams as a set of two fixed-guided beams in parallel, as shown in Eq. 5. E is the modulus of elasticity of silicon, and w_{spr} and L_{spr} are the width and length of the silicon springs, respectively.

$$k = \frac{2ETw_{spr}^3}{L_{spr}^3} \quad (5)$$

We then equate F_y to F_x , the force provided to the fiber in the horizontal, x-direction, using Eq. 6. α refers to the angle of the angled arms (see [2, 36] for more details).

$$F_x = \frac{F_y}{\tan \alpha} \quad (6)$$

For our design, values for the geometry of the gap closing actuator array are shown in Table 4. The computed F_y and F_x values are shown in Table 5. Note that the distance between the pawls is $10 \mu\text{m}$ and the fiber is $7 \mu\text{m}$ in diameter, so the angled arms pull in by $Y_I = (\frac{10 \mu\text{m} - 7 \mu\text{m}}{2}) = 1.5 \mu\text{m}$. The gapstop has $2 \mu\text{m}$ of total travel, so with $Y_I = 1.5 \mu\text{m}$ of travel already used from the angled arms pulling in to touch the carbon fiber, the remaining $0.5 \mu\text{m}$ of travel is used to push the carbon fiber forwards [36]. For the purposes of this calculation, F_x and F_y are evaluated at 55 V to be consistent with that used in experiments, but in reality the actuator can be operated at any voltage within the range $0 \text{ V} - 110 \text{ V}$.

Table 4: Geometry of the gap closing actuator array

Geometry	Value
ϵ_0	$8.85 \times 10^{-12} \text{ F/m}$
N	$70 \frac{\text{fingers}}{\text{half}} * 2 \text{ halves} = 140 \text{ fingers}$
L_{ol}	$77 \mu\text{m}$
T	$40 \mu\text{m}$
x_0	$3 \mu\text{m}$ (ignoring undercut)
x_b	$5 \mu\text{m}$ (ignoring undercut)
Y_I	$1.5 \mu\text{m}$
α	67°
E	169 GPa
w_{spr}	$3 \mu\text{m}$
L_{spr}	$194 \mu\text{m}$
k (Eq. 5)	50 N/m

Table 5: Nominal gap closing actuator operating forces at 55 V

Force	Value
$F_y _{55 \text{ V}}$	2.4 mN
$F_x _{55 \text{ V}}$	1.0 mN

By sweeping the voltage, the force output F_x in the direction of the fiber movement increases quadratically (see Fig. 5.3).

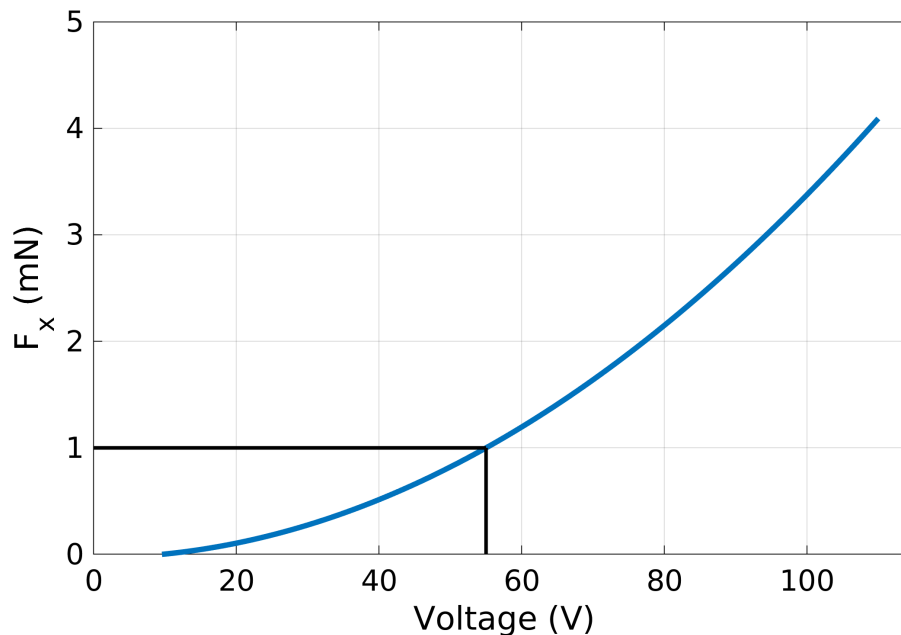


Figure 5.3: Theoretical force vs voltage curve for a gap closing actuator with dimensions as listed in Table 4. The operating point at 55 V and 1 mN is annotated by the black lines.

5.2.2 Solar Cell Operating Points

A complete system necessitates having a power source that enables the microrobot to be autonomous - the most obvious being a miniature, microrobot-sized solar panel which we refer to as ‘Zappy2’.⁸ We will now analyze how much power the current iteration of this panel can provide to the robot. The equations and constraints on the operating regimes of the solar panel and actuators are as follows, and are discussed in further detail below. Note that these equations describe the ‘average’ system dynamics as opposed to the instantaneous mechanical and electrical dynamics.

- Equation 1: IV curve of the solar panel. The operating I and V of the actuator must lie on the solar panel IV curve.
- Equation 2: $I = CVf$. The operating frequency of the actuators is f .
- Constraint 1: $V > V_{pi}$ to turn the motors on.
- Constraint 2: $f > f_{operate}$ otherwise the actuator will not push the fiber forwards (at an appreciable speed).

5.2.2.1 Equation 1: IV curve of the solar panel The I-V curve and corresponding power curves are shown in Fig. 5.4. The maximum power of 323 μ W is delivered from the solar panel to the actuator at 104 V.

⁸The solar cell and high-voltage buffers were designed by our collaborators, led by **Jason Stauth** at Dartmouth.

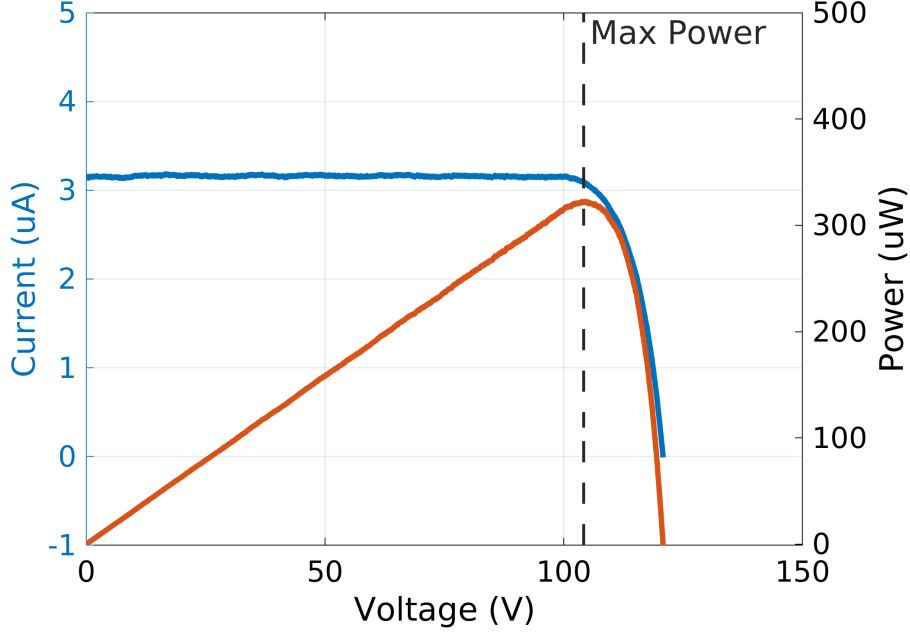


Figure 5.4: Zappy2 solar cell I-V curve and power curve. The maximum powerpoint of $323 \mu\text{W}$ at 104 V is indicated by the vertical line.

5.2.2.2 Equation 2: $I = CVf$ This equation specifies the relationship between the gap closing actuator's operating current, voltage, and frequency to the capacitance of the fingers when they are pulled in. It can be derived by dividing $Q = C_{gca,closed}V$ on both sides by t (Eq. 7 and Eq. 8). The total capacitance of the gap closing actuators when they are closed is calculated as in Eq. 9. Note that for this analysis, the total number of fingers, N , includes all four of the GCA arrays, as opposed to just the two arrays we used in the force analysis.

$$Q = C_{gca,closed}V \quad (7)$$

$$I = C_{gca,closed}Vf \quad (8)$$

$$C_{gca,closed} = \epsilon_0 N L_{ol} T \left(\frac{1}{(x_0 - Y_I)} + \frac{1}{(x_b + Y_I)} \right) = 6.3 \text{ pF} \quad (9)$$

The possible operating frequencies are calculated by taking each of the solar cell's (V, I) pairs and solving for f . The formula is shown in Eq. 10 and the resulting graph of points is shown in Fig. 5.5. The operating frequency corresponding to the maximum powerpoint at $323 \mu\text{W}$ is 4.7 kHz .

$$f = \frac{I}{CV} \quad (10)$$

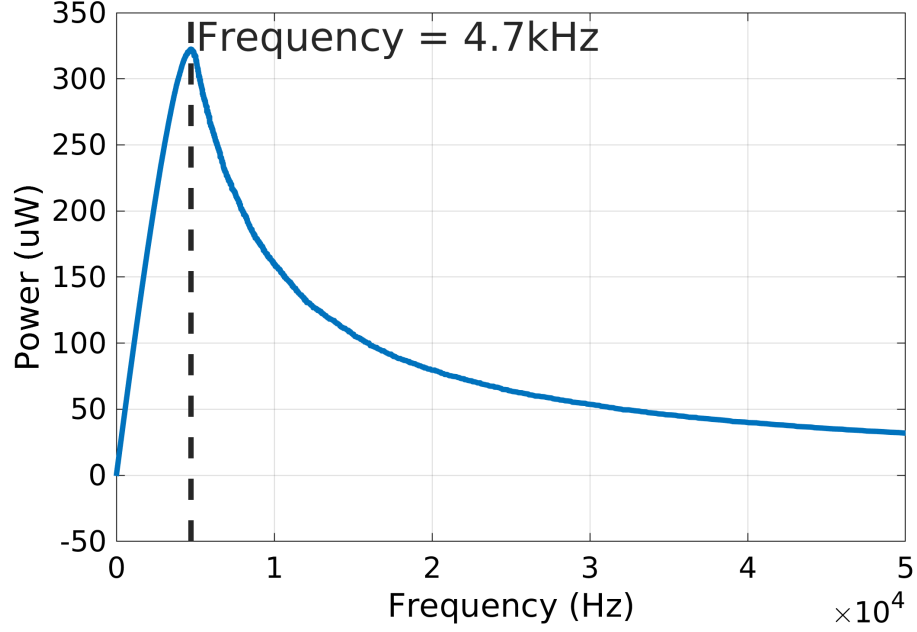


Figure 5.5: Frequency operating points which correspond to valid points on the solar cell IV curve.

5.2.2.3 Constraint 1: $V > V_{pi}$ The voltage operating point must be larger than the pull-in voltage of the actuator. The equation for the pull-in voltage is shown in Eq. 11. For this system, $x_{pi} = \frac{1}{3}x_0 = \frac{1}{3}(3 \mu\text{m}) = 1 \mu\text{m}$. Similarly, V_{pi} for this system is 15 V.

$$V_{pi} = \sqrt{\frac{2kx_{pi}}{\epsilon_0 N L_{ol} T} \left(\frac{1}{(x_0 - x_{pi})^2} - \frac{1}{(x_b + x_{pi})^2} \right)^{-1}} = 15 \text{ V} \quad (11)$$

$$x_{pi} = \frac{1}{3}x_0 = 1 \mu\text{m} \quad (12)$$

The GCAs often get stuck in a shut position at operating voltages greater than around 70 V, placing an upper bound on the operating voltage. Future work would investigate why the GCAs get stuck shut at larger operating voltages. This problem limits the total force output of the motors.

5.2.2.4 Constraint 2: $f > f_{operate}$ Experimentally, the fiber-pusher motors do not seem to push the fiber forwards if the frequency is too low. The lower operating limit on frequency has not yet been established quantitatively and is a good candidate for future work. The speed of a silicon shuttle vs frequency is shown in Fig. 5.6.

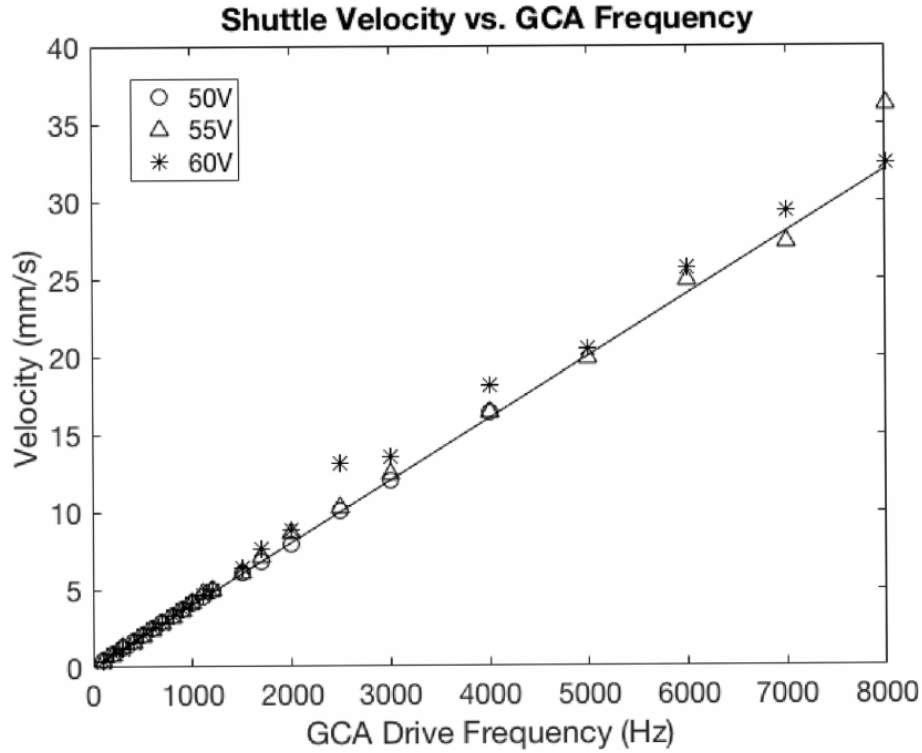


Figure 5.6: Frequency operating points which correspond to valid points on the solar cell IV curve.

5.2.3 Inchworm Motor Integration Operating Points

From a physics standpoint, the motors must be strong enough to overcome the static friction between the MEMS chip and the substrate, in this case a glass slide ($\mu_{s, \text{MEMS-glass}}$). The original MEMS chip weighs 22 mg and the redesigned MEMS chip (with less dummy fill) weighs 8 mg, while the coefficient of static friction was experimentally found to be $\mu_{s, \text{MEMS-glass}} = 0.7$.⁹

Drawing a free body diagram of the setup (Fig. 5.7) and equating the forces as in Eq. 13, the motors must be able to provide at least $\mu_{s, \text{MEMS-glass}} mg$ newtons of force.

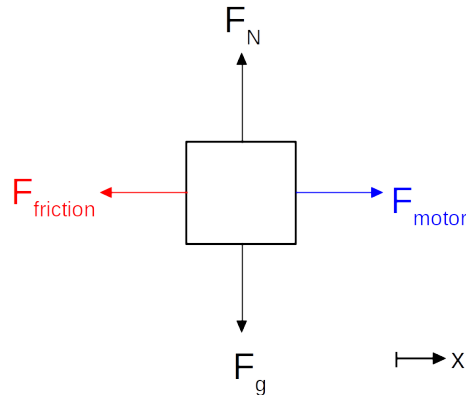


Figure 5.7: Free body diagram of the setup.

⁹Determine the coefficient of static friction by measuring the angle at which a piece of silicon begins to slide on a piece of glass. $\mu_{s, \text{MEMS-glass}}$ is then calculated as the tangent of that angle ($\mu_{s, \text{MEMS-glass}} = \tan(\theta_{\text{slip}})$).

$$\begin{aligned}
\sum F_x &= 0 & (13) \\
F_{\text{motor}} - F_{\text{friction}} &= 0 \\
F_{\text{motor}} &= F_{\text{friction}} \\
F_{\text{motor}} &= \mu_{\text{s, MEMS-glass}} mg
\end{aligned}$$

This means that the motors must be able to provide 144 μN of force for the 22 mg chip, and 66 μN of force for the 8 mg chip. The motors must eventually be strong enough to compensate for the additional weight of the coverslip, and eventually the solar panel, signal control IC, and supply capacitors. To be able to pull the weight of a fiber pusher with dummy fill, a SCUM, a Zappy2, a coverslip, an 0402 supply capacitor, and an 0603 supply capacitor, the fiber pusher must be able to pull 37.2 mg of weight, equating to 250 μN of force. Table 6 shows the constituent masses and corresponding motor force required to carry each element, assuming silicon is the material in contact with a glass surface. Please refer to the [appendix \(11.3\)](#) for the MATLAB code used to produce these estimates.

Table 6: Mass and force requirements for autonomous microrobot

Component	Dimensions (mm x mm)	Thickness (mm)	Weight (mg)	Additional F_{motor} required (μN)
Fiber Pusher (dummy fill)	4.5 x 3.5	0.590	21.6	144
Fiber Pusher (no dummy)	3 x 2.4	0.590	9.9	66
SCUM (signal control IC)	3 x 2.5	0.300	5.2	35
Zappy2 (solar cell & HV buffer)	3.5 x 3	0.300	7.3	49
Coverslip (mylar)	1 x 2	0.127	0.4	2
0402 supply capacitor	1 x 0.5	0.6	0.65 ¹⁰	4
0603 supply capacitor	1.6 x 0.8	0.9	2.0	4

5.3 Suggestions for Integration

There are two high-level steps needed to integrate the fiber crawler (MEMS) with the power and control circuitry.

The first demonstration would be of a fiber crawler that crawls along a pre-deployed fiber, with the aid of external power and control circuitry. The fiber crawler actuators should be able to provide enough force so that the crawler can pull its own weight along the fiber. See the [externally-powered crawling](#) section (5.3.1) for more details.

The next demonstration would be of a fiber crawler that crawls along a pre-deployed fiber, with on-board power and control circuitry. See the [on-board power and control](#) section (5.3.2) for more details.

At the end of this section, we also discuss a few high-level concept ideas that would enable the fiber crawler to ascend or descend a fiber that it deploys (as opposed to a pre-deployed fiber).

¹⁰Weight estimates from Mouser 0402 and 0603 MLCC capacitor.

5.3.1 Crawling with External Power and Control

Although I did not quite get the fiber crawler to crawl along the carbon fiber, I came up with a process for most of the setup:

1. Test motors.
2. Bond clear coverslip to chip.
3. Prepare interposers; glue down to glass slide.
4. Wirebond between interposers + taped-down chip (note: tape should be applied to the sides of the chip as opposed to the bottom, otherwise all of the wirebonds and fiber will rip off). The wirebonds will be multiple centimeters long; mine were ~ 2 cm.
5. Load carbon fiber.
6. Glue down silicon platform near end of carbon fiber; glue one end of carbon fiber to it (see Fig. 5.8 and Fig. 5.9).

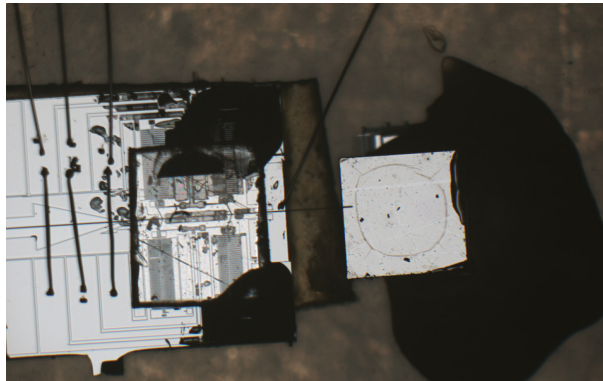


Figure 5.8: Carbon fiber suspended from chip, with silicon platform at right.

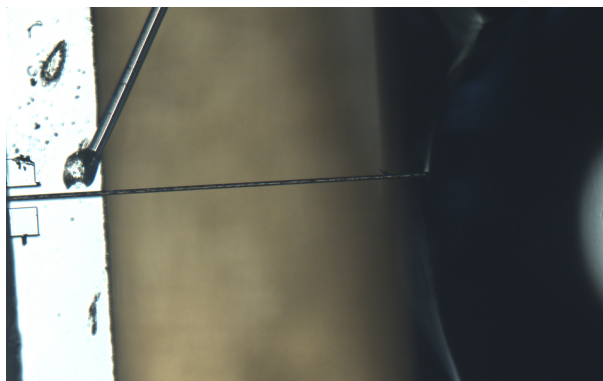


Figure 5.9: Carbon fiber glued to silicon platform.

7. Glue other end of fiber (optional for now; not clear whether this is necessary).

5.3.2 Crawling with On-board Power and Control

After getting the inchworm motor to crawl along a fiber with power and controls provided via wirebonds, the next steps would be to integrate a power source for the actuator's high voltage signals, and a control module to generate the anti-phase clocking scheme to run the inchworm motors. Other members of our group have designed a crystal-free ASIC that has both onboard transceivers and digital logic [47]. In addition, our collaborators have developed a high-voltage chip with onboard integrated solar panels. By combining all three chips, we could develop an autonomous inchworm robot.

The block diagram showing connections between the three chips is as shown in Fig. 5.10. Zappy2, the solar cell chip, provides power to the microprocessor. In exchange, the microprocessor provides clocking I/O to the solar cell's high-voltage buffers. Finally, the clocked high-voltage buffers provide power and ground signals to run the MEMS actuators. Two supply capacitors help to keep the voltage supply levels constant. For the microprocessor, the capacitor should store enough charge to prevent supply droop for the amount of time and charge it takes to send a single packet. For the MEMS, the capacitor should prevent significant supply ripple that would hinder electrostatic pull-in at the operating frequency.

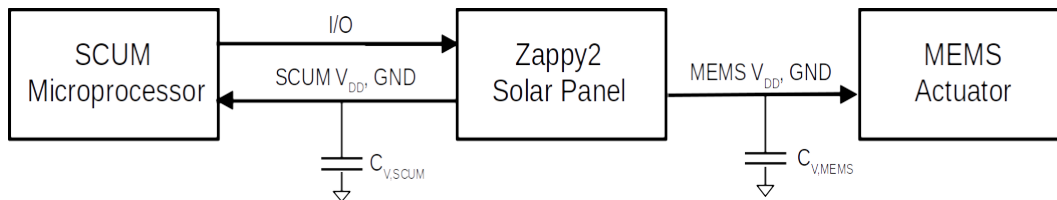


Figure 5.10: Block diagram showing the electrical connections between the three chips needed to make an autonomous microrobot.

Note that a coverslip is necessary to prevent the fiber from falling out of the channel. With the cover in place, the inchworm robot remains in contact with the carbon fiber and is able to continue inching forwards (see Fig. 5.11). Placement of this cover is discussed in greater detail in the next section (6).

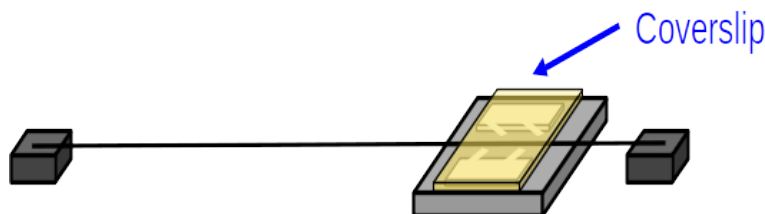


Figure 5.11: Cartoon diagram of the carbon fiber inchworm robot.

To make the integrated microrobot dream a reality, many steps are needed.¹¹ From an integration standpoint, it is easier to lay the three chips flat next to each other than to stack them one on top of the other. A concept diagram is shown in Fig. 5.12. Each of the three chips is epoxied and wirebonded to a flexboard.¹² The flexboard provides a durable platform for signal routing.

¹¹Thanks to **Alex Moreno** and **Craig Schindler** for their thoughts on this.

¹²Consider using Gold Phoenix for a low price-point flexboard manufacturer.

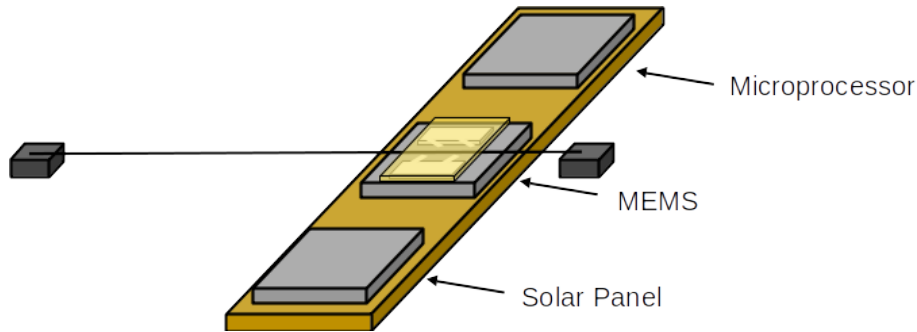


Figure 5.12: Block diagram showing the electrical connections between the three chips needed to make an autonomous microrobot.

In reality this diagram is not quite complete, as it does not include the supply capacitors, substrate connection pads, or wirebonds. Fig. 5.13 shows the additional connections. The wirebonds depict the setup at a high level and do not show the exact placement of the wirebond pads on each of the three chips.

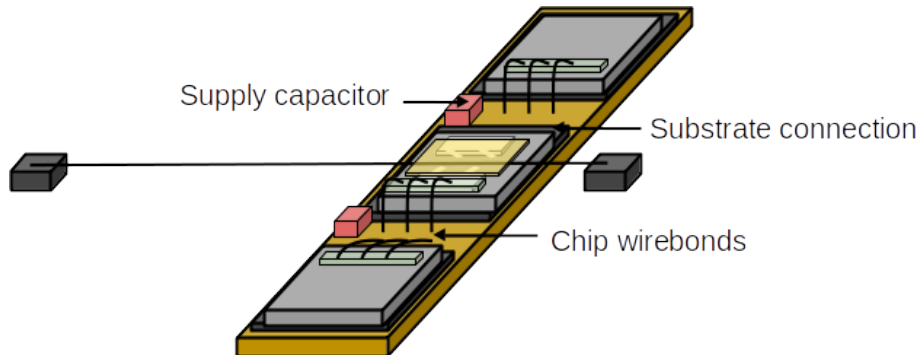


Figure 5.13: Block diagram showing details of all connections between the three chips.

The substrate connection pads and wirebond pads should be fairly large, so that the chips can be easily manually placed and wirebonded. It would probably be better to place the two supply capacitors $C_{V,SCUM}$ and $C_{V,MEMS}$ first, prior to epoxying the three chips down. Consider leaving wirebond pads available on the flex board for SCUM and Zappy2 debugging.

The entire assembly process might look like:

1. Glue down supply capacitors.
2. Test MEMS actuators.
3. Bond clear coverslip to MEMS chip.
4. Silver epoxy the MEMS chip to the flexboard. Note that the MEMS substrate needs to be grounded otherwise the electrostatic actuators will not actuate properly.
5. Load a carbon fiber.
6. Glue down silicon platform near end of carbon fiber; glue one end of carbon fiber to it (shown as dark grey cube at left and right edges of carbon fiber, in diagrams).

7. Test SCUM and Zappy2 to ensure functionality.
8. Prepare SCUM microprocessor and Zappy2 solar panel chips by epoxying and wirebonding them to the flexboard.
9. Glue down other end of carbon fiber onto silicon platform after preparing the other two chips.

The last two steps in this sequence are probably interchangeable, although since SCUM and Zappy2 chips have a longer lead time for manufacturing and would thus be more frustrating to accidentally break, it's probably better to load the carbon fiber while they are not present, to avoid breaking them.

Here are a few rules of thumb when coming up with new assembly processes. You should also refer to the [assembly process \(3.4.2.1\)](#) for the neural pusher testing, as there are a few more integration and assembly steps there that might be helpful.

- If possible, wirebonding should be the very last step (or one of the very last steps), as the wirebonds are quite fragile.
- You are probably already aware that gluing is generally non-reversible. This includes super glue and silver epoxy. Tapes are more friendly, and there are many types! Single-sided, double-sided, various widths of Kapton, paper tape, masking tape, packing tape ... the list goes on. Think about how these might come to your advantage, depending on what you're trying to accomplish.
- Solder joints are more durable than wirebond joints, so should be completed first if possible.
- In order to wirebond, the sample needs to be held fairly firmly by the vacuum. I have found that it is easier to glue the chip down, or tape it using doublesided tape, and then place the chip directly over top of one of the vacuum holes of the wirebonder chuck.
- The wirebonder has very good positioning capabilities. If there are very small pieces of silicon scrap that are in the way on your chip, you may be able to remove them electrostatically by placing the wirebonder wedge close by. I suggest turning the wirebonder off when you try this, but keep the light on.
- When designing your MEMS, make sure to leave enough space between wirebond pads so excess wirebond tails don't end up in the channel between adjacent wirebond pads and cause them to short.
- I like to use the following Westbond wirebonder settings: ¹³ Power:380 or 400; Time:40ms.
- Micro scalpels are surprisingly useful for cutting tiny things in a pinch, and are probably good to keep on-hand. ¹⁴

5.3.3 Ascending and Descending

After the basic fiber crawler works horizontally (or maybe crawling up an incline) and with integrated power and control, the next thing to do is add functionality! This requires redesign of the core MEMS structure. Similar to how a spider weaves a web, the crawler should be able to tack one

¹³Cory 490E Westbond machine: buffer 10 or 11, as of the time of this writing, but check that the presets haven't been changed.

¹⁴I like the GF Health 2979#15 Sterile Micro Scalpel, 15°Angle.

end of its fiber “web” and then descend. It would ideally be able to ascend after descending, and optionally re-coil the fiber for reuse.

The tack could consist of a sticky pad which is pre-loaded and stuck onto the end of a long carbon fiber. The user could stick the sticky pad onto a ceiling or other surface, or the microrobot could provide enough horizontal or vertical force to place the tack. Then, the robot would descend in a controlled fashion letting go of the fiber completely and then re-grabbing the fiber after a prescribed amount of fall time. It could also descend more slowly and precisely by using the actuators to crawl down the fiber. A concept diagram for this mechanism is shown in Fig. 5.14. A possible concept diagram of sticking and descending is shown in Fig. 5.15.

To ascend without re-furling the fiber (assuming one end of the carbon fiber is now completely free and hanging below the fiber crawler), the actuators can pull the crawler up the fiber. To ascend and refurl the fiber, additional mechanisms are needed to furl the fiber back into its silicon compartment. The compartment could possibly be designed in such a way that the fiber would furl by itself, without needing additional motorized components to push it properly into place in the compartment.

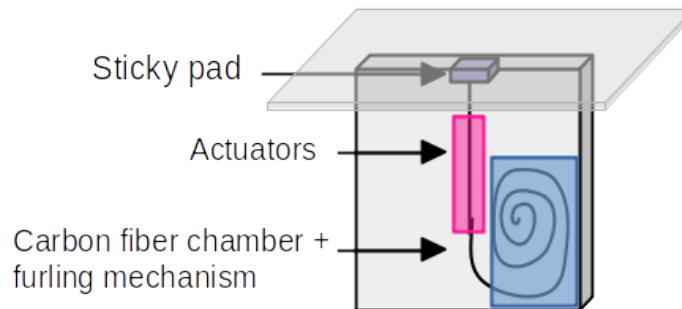


Figure 5.14: Concept diagram of mechanisms used for descending. Note the purple sticky pad, gray surface at top, pink area highlighting the actuators, and blue area highlighting the fiber chamber and area for fiber un/furling mechanisms.

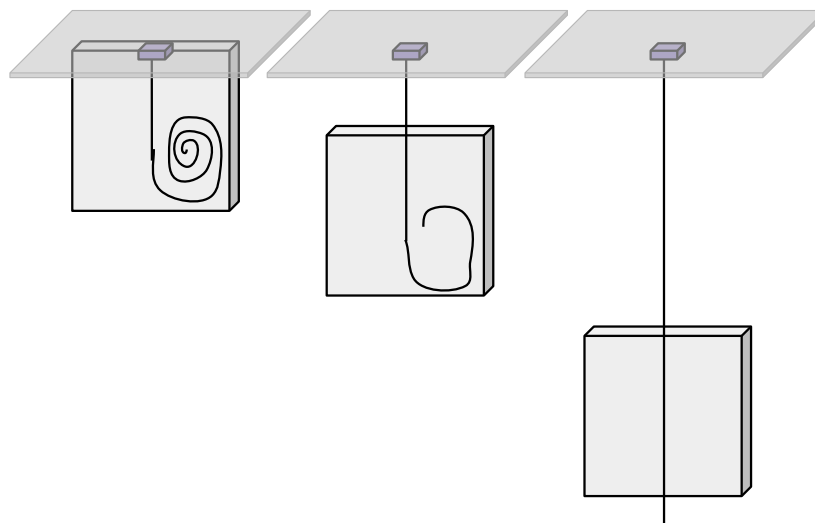


Figure 5.15: Concept diagram of descending.

If crawling horizontally, the fiber crawler might potentially be able to operate by grabbing the fiber with all four angled arms at once, and then letting go with all four angled arms, as opposed to actuating with anti-phase signals. The motors would be 2x smaller in this case, as the force during each “crawl” sequence would be twice as large as before.

When ascending vertically, the anti-phase signals are necessary to prevent the crawler from accidentally descending when the angled arms release.

6 Flipchip Bonder

6.1 Use Cases

Flipchip bonding is a technique commonly used in the integrated circuit (IC) industry to interconnect ICs and external circuitry. The IC with bumps (e.g. balls of metallized copper) on the top of the chip is flipped upside down and aligned directly on top of the metal pads of the external circuitry. The entire stack is subsequently heated to reflow the components together. Another method, wirebonding, connects ICs placed alongside external circuitry via thin wires.

The flipchip bonding technique is particularly useful in aligning and placing materials onto SOI MEMS structures. For instance, protective cover pieces can enhance MEMS functionality by maintaining 2D in-plane motion of silicon joints [2, 48], preventing unwanted contact between foreign materials (dust, loose material fragments) and native silicon elements, or providing containment of non-silicon design elements such as non-conductive solids or liquids (hydrogel was used in [3]; carbon fiber threads were used in [37] and [49]).

The bonding setup ¹⁵ consists of a vacuum-suction pickup arm, vacuum base plate, camera, beamsplitter to capture images of both the top and bottom substrate, and monitor to display an overlay image of the two substrates. Refer to Fig. 6.1 for a more detailed cartoon diagram of the components, and more detailed picture diagram of the setup.

¹⁵The flipchip bonder used for this work was a Finetech FINEPLACER 96 Lambda, located on the first floor of Cory Hall.

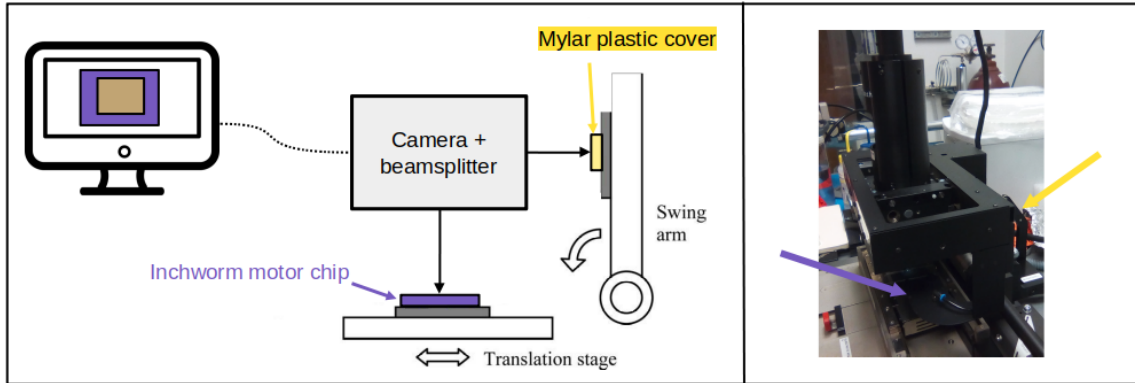


Figure 6.1: Left: Cartoon diagram indicating the components and placement of experimental samples in the flipchip bonder. Note the computer monitor displays an overlay of the mylar plastic cover (top substrate) and inchworm motor chip (bottom substrate). Right: Picture diagram indicating the components and placement of experimental samples in the flipchip bonder. The yellow arrow at the right indicates the vacuum-suction pickup arm which will pick up the top substrate. The purple arrow at the left indicates the vacuum base plate where the bottom substrate is positioned.

The bonding process consists of two stages. First, the top substrate is aligned and picked up using the vacuum-suction pickup arm. Next, the bottom substrate is aligned to the image of the top substrate with the aid of the camera, beamsplitter, and real-time overlay image of both substrates. The top substrate is brought down into contact with the aligned bottom substrate, and subsequently attached in place via a variety of methods (heat, epoxy, etc).¹⁶ Methods for generating cover materials and attaching them to a substrate are discussed in the [flipchip considerations](#) section (6.2.2.4).

6.1.1 Comparison to Wafer Bonding

Why not use wafer bonding instead of flipchip bonding? The wafer bonding process bonds one whole wafer to another whole wafer, and may be more suitable for some applications:

- Potentially more cost and time-effective than flipchip bonding, since each alignment and bonding procedure results in a whole wafers' worth of chiplets being bonded.
- Alignment accuracy of $1\ \mu\text{m}$ with sufficient user proficiency [50].
- More options for bonding types: including anodic bonding, radical assisted bonding, direct bonding, thermocompression bonding.
- Both wafers must be either visual or IR light transparent. Silicon and quartz wafers meet these criteria; other materials might not.

Meanwhile, the flipchip bonder may be more suitable for other applications:

- In addition to adhesion via heat and/or pressure, items can be adhered using photopolymers such as UV cure epoxy.

¹⁶The bottom substrate is now 'undercover'.

- Easier to iterate on placement with individual chips. Don't need to process two entire wafers (bottom wafer, top wafer) before performing bonding. For more information on parallel preparation of two separate wafers for wafer bonding, see Contreras' "Robot Process Description" on page 108 of [2].
- Easier to iterate on cover material types, cover material thickness.
- Samples can be in various state of prep; solder, tape, etc.

6.1.2 Specific Design Examples

Next, we will explore specific use cases where coverslips attached using the flipchip bonding process could be used to protect silicon joints, prevent contamination of moving elements, or contain non-silicon elements.

6.1.2.1 Prevention of Silicon Out-of-Plane Buckling Coverslips could be strategically placed so as to eliminate out-of-plane buckling of silicon pin-joints or other similarly at-risk structures while not interfering with the movement of other structures.

The silicon pin joints described in [51] are fabricated in a single layer of silicon and do not have capping structures to hold the rotating elements in plane. These structures are sensitive to out-of-plane forces above 100 μN , and higher forces are enough to pop the pin-joints out of plane, disassembling them [2].

Fig. 6.2 shows a silicon MEMS aerodynamic control surface for use in millimeter-scale rockets and other miniature aerial vehicles [48]. The out-of-plane silicon fin is inserted into an SOI rotary slot mechanism, which pivots about a central pin joint and is controlled via two opposing electrostatic actuators. The pin joint holding the thin silicon fin in place is susceptible to out-of-plane buckling, rendering the fin unusable. Fig. 6.2, right, depicts possible placement of a coverslip to prevent out-of-plane motion. Note that the proposed coverslip placement would not interfere with the out-of-plane fin's rotational movements.

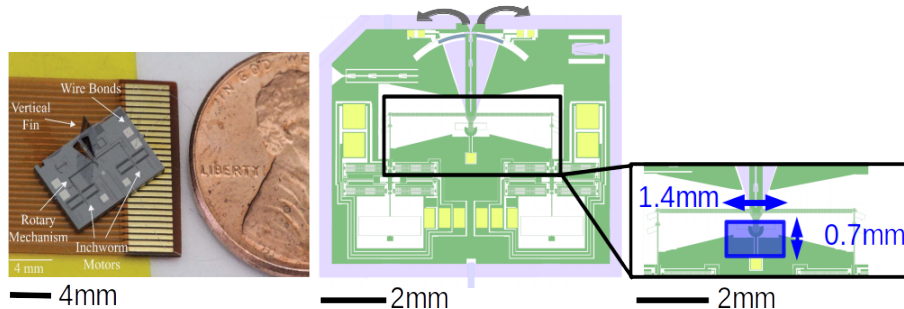


Figure 6.2: Left: Picture of vertical fin assembled into rotary slot mechanism. Middle: Layout diagram; gray arrows indicate direction of motion of rotary slot mechanism. Right: An inset of the middle image, with possible coverslip placement over the central pin joint indicated by the blue rectangle.

Fig. 6.3 shows a single-legged silicon walking robot and silicon walking hexapod which consists of three pairs of two-degree-of-freedom legs. Each silicon leg has a number of pin joints which are susceptible to out-of-plane motion. In previous work, silicon screens and linkages were used to prevent out-of-plane motion [2]. One advantage of these screens as compared to a fully-enclosing coverslip

is that the joints are still accessible with a probe tip for debugging purposes. A fully-enclosing coverslip, envisioned in blue in Fig. 6.3, might still be useful for the purpose of both preventing out-of-plane silicon motion and protecting the electrostatic motors from debris.

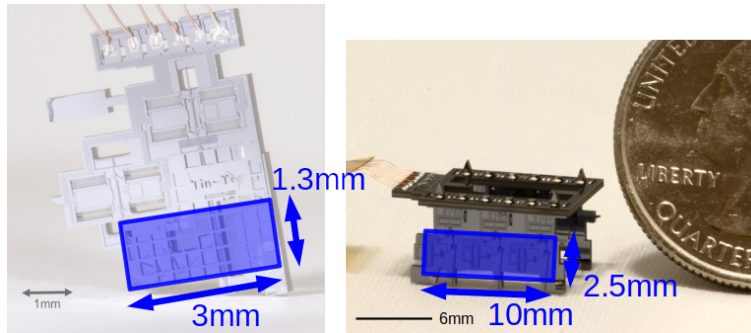


Figure 6.3: Left: Single-legged silicon walking robot [2] and silicon screens and linkages used to prevent out-of-plane motion, with possible coverslip placement shown in blue. Right: Silicon walking hexapod [2], with possible coverslip placement shown in blue.

6.1.2.2 Protection from Debris Fig. 6.4 shows a silicon jumper which consists of a large silicon spring and motor actuation stages [52]. These structures are not as susceptible to out-of-plane silicon motion. However, dust and other airborne contaminants could impede the movement of any number of silicon structures. A coverslip, if placed over the entirety of the movable silicon motors, could help to increase the lifespan of these structures by preventing damage to moving components (see Fig. 6.4).

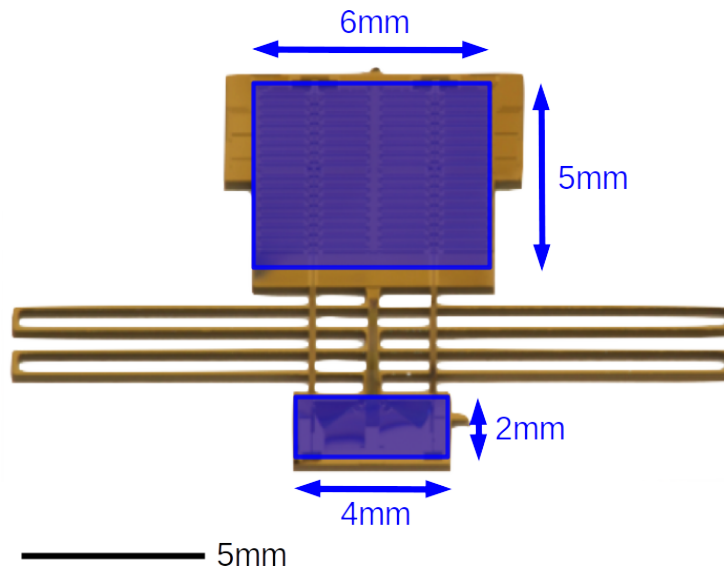


Figure 6.4: Left: The silicon jumper with possible coverslip placement shown in blue.

6.1.2.3 Enclosure for Untethered Silicon Structures¹⁷ Silicon etchholes are commonly used in SOI processes to release silicon structures so that they are free to move. Normally, released

¹⁷Thanks to **Ryan Shih** for providing inspiration for this example case, via testing of his circular motor.

silicon structures are tethered to a non-released section of silicon. However, some structures might be fully released during operation by design (i.e. no tethers). For these structures, a coverslip is essential to prevent untethered structures from floating away during operation. A mock-up design is shown in Fig. 6.5. A square of fully-released silicon, shown in center, is gripped by two gear-tooth structures which are released but tethered by springs, shown at left and right. The square is designed to be capable of moving completely independently of the substrate, but will float up and out of plane if not for a coverslip preventing this direction of movement. During fabrication, the square of silicon should be temporarily tethered to prevent the silicon square from floating away during processing. During testing, the temporary tether can be broken, and a coverslip attached. Care should be taken to prevent glue from getting in the etch holes and preventing movement of released structures.

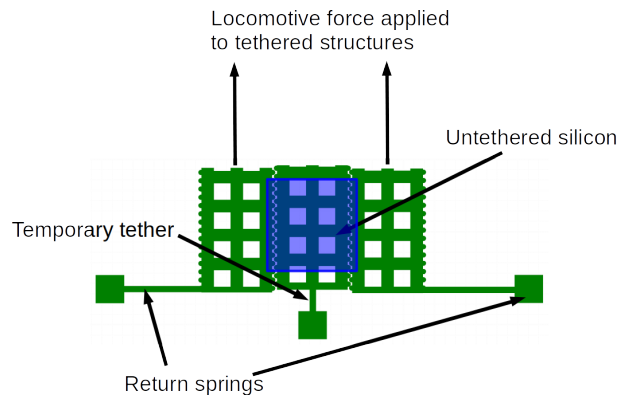


Figure 6.5: Example of an untethered structure and possible coverslip placement (shown in blue) to prevent untethered structure from floating away.

6.1.2.4 Containment of Non-Silicon Design Elements Other designs employ non-silicon components which interact directly with silicon components. Depending on the component material, these components can be contained with non-silicon covers which are attached as part of a post-processing step.

In the case of [3], dried polyacrylamide was hydrated inside a silicon channel and used to drive forwards a carbon fiber. To contain the hydrated polyacrylamide hydrogel, microfabricated silica covers were attached to the silicon substrates. This setup is shown in Fig. 6.6.

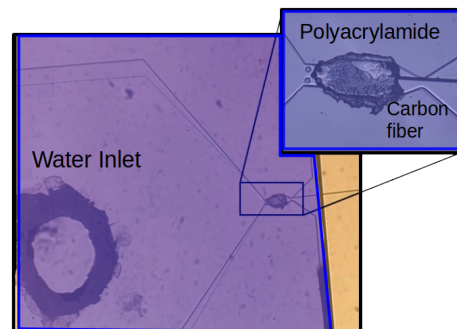


Figure 6.6: Dried polyacrylamide is hydrated inside a silicon channel. The silica cover, highlighted in blue, contains the liquid hydrogel inside the silicon channel. Reproduced and modified with permission from [3].

Similarly, [49] uses mylar covers to contain and prevent carbon fibers from moving out of plane within a microfabricated silicon channel. This setup is shown in Fig. 6.7.

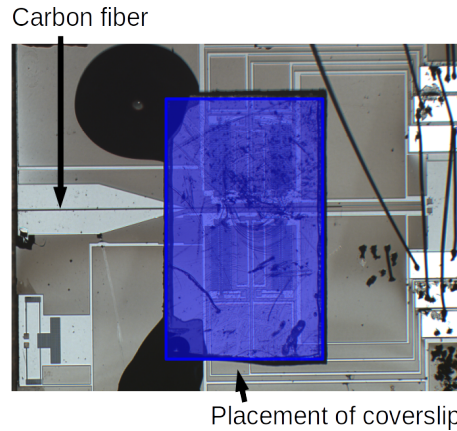


Figure 6.7: A carbon fiber travels within the silicon channel. The mylar cover, shown in blue, prevents the carbon fiber from falling out of plane and exiting the channel.

6.2 Design Considerations

6.2.1 Flipchip Bonder Design Considerations

There are many design considerations to keep in mind in order to achieve a successful bond. Depending on your design, there are different cover materials, methods of preparing these covers to the desired dimension and shape, and methods of attaching the coverslip using the flipchip bonder. Also think about how the geometry of your SOI GDS affects coverslip placement. This is by no means an all-inclusive list of everything you *must* do, just a few suggestions that might make your initial design easier.

- When bonding, the material with the larger footprint would ideally be on the bottom, while the material with the smaller footprint would ideally be on top. This is not absolutely necessary - gluing will be easier if the top material is smaller than the bottom material, but other bonding techniques might not have this requirement. This should become more apparent once you try gluing two dummy pieces together using the flipchip bonder.
- If needed for electrical or mechanical testing/assembly, avoid covering those portions of silicon with a coverslip. This may include but is not limited to wirebond pads, mechanical assembly slots, large springs, etc.
- Consider the order of your other post-processing steps. Will you need to manually glue, solderpaste, wirebond, apply adhesive, etc after flipchip bonding? If so, consider how much space you will need on your chip needed to manually complete these steps. Will the coverslip be in the way or be an impediment in any way to other processing steps? How can you reduce this effect?
 - The wirebond wedge will need silicon access within at least $\pm 50 \mu\text{m}$ of the wirebond area, perhaps more.
- Consider how you will be able to see particular features during the assembly. Will you need to use a 45 degree mirror?

- If you plan to attach the coverslip to the SOI design with UV cureable epoxy or another form of glue, consider:
 - The overall size of the glue dabs can be highly variable, since they are manually placed. Make sure to leave enough dummy silicon to safely land glue dabs. The smallest glue dabs I've had success in placing are $\sim 750\ \mu\text{m}$ in diameter (see Fig. 6.8).

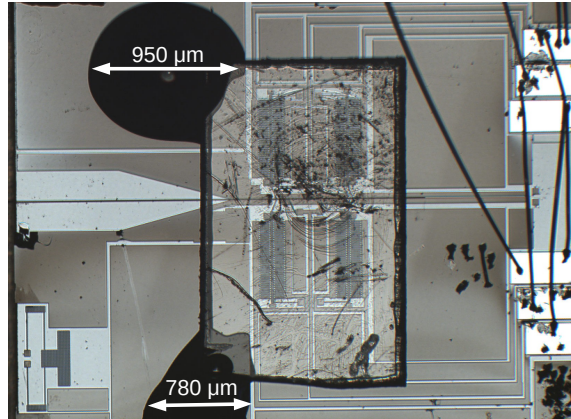


Figure 6.8: Representative image of a coverslip placed and attached to a silicon die with UV cureable epoxy. Relative size of the glue dabs is indicated by the white arrows.

- On a related note, it is easier to place glue dabs along the edge of a chip as opposed to in the middle of a chip.
- The glue tends to wick in between silicon traces (see Fig. 6.9). Make sure there are no active devices in this area which will be rendered unusable if they are covered in glue. The epoxy is relatively insulating, so if there is glue in between silicon traces, they will not short. In Fig. 6.9, although the glue has wicked onto the top of the fingers, it has not wicked in between the fingers, so the motors still work.

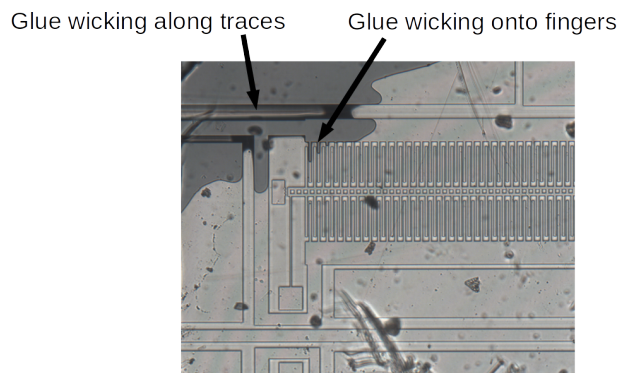


Figure 6.9: Zoom-in shot of a coverslip placed and attached to a silicon die with UV cureable epoxy. Note the glue wicking into nearby silicon traces and electrostatic actuator fingers.

- Depending on your use case, glue dabs do not always need to be placed on all of the corners of the cover. Two corners may be sufficient.

- Square or rectangular-shaped cover pieces are generally easier to work with than more abstractly-shaped pieces. This is true for both [generating](#) the cover as well as [placing and attaching](#) the cover (sections 6.2.2.2 and 6.2.2.3).

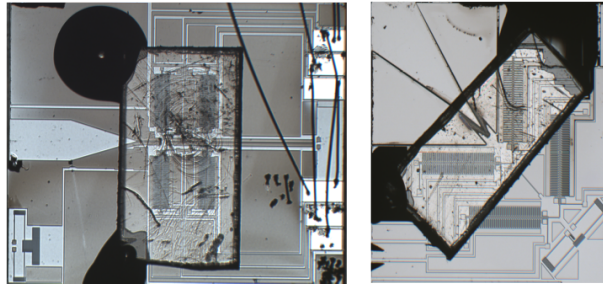


Figure 6.10: Left: A cover is placed at a 0° orientation. Right: A cover is placed at a 45° rotation to cover the entirety of the motors. Note that a trapezoidal-shaped coverslip may have been more ideal in this case, as it is difficult to place the rectangular-shaped coverslip without covering the wirebond pads.

- The silicon area underneath the cover will still be visible through a microscope, albeit with an overlay of a few scratches in some places, if the cover has micro-scratches. The silicon area underneath the edge of the cover will *not* be visible, however. If there are critical structures which you need to be able to image for an experiment, it would be safer to enlarge the cover so that it covers all structures entirely, leaving mostly only dummy silicon directly underneath the edge of the cover. Fig. 6.11 provides examples of different placements of a coverslip.

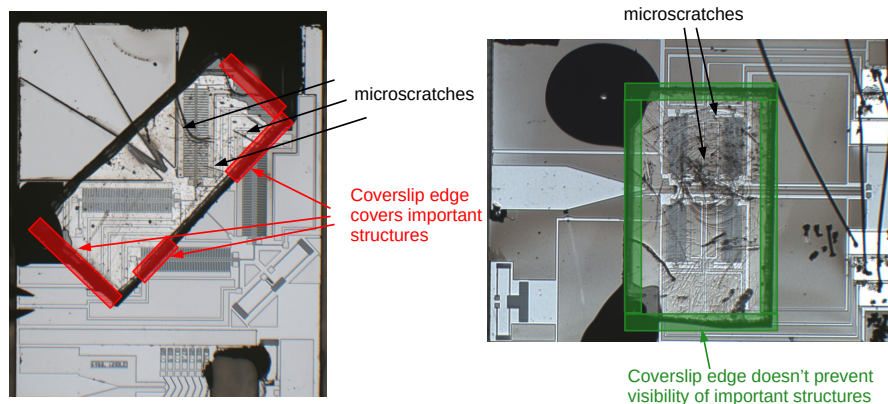


Figure 6.11: Left: The smaller coverslip ruins visibility of devices which are directly under the edge of the coverslip, highlighted in red. Right: The larger coverslip is placed such that its edge, highlighted in green, only impedes visibility of dummy silicon area. Note the microscratches on the cover surfaces in both images.

- It will be very difficult to remove the cover after it has been placed. This may be an issue if your devices get stuck often and need to be manually released with a probe tip. It would also be difficult to image failed devices after-the-fact (e.g. with SEM), if a cover is in place.

6.2.2 Flipchip Bonder Design Options

6.2.2.1 Cover Material The ideal cover would be as thin as possible to minimize weight, flat so as to not destroy delicate structures, optically transparent to enable imaging of structures beneath the cover, and able to be safely cut or trimmed using one of the techniques presented below (section 6.2.2.2). Note that the final SOI device thickness for my devices is on the order of $550\ \mu\text{m}$. Many materials come in form factors that meet these requirements:

- **Mylar**, a polyethylene terephthalate (PET) film, is transparent clear. I experimented with 5mil films ($127\ \mu\text{m}$), but thinner films are available online. See Fig. 6.12 (left) for an example of what the kapton looks like when bonded to silicon.
- **Kapton**, a polyimide film, is amber/bronze in color yet still transparent. It is commonly used as an insulating tape for electronics components, but also comes in a non-adhesive format. As of the time of this writing, films as thin as 0.5mil ($12.7\ \mu\text{m}$) are available for purchase. For the purposes of this work, I experimented with 2mil films ($50.8\ \mu\text{m}$). See Fig. 6.12 for an example of what the kapton looks like when bonded to silicon.
- **Acrylic**, or poly(methyl methacrylate) (PMMA) is a transparent thermoplastic. Although it is safe to use in a laser cutter, the thinnest available sheets are $1/32''$ ($794\ \mu\text{m}$). This is too thick if trying to minimize weight, but could be useful as a spacer/shim in other applications.
- **Silica / Quartz** and **Borofloat** are both clear and flat. These materials come in standard 6" wafer formats and would be best prepared and diced to an appropriate size using cleanroom fabrication techniques. For more details on this process, see [3].
- **Glass coverslips** are clear and flat, but do not cut cleanly or all of the way through in a laser cutter. They are also difficult to score cleanly and to size using a diamond scribe. Standard thickness are either $170\ \mu\text{m}$ or $220\ \mu\text{m}$. I would recommend avoiding glass coverslips unless you have another cutting technique in mind.

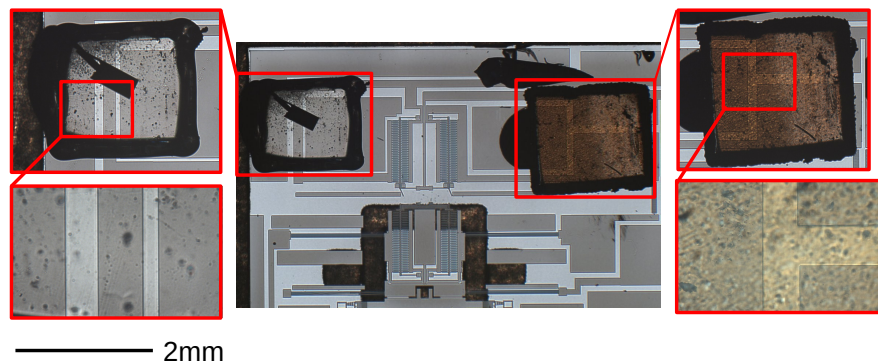


Figure 6.12: Left: 5mil mylar film flipchip bonded onto silicon. Right: 2mil kapton flipchip bonded onto silicon.

6.2.2.2 Cutting Method MEMS chips are small, often on the order of a few millimeters per side. At this size scale, there are a few options for cutting coverslips to size:

- **Laser Cutters** are becoming ubiquitous in many modern labs. I had success in cutting kapton and mylar films with a laser cutter, ¹⁸ after tuning the power settings to ensure the cut went all of the way through the plastic. Due to the small size of these cuts, be sure to leave a small tether to prevent coverslips from being cut completely away from the plastic sheeting. I also had success with attaching thin double-sided tape to one side of the plastic to prevent it from being blown away or becoming misaligned during the cutting process. The tape also prevents coverslips from floating away within the laser cutter bed after being cut. Tolerance test cuts are likely necessary to tune to the final desired dimensions. Free-form shapes and cutouts within a rectangle of plastic are possible. See Fig. 6.13 and Fig. 6.14 for example test cut results.

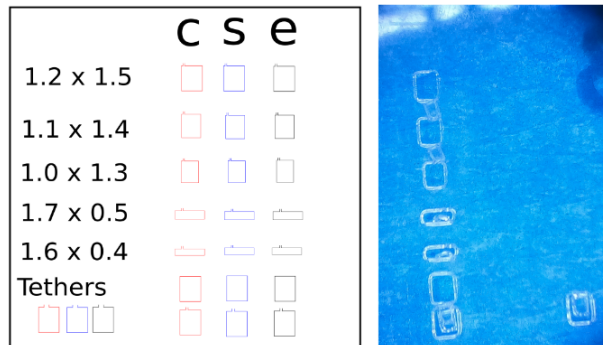


Figure 6.13: Left: Tolerance test cut patterns. “c”, “s”, and “e” refer to the laser cutter’s different cutting styles: vector cut (red), vector score (black), and raster engrave (blue). Right: Results of using the laser cutter with the tolerance cut patterns. Only the vector cut singulated coverslips entirely.

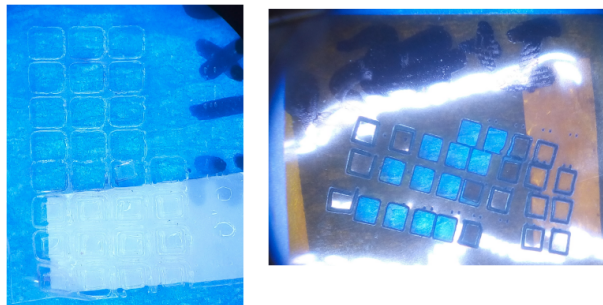


Figure 6.14: Double-sided tape helps to keep the plastic in place while the laser cutter and vacuum are on. It also helps to keep the coverslips from floating away after they’ve been cut. Left: 1.2 mm x 1.5 mm coverslips on 5mil mylar. Right: 1.2 mm x 1.5 mm coverslips on 2mil kapton.

- **Scissors** Works as usual. Use calipers to measure the final size, and be gentle when holding plastic coverslips with tweezers. Try marking shape sizes with a thin permanent marker. Marks can be removed with isopropyl alcohol. Note that the smallest size cover you will likely be capable of achieving is $\sim 1 \text{ mm} \times 1 \text{ mm}$.
- **Microfabrication - Dicing** Use a dicing tool to cut silica, quartz, or borofloat wafers to size.

¹⁸Universal Systems Laser Cutter (found in Jacobs Hall).

Square and rectangular shapes are easiest to cut; any other shape would require more effort.

6.2.2.3 Attach Method Once you've chosen the material and method, now is the time to choose how you will attach it to your substrate! Flipchip bonders primarily support thermocompression, the application of both temperature and pressure, to ensure a good bond. You can also forego the temperature and pressure, and just use the tool to precisely align two substrates. This technique lends itself well to other attachment methods, such as with UV cure epoxy.

- **UV cure epoxy** is a clear polymer that cures in a matter of seconds with the application of UV light. When using the flipchip bonder, bring the arm with the plastic cover down to rest on the silicon chip, apply and cure the glue, and then release the vacuum and bring the arm up again. The application of glue is entirely manual, so try using either a sewing needle or probe tip to apply glue to the corner of the coverslip and then shining a laser on the glue spots. Apply minimal force during this step to avoid damaging MEMS structures. There are also die bonders that have automated liquid dispensers, which could be useful to dispense a controlled amount of epoxy.

6.2.2.4 Flipchip Bonder Attach Tools Flipchip bonders, if used in an R&D setting, will likely support multiple sizes of vacuum pickup adapters. Some are specific to eutectic or thermocompressive bonding, and can optionally provide a pocket of inert gas to prevent oxidation during bonding. Others support the pick up of smaller components.

7 Lessons Learned and Protips

In no particular order.

- Iterate more often as opposed to getting all features working at once.
- Test with half-broken structures first so as to not break fully functional structures. Note that this will add additional overhead time to testing, since you have to test which structures are broken vs which aren't. It may be possible to determine which structures are broken via visual inspection, or electrically if they appear sane.
- Iterate on testing; try different materials, order of setup. For instance, if you want to test gluing coverslips over new portions of MEMS chip, try testing with a half-broken chip or be willing to sacrifice a fully functioning one.
- There's a higher likelihood of getting your designs included on someone else's run if you have designs ready to go and on-hand, at all times.
- Keep a L^AT_EX-ed (or otherwise neatly typeset) cheatsheet of commonly used formulas, constants, or derivations that you find yourself looking up or needing to re-derive often.
- Try to maintain digitally-created diagrams of your test setup for future reference and ease of inclusion into presentable materials.
- Keep a running inventory of all of your samples, if you think you'll use them for future experiments. Include details such as their position in sample carriers, whether they are mechanically functional, which processing steps they have done (e.g. wirebonding, gluing), any comments you have during testing, etc. This helps cut down on the amount of time you'll

need to re-remember which tests you ran on a specific chip X months ago. For an example of what an inventory spreadsheet might look like, refer to Fig. 7.1.

Boat	Position in Boat	Mechanically Working?	Wirebonded?	Coverslip?	Comments	Used?
May2017	1	N	Y		Crud over channel opening between funnel and left pawl; looks to be above channel? Broke bottom left pawl 2018-7-29; top left pawl already broken	(still have, 2019-4-26) Used on flexPCB; iteration 1 of experimental setup. All pawls still work? So just need to figure out a scheme to wirebond. A chunk of the bottom left GCA's spring is missing. Presumably it's the large polygon shape? Top left angled arm completely obliterated by probe tip (2019-5-3 used for electrical testing, in Faraday cage) Not glued to anything; used for 6.7um and 7.2um fiber testing. Initial tests with 7.2um fiber: was able to push fiber but it got stuck very often. Eventually at -90V the bottom right gap closer got stuck closed, so unstuck it with probes. Tried with 6.7um fiber and it didn't push whatsoever. Pawls didn't even seem to move forwards. Crunched majority of bottom left GCA trace. Tried wirebonding to fix trace, ended up lifting off majority of trace. Wirebonded across channel; carbon fiber stuck in channel. Was having parasitic issues but seems fixed with grounding of substrate. Lots of debris and shrapnel.
May2017	3	3/4/2018 (bottom left trace completely gone)	Y		Exploratory, 2018-6-20. Will need to break vernier. Hopefully this doesn't also result in death of wirebonds?	
May2017	4		3/4 N		top right quadrant of GCA not working. Tried using 3 good probes and still no bueno. -> might be because of one probe not electrically connected properly (HV2). Try using other HV2 probe, instead.	(2019-4-22 Given to Kris as a showpiece for showing to NASA people.) Might actually work?
Sept2017	1	N (2018-6-19) top left pawl smashed; bottom left GCA non-functional (stuck on CF?)	Y (2018-6-12)		Used different probe and HV2 worked; all 4 GCAs working	(still have, 2019-4-26) Use for iteration 2 of experimental setup. Fiber stuck under bottom left pawl when trying to operate at 70V? Tried to pull pawl off using probe tip, but accidentally broke top left pawl instead. CF still stuck in channel; might be good to SEM this. Officially broken. Was unable to get resistance readings. Vernier broken.
Sept2017	2	N?	Y (2018-7-8)		No problems; just tested the two halves of the GCA array (top and bottom) separately	(still have, 2019-4-26) Salt water splashed over left half of GCA during LCR meter testing. Bond pads look shorted; or they could just be covered in salt. Try scraping it off, blasting with air gun, putting in water and hot-plating, etc to clean and maybe it will still work?
Sept2017	3	Y	Y (2018-7-26)			(still have, 2019-4-26) Pushes into agar. 7/28, potentially. 7/29, definitively.
Sept2017	4	Y	N		Check 2019-2-1; all pawls intact; vernier intact; all four beams intact	(still have, 2019-4-26)

Figure 7.1: Example inventory of one set of chips.

- When taking screenshots of layouts in KLayout for design review, publication, or other uses¹⁹, you can increase the resolution and visibility:
 - Use oversampling. File > Setup > Display > General > Oversampling. I like to use 2X or 3X oversampling for the highest quality. This helps especially for the finger arrays, which would otherwise appear as solid blocks of color. When editing, you'll probably want to stick with No oversampling for faster rendering speed.
 - Change the stipple (texture) of the layers. To do this, select the layer of interest in the right-hand window, then Layer Toolbox > Stipple. I like to use the solid stipple for the SOI, SOIHOLE, and METAL layers, and a hatched stipple for the TRENCH and NOTRENCH layers. Feel free to choose stipples that suit your image!
 - To make your layout appear fullsize on the screen: F2. Use either your computer's built-in snipping tool or KLayout's screenshot editor to take an image of the scale bar and layout: File > Screenshot or just Print.
- The wirebonder microscope is surprisingly good. You can capture digital images by holding your phone up to the viewport at just the right angle. Fig. 3.18 was taken through the wirebonder microscope viewport.

¹⁹On that note, try to show cartoons as opposed to full-on layouts during group meeting unless it's a design review

- Imaging MEMS can be very difficult.²⁰ The size scale, lighting, and focus will take a while to get right. Think about how you will image your setup as proof that your experiment worked, before running the experiment. For example, always leave the video feed running on the microscope (while you're experimenting) in case something interesting happens. Take pictures - with your phone, the microscope view port, etc - during the assembly process so you can see when things go wrong.
- Use version control for your layouts. Even though version control doesn't diff binaries very well, it's still a good idea to track your work more discretely. Upload your design docs somewhere, too.
- Try using a citation manager. It makes writing reports (like this one) much more manageable. For example, Mendeley has a great Google Chrome browser plugin that makes capturing and syncing new articles super easy.²¹
- Time tracking tools (such as Toggl) can be useful.²²
- With enough perseverance, any of your ideas (or Kris's) are probably possible.

8 Future Directions

- Parallelize the fiber pusher for insertion into biological tissues, and package it to be biocompatible.
- Test whether anti-aliasing of control signals is actually necessary for the fiber pusher. There is no return spring pulling the fiber back as in many other electrostatic motor applications.
- Experimentally test the lower and upper limits on the operating frequency for the fiber pusher application.
- Test the maximum pull-in voltage that the motors can withstand before becoming stuck
- Optimize the fiber pusher for integration with a solar sail or silicon MEMS fin for aerodynamic control.

9 Conclusion

This thesis presented a MEMS mechanism for actuating (pushing/pulling) carbon fibers, unlocking applications in neural recording, arbitrary movement of microrobots in free space, and beyond.

Recent work has demonstrated precise, depth-controllable mechanisms for the insertion of single neural recording electrodes, but these methods are mostly only capable of inserting electrodes which elicit adverse biological response. In this work, we presented an electrostatic-based actuator capable of inserting individual carbon fiber microelectrodes which elicit minimal to no adverse biological response. This technique provides a platform generalizable to many microwire-style recording electrodes.

²⁰For reference, our group uses a Canon EOS 7D camera body, EF-S 18-135mm f/3.5-5.6 IS Standard Zoom Lens, and Canon EF 180mm f/3.5L Macro USM Lens, tripod, and tabletop studio lighting light tent kit.

²¹Thanks to **Mauricio Bustamante** for introducing this to me.

²²Thanks to **Joseph Greenspun** for introducing this to me.

This thesis also discussed a second high-level application of fiber pushing microrobots. While previous work focused on jumping [4], flying [5], and walking microrobots [2], an interesting class of microrobots that hasn't been actively explored are microrobots that create the surface on which they move. This work discussed the mass and power budget requirements for an integrated system which combines an actuator, controller, and power supply. We also introduced specific thoughts for integration and hand-assembly, as well as high-level concept ideas for how the robot could ascend and descend along an arbitrary length of material.

The future of microrobots lies in their ability to interact with the world in increasingly complex, abstract ways. Fiber pushing microrobots have the potential to change how we interact with moving materials at the micro-scale.

10 References

References

- [1] A. Lecomte, E. Descamps, and C. Bergaud, "A review on mechanical considerations for chronically-implanted neural probes," *J. Neural Eng.*, vol. 15, 2017.
- [2] D. Contreras, "Walking Silicon: Actuators and Legs for Small-Scale Terrestrial Robots," Ph.D. dissertation, 2018.
- [3] O. Chen, M. M. Maharbiz, and S. Member, "Hydrogel-actuated carbon fiber neural probes," *NER; International IEEE EMBS Conference on Neural Engineering*, 2019.
- [4] J. T. Greenspun and K. S. Pister, "Low voltage actuation of high force electrostatic latches," in *2017 19th Int. Conf. Solid-State Sensors, Actuators Microsystems*. IEEE, Jun 2017, pp. 898–901.
- [5] D. S. Drew, N. O. Lambert, C. B. Schindler, and K. S. J. Pister, "Toward Controlled Flight of the Ionocraft: A Flying Microrobot Using Electrohydrodynamic Thrust With Onboard Sensing and No Moving Parts," *IEEE Robotics and Automation Letters*, vol. 3, no. 4, pp. 2807–2813, 2018. [Online]. Available: <https://ieeexplore.ieee.org/document/8373697/>
- [6] S. Venkatraman, "Serial Assembly of Microstructures," Ph.D. dissertation, 2006.
- [7] S. L. BeMent, K. D. Wise, D. J. Anderson, K. Najafi, and K. L. Drake, "Solid-State Electrodes for Multichannel Multiplexed Intracortical Neuronal Recording," *IEEE Trans. Biomed. Eng.*, vol. BME-33, no. 2, pp. 230–241, 1986.
- [8] P. R. Patel, H. Zhang, M. T. Robbins, J. B. Nofar, S. P. Marshall, M. J. Kobylarek, T. D. Y. Kozai, N. A. Kotov, and C. A. Chestek, "Chronic in vivo stability assessment of carbon fiber microelectrode arrays," *J. Neural Eng.*, vol. 13, no. 6, p. 066002, Dec 2016.
- [9] T. L. Massey, S. R. Santacruz, J. F. Hou, K. S. J. Pister, J. M. Carmena, and M. Michel, "A high-density carbon fiber neural recording array technology," *bioRxiv*, 2018.
- [10] J. J. Jun, N. A. Steinmetz, J. H. Siegle, D. J. Denman, M. Bauza, B. Barbarits, A. K. Lee, C. A. Anastassiou, A. Andrei, Ç. Aydın *et al.*, "Fully integrated silicon probes for high-density recording of neural activity," *Nature*, vol. 551, no. 7679, p. 232, 2017.

- [11] P. J. Rousche and R. A. Normann, “Chronic recording capability of the utah intracortical electrode array in cat sensory cortex,” *J. Neurosci. Methods*, vol. 82, no. 1, pp. 1–15, 1998.
- [12] M. A. Nicolelis, D. Dimitrov, J. M. Carmena, R. Crist, G. Lehew, J. D. Kralik, and S. P. Wise, “Chronic, multisite, multielectrode recordings in macaque monkeys,” *Proceedings of the National Academy of Sciences*, vol. 100, no. 19, pp. 11 041–11 046, 2003.
- [13] W. M. Reichert, *Indwelling neural implants: strategies for contending with the in vivo environment*. CRC Press, 2007.
- [14] T. D. Yoshida Kozai, N. B. Langhals, P. R. Patel, X. Deng, H. Zhang, K. L. Smith, J. Lahann, N. A. Kotov, and D. R. Kipke, “Ultrasmall implantable composite microelectrodes with bioactive surfaces for chronic neural interfaces,” *Nat. Mater.*, vol. 11, no. 12, pp. 1065–1073, 2012.
- [15] J. J. Clark, S. G. Sandberg, M. J. Wanat, J. O. Gan, E. A. Horne, A. S. Hart, C. A. Akers, J. G. Parker, I. Willuhn, V. Martinez *et al.*, “Chronic microsensors for longitudinal, subsecond dopamine detection in behaving animals,” *Nature Methods*, vol. 7, no. 2, pp. 126–129, 2010.
- [16] S. F. Bernatchez, P. J. Parks, and D. F. Gibbons, “Interaction of macrophages with fibrous materials in vitro,” *Biomaterials*, vol. 17, no. 21, pp. 2077–2086, 1996.
- [17] J. P. Seymour and D. R. Kipke, “Neural probe design for reduced tissue encapsulation in cns,” *Biomaterials*, vol. 28, no. 25, pp. 3594–3607, 2007.
- [18] P. R. Patel, K. Na, H. Zhang, T. D. Kozai, N. A. Kotov, E. Yoon, and C. A. Chestek, “Insertion of linear 8.4 μm diameter 16 channel carbon fiber electrode arrays for single unit recordings,” *J. Neural Eng.*, vol. 12, no. 4, p. 46009, 2015.
- [19] G. Guitchounts, J. E. Markowitz, W. A. Liberti, and T. J. Gardner, “A carbon-fiber electrode array for long-term neural recording,” *J. Neural Eng.*, vol. 10, no. 4, 2013.
- [20] W. F. Gillis, C. A. Lissandrello, J. Shen, B. W. Pearre, A. Mertiri, F. Deku, S. Cogan, B. J. Holinski, D. J. Chew, A. E. White, T. J. Gardner, and T. M. Otchy, “Carbon Fiber On Polyimide Ultra-Microelectrodes,” *J. Neural Eng.*, vol. 15, 2018.
- [21] J. Feingold, T. M. Desrochers, N. Fujii, R. Harlan, P. L. Tierney, H. Shimazu, K.-i. Amemori, A. M. Graybiel, H. Shimazu, K. Amemori, and G. Am, “A system for recording neural activity chronically and simultaneously from multiple cortical and subcortical regions in nonhuman primates,” *J. Neurophysiol.*, vol. 107, no. 7, pp. 1979–1995, 2012.
- [22] J. Muthuswamy, M. Okandan, T. Jain, and A. Gilletti, “Electrostatic microactuators for precise positioning of neural microelectrodes,” *IEEE Trans. Biomed. Eng.*, vol. 52, no. 10, pp. 1748–1755, 2005.
- [23] J. Muthuswamy, M. Okandan, A. Gilletti, M. S. Baker, and T. Jain, “An array of microactuated microelectrodes for monitoring single-neuronal activity in rodents,” *IEEE Trans. Biomed. Eng.*, vol. 52, no. 8, pp. 1470–1477, 2005.
- [24] A. Andrei, M. Welkenhuysen, B. Nuttin, and W. Eberle, “A response surface model predicting the in vivo insertion behavior of micromachined neural implants,” *Journal of Neural Engineering*, vol. 9, no. 1, p. 016005, feb 2012. [Online]. Available: <http://stacks.iop.org/1741-2552/9/i=1/a=016005?key=crossref.60aefa04fa76454b7c9ed6f29c773305>

- [25] W. Jensen, U. Hofmann, and K. Yoshida, "Assessment of subdural insertion force of single-tine microelectrodes in rat cerebral cortex," *Proceedings of the 25th Annual International Conference of the IEEE Engineering in Medicine and Biology Society (IEEE Cat. No.03CH37439)*, no. June 2014, pp. 2168–2171, 2003. [Online]. Available: <http://ieeexplore.ieee.org/document/1280170/>
- [26] M. A. Howard, B. A. Abkes, M. C. Ollendieck, M. D. Noh, R. C. Ritter, and G. T. Gillies, "Measurement of the force required to move a neurosurgical probe through in vivo human brain tissue," *IEEE Transactions on Biomedical Engineering*, vol. 46, no. 7, pp. 891–894, 1999.
- [27] C. Tian and J. He, "Monitoring Insertion Force and Electrode Impedance during Implantation of Microwire Electrodes." *Conference proceedings : ... Annual International Conference of the IEEE Engineering in Medicine and Biology Society. IEEE Engineering in Medicine and Biology Society. Conference*, vol. 7, pp. 7333–6, 2005. [Online]. Available: <http://www.ncbi.nlm.nih.gov/pubmed/17281974>
- [28] N. H. Hosseini, R. Hoffmann, S. Kisban, T. Stieglitz, O. Paul, and P. Ruther, "Comparative study on the insertion behavior of cerebral microprobes," *Annual International Conference of the IEEE Engineering in Medicine and Biology - Proceedings*, no. c, pp. 4711–4714, 2007.
- [29] F. Vitale, D. G. Vercosa, A. V. Rodriguez, S. S. Pamulapati, F. Seibt, E. Lewis, J. S. Yan, K. Badhiwala, M. Adnan, G. Royer-Carfagni, M. Beierlein, C. Kemere, M. Pasquali, and J. T. Robinson, "Fluidic Microactuation of Flexible Electrodes for Neural Recording," *Nano Lett.*, vol. 18, no. 1, pp. 326–335, Jan 2018.
- [30] H. J. P. Reitboeck, "A 19-Channel Matrix Drive with Individually Controllable Fiber Microelectrodes for Neurophysiological Applications," *IEEE Trans. Syst. Man Cybern.*, vol. SMC-13, no. 5, pp. 676–683, 1983.
- [31] S. Qiao, K. A. Brown, A. L. Orsborn, B. Ferrentino, and B. Pesaran, "Development of semi-chronic microdrive system for large-scale circuit mapping in macaque mesolimbic and basal ganglia systems," in *2016 IEEE 38th Annual International Conference of the Engineering in Medicine and Biology Society (EMBC)*. IEEE, 2016, pp. 5825–5828.
- [32] T. M. Otchy and B. P. Ölveczky, "Design and assembly of an ultra-light motorized microdrive for chronic neural recordings in small animals," *J. Vis. Exp.*, no. 69, Nov 2012.
- [33] M. Fee and A. Leonardo, "Miniature motorized microdrive and commutator system for chronic neural recording in small animals," *J. Neurosci. Methods*, pp. 83–94, 2001.
- [34] N. Jackson, A. Sridharan, S. Anand, M. Baker, M. Okandan, and J. Muthuswamy, "Long-Term Neural Recordings Using MEMS Based Movable Microelectrodes in the Brain." *Front. Neuroeng.*, vol. 3, no. June, p. 10, 2010.
- [35] M. Welkenhuysen, A. Andrei, L. Ameye, W. Eberle, and B. Nuttin, "Effect of insertion speed on tissue response and insertion mechanics of a chronically implanted silicon-based neural probe," *IEEE Trans. Biomed. Eng.*, vol. 58, no. 11, pp. 3250–3259, 2011.
- [36] I. Penskiy and S. Bergbreiter, "Optimized electrostatic inchworm motors using a flexible driving arm," *J. Micromechanics Microengineering*, vol. 23, no. 1, 2012.
- [37] C. B. Schindler, D. S. Contreras, J. Greenspun, and K. S. J. Pister, "An Electrostatic MEMS Filament Micromanipulator for Microrobots," *Int. Conf. Manip. Autom. Robot. Small Scales*, pp. 7–9, 2017.

- [38] R. Yeh, S. Hollar, and K. S. Pister, “Single mask, large force, and large displacement electrostatic linear inchworm motors,” *J. Microelectromechanical Syst.*, vol. 11, no. 4, pp. 330–336, 2002.
- [39] D. S. Contreras and K. S. J. Pister, “Dynamics of Electrostatic Inchworm Motors for Silicon Microrobots,” *Int. Conf. Manip. Autom. Robot. Small Scales*, 2017.
- [40] R. Deepthi, R. Bhargavi, K. Jagadeesh, and M. S. Vijaya, “Rheometric Studies on Agarose Gel- A Brain Mimic Material,” *SASTech*, vol. 9, no. 2, pp. 27–30, 2010.
- [41] L. Luan, X. Wei, Z. Zhao, J. J. Siegel, O. Potnis, C. A. Tuppen, S. Lin, S. Kazmi, R. A. Fowler, S. Holloway, A. K. Dunn, R. A. Chitwood, and C. Xie, “Ultraflexible nanoelectronic probes form reliable, glial scarfree neural integration,” *Sci. Adv.*, vol. 3, no. 2, pp. 1–10, 2017.
- [42] D. R. Sparta, A. M. Stamatakis, J. L. Phillips, N. Hovelsø, R. van Zessen, and G. D. Stuber, “Construction of implantable optical fibers for long-term optogenetic manipulation of neural circuits,” *Nat. Protoc.*, vol. 7, no. 1, pp. 12–23, Dec 2011.
- [43] B. Pesaran, M. Vinck, G. T. Einevoll, A. Sirota, P. Fries, and M. Siegel, “Investigating large-scale brain dynamics using field potential recordings : Analysis and interpretation,” *Nature Neuroscience*, 2018. [Online]. Available: <http://dx.doi.org/10.1038/s41593-018-0171-8>
- [44] G. Paxinos and C. Watson, *The rat brain in stereotaxic coordinates*.
- [45] A. L. Orsborn, C. Wang, K. Chiang, M. M. Maharbiz, J. Viventi, and B. Pesaran, “Semi-chronic chamber system for simultaneous subdural electrocorticography, local field potentials, and spike recordings,” *International IEEE/EMBS Conference on Neural Engineering, NER*, vol. 2015-July, pp. 398–401, 2015.
- [46] “Watch This Robot Crawl on a High-Voltage Power Line - IEEE Spectrum.” [Online]. Available: <https://spectrum.ieee.org/autamaton/robotics/industrial-robots/explainer-robot-inspects-high-voltage-lines>
- [47] F. Maksimovic, B. Wheeler, D. C. Burnett, O. Khan, S. Mesri, I. Suci, A. Moreno, A. Sundararajan, B. Zhou, R. Zoll, A. Ng, T. Chang, X. Villajosana, T. Watteyne, A. Niknejad, K. S. J. Pister, E. Engineering, and C. Sciences, “A Crystal-Free Single-Chip Micro Mote with Integrated 802 . 15 . 4 Compatible Transceiver , sub-mW BLE Compatible Beacon Transmitter , and Cortex M0 Cortex M0,” in *Symposia on VLSI Technology and Circuits*, 2019, p. 2.
- [48] B. G. Kilberg, D. S. Contreras, J. Greenspun, and K. S. Pister, “MEMS aerodynamic control surfaces for millimeter-scale rockets,” *International Conference on Manipulation, Automation and Robotics at Small Scales, MARSS 2017 - Proceedings*, pp. 1–5, 2017.
- [49] R. S. Zoll, C. B. Schindler, T. L. Massey, D. S. Drew, M. M. Maharbiz, and K. S. J. Pister, “MEMS-Actuated Carbon Fiber Microelectrode for Neural Recording,” *IEEE Transactions on NanoBioscience*, vol. 18, no. 2, pp. 234–239, 2019.
- [50] “ALIGNER WAFER BONDER AML - AWB: TECHNICAL SPECIFICATION,” Tech. Rep. [Online]. Available: http://aml.co.uk/files/7214/4309/0847/AML_{_}FLyerSept15.pdf
- [51] D. S. Contreras and K. S. Pister, “Durability of silicon pin-joints for microrobotics,” *2016 International Conference on Manipulation, Automation and Robotics at Small Scales, MARSS 2016*, pp. 1–6, 2016.

- [52] C. Schindler, J. Greenspun, H. Gomez, and K. S. J. Pister, “A Jumping Silicon Microrobot with Electrostatic Inchworm Motors and Energy Storing Substrate Springs,” in *20th International Conference on Solid-State Sensors, Actuators and Microsystems*, 2019.

11 Appendix

11.1 Arduino Code and Waveforms

The code ²³ below produces the waveforms as shown in Fig. 11.1.

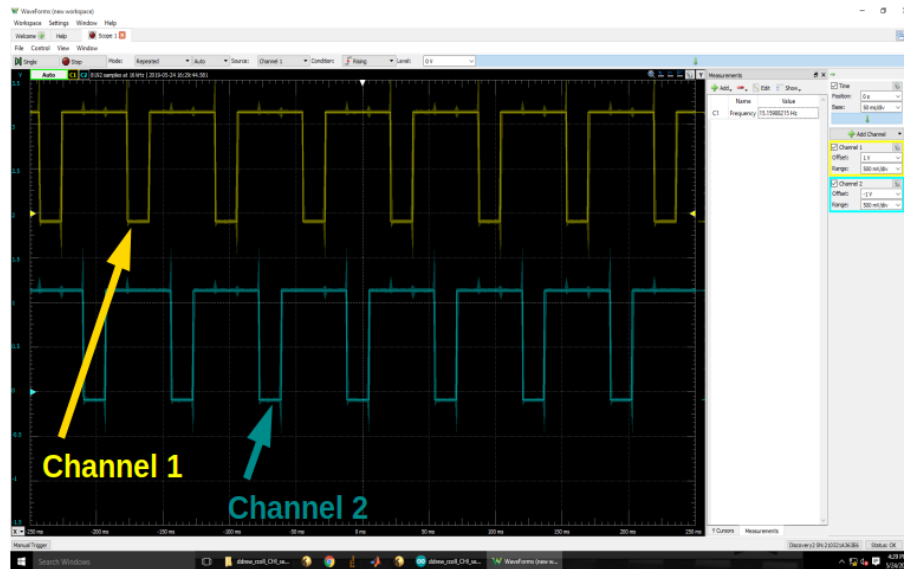


Figure 11.1: Waveforms produced by the arduino code. Note the anti-phase between Channel 1 and Channel 2, which have a frequency of 15 Hz.

```
// arduino digital output switch labels
// D1 and D2 -> vertical swing motor
int D1 = 2;
int D2 = 3;

int strokeFrequency;
int strokeNumber;
int extensionRatio;
int totalStrokes;

int tstart = 1000;

//initialize outputs and start initial delayMicroseconds
void setup() {
  Serial.begin(9600);
  pinMode(D1, OUTPUT);
  pinMode(D2, OUTPUT);

  releaseMotors(D1,D2);
  delayMicroseconds(tstart);
}
```

²³Thanks to **Daniel Contreras** and **Daniel Drew** for sharing this code template.

```

}

//run through steps after initial delayMicroseconds
void loop() {

    strokeFrequency = 2000; // NOTE: change this to set the frequency
    totalStrokes = 0;
    int cycleDelay = 1000/strokeFrequency;

    engageMotors(D1,D2);

    doStrokeForever(cycleDelay); // run indefinitely

    for(int i = 0; i<totalStrokes; i++){ // run for totalStrokes
        doStroke(totalStrokes , cycleDelay);
    }

    releaseMotors(D1,D2);
}

void doStroke(int cycles , int innerDelay){
    for(int i=0; i < cycles; i++)
    {
        delayMicroseconds(innerDelay);
        digitalWrite(D1, 1);
        delayMicroseconds(innerDelay);
        digitalWrite(D1, 0);
        delayMicroseconds(innerDelay);
        digitalWrite(D2, 1);
        delayMicroseconds(innerDelay);
        digitalWrite(D2, 0);
    }
}

void doStrokeForever(int innerDelay){
    while(true)
    {
        delayMicroseconds(innerDelay);
        digitalWrite(D1, 1);
        delayMicroseconds(innerDelay);
        digitalWrite(D1, 0);
        delayMicroseconds(innerDelay);
        digitalWrite(D2, 1);
        delayMicroseconds(innerDelay);
        digitalWrite(D2, 0);
    }
}

void releaseMotors(int D1, int D2){
    digitalWrite(D1, 1);
    digitalWrite(D2, 1);
    //delayMicroseconds(stroke_reset);
}

void engageMotors(int D1, int D2){
    digitalWrite(D1, 0);
    digitalWrite(D2, 0);
    // delayMicroseconds(stroke_reset);
}

```

11.2 LCR Impedance Measurements

11.2.1 Keysight Data Collection Automation ²⁴

```
measure_zpec.m

%% establish connection

AVG = 4;
FREQ = logspace(2,6,41);

%open connection
% fObj = ZmeterGPIB;
fprintf(fObj, 'VOLT_1 ');
fprintf(fObj, 'APER_MED ');
fprintf(fObj, 'AMPL:ALC_OFF ');
fprintf(fObj, 'DISP:PAGE_MEAS '); %Display Format

% select current electrode pair

data = Zmeas(AVG, FREQ, fObj); %Store and transfer data
% plot the data
mag = squeeze(data(:,1,:));
ang = squeeze(data(:,2,:));
% ang(mag>1e10)=nan;
% mag(mag>1e10)=nan;

% magerr = ssatdev(mag)/sqrt(AVG);
% angerr = stdev(ang)/sqrt(AVG);
%% plot
subplot(211);
loglog(FREQ, mean(mag,2));
hold on;
xlabel('Frequency [Hz] ');
ylabel('|Z| [\Omega] ');
xlim([FREQ(1) FREQ(end)])

subplot(212);
semilogx(FREQ, mean(ang,2));
hold on;
ax=gca;
axis([1e2 FREQ(end) -180 90]);
ax.YTick = -180:45:180;
ylabel('\angle Z [deg] ');
xlabel('Frequency [Hz] ');

% close the connection
% ZmeterClose(fObj);
% clear fObj;
```

Zmeas.m

```
function data = Zmeas( AVG, FREQ, fObj )
%UNTITLED5 Summary of this function goes here
% Detailed explanation goes here

fprintf(fObj, 'DISP:PAGE_MEAS ');
```

²⁴Thanks to **Tom Zajdel** for sharing this code and teaching me how to use it.

```

for i = 1:length(FREQ)
    % START FREQ
    for j = 1:AVG
        fprintf(fObj, sprintf('FREQ_%8f',FREQ(i)));
    %     pause(0.1);
    %     fprintf(fObj, 'FUNC:IMP_RX'); %change function
        fprintf(fObj, 'TRIG:SOUR_BUS');
        fprintf(fObj, 'ABOR');
        fprintf(fObj, 'INIT:CONT_ON');
        fprintf(fObj, 'TRIG:IMM');
        fprintf(fObj, 'FETC?');
        tmp = fscanf(fObj);
        stmp = str2num(tmp);
        tmp = stmp(1:2);
        data(i, :, j) = tmp;
    %     fprintf('Reading: %d/%d', j, AVG);
    end
end

end

```

ZmeterGPIB.m

```

function fObj = ZmeterGPIB()
%% Interface configuration and instrument connection
vinfo = instrhwinfo('gpib', 'agilent');
%
% create a VISA-USB object corresponding to the scope. The value of i may
% be adjusted accordingly
i = 1;
fObj = eval(vinfo.ObjectConstructorName{i});

% Create a GPIB object.
% fObj = instrfind('Type', 'gpib', 'BoardIndex', 0, 'PrimaryAddress', 17, 'Tag', '');
%
% Create the GPIB object if it does not exist
% otherwise use the object that was found.
% if isempty(fObj)
%     fObj = gpib('AGILENT', 7, 17);
% else
%     fclose(fObj);
%     fObj = fObj(1);
% end

% Open the connection
fopen(fObj);

end

```

Zmeter_init.m

```

fObj = ZmeterGPIB;
fprintf(fObj, 'FUNC:IMP_ZTD');

```

11.2.2 MATLAB plotting

Used to generate this figure: [Fig. 3.27](#).

plot_LCR_2Dscatter.m

```

% Combine plots across operating voltages, number of pawls touching,
% variance and std-dev of each measurement based on the averaging

close all;
clear;

%set(groot, 'DefaultAxesColorOrder', flipud(parula(7)))

set_figure_style_pre(2);

num_pawls = [2,3];

%extract_all = sprintf('*pawls.mat')
N = length(num_pawls);
for j=1:N
    figure
    %     pu = get(gcf, 'PaperUnits');
    %     pp = get(gcf, 'PaperPosition');
    %     set(gcf, 'Units', pu, 'Position', pp);
    extract_str = sprintf('%dpawls.mat', num_pawls(j))
    %% load n-pawl data
    files = dir(fullfile('../2018-7-11_impedance_measurements', extract_str))
    %files = dir(fullfile('../2018-7-11_impedance_measurements', extract_all))

    L = length(files);

    FREQ = logspace(2,6,41);

    for i=1:L
        file=files(i).name;
        filepath = fullfile('../2018-7-11_impedance_measurements', file )

        load_data = load(filepath);
        data = load_data.data;

        % extract voltage from filename
        voltage = extractAfter(filepath, 'May2017-3-');
        voltage = extractBetween(voltage, 1, 3)
        voltage = voltage{1};

        %% collate data
        mag = squeeze(data(:,1,:)); % contains 4-pts from each frequency measured
        ang = squeeze(data(:,2,:));

        %% plot

        subplot(211);
        colormap(jet);
        loglog(FREQ, mean(mag,2)/1e6, '.', 'MarkerSize', 20);
        hold on;
        title_str = sprintf('Electrode_Impedance', num_pawls(j))
        %title(title_str)
        %xlabel('Frequency [Hz]')
        ylabel('|Z| [M\Omega]')%, 'FontSize',20,'FontName', 'Times_New_Roman')
        % xlim([FREQ(1) FREQ(end)])
        xlim([FREQ(1) 1e4]) % match Travis's axes, except mine doesn't go down to 10^0
        ylim([1e-1 1e1])
    end
end

```

```

subplot(212);
colormap(jet);
semilogx(FREQ,mean(ang,2), '.', 'MarkerSize', 20);
hold on;
ax=gca;
axis([1e2 FREQ(end) -180 90])
ax.YTick = -180:45:180;
%title_str = sprintf('Electrode_Impedance_Phase', num_pawls(j))
%title({'';title_str})
ylabel('\angle_Z[deg]')%, 'FontSize',20,'FontName', 'Times_New_Roman')
xlabel('Frequency[Hz]')%, 'FontSize',20,'FontName', 'Times_New_Roman')
% xlim([FREQ(1) FREQ(end)])
xlim([FREQ(1) 1e4]) % match Travis's axes, except mine doesn't go down to 10^0
ylim([-100 0])

voltage = sprintf('%s', voltage)
legendInfo{i} = [voltage];

end
legend(legendInfo, 'Location', 'southoutside', 'Orientation', 'horizontal')%

% Set plot style, export
set_figure_style(2);
resize_figure(2,1);
str = sprintf('Impedance-vs-freq-%dpawls', num_pawls(j))
export_figure(str, 'eps')
end

```

11.3 Weight and Force Estimates, Inchworm Pusher

Used to generate Table 6.

static_friction.m

```

%% Experimentally calculate coefficient of static friction
angles = [38 25 32 40 25 45];
angle = mean(angles);
mu_s_glass_silicon = tand(angle)

mass_silicon = 22e-3; % 22mg for giraffe chip
g = 9.81 % m/s^2

f_motor = mu_s_glass_silicon*mass_silicon*g

%% Calculate mass empirically
rho_silicon = 2.32; % g/cm^3
area = 0.45*0.35; %cm^2
t_mems = 0.059; % 590um = 0.59mm = 0.059cm
volume = area*t_mems;
mass_silicon_analytical = rho_silicon*volume; % 22mg, same as scale val

%% Weight of coverslip
rho_mylar = 1.38; % g/cm^3
area_mylar = 0.1*0.2; %cm^2
t_mylar = 0.0127; % mm
mass_mylar = rho_mylar*area_mylar*t_mylar

%% Calculate constituent
t_ic = 0.03 % 300um IC thickness estimate from Brad

```

```
% Example calculation for optimized fiber pusher
length_cm = 0.3 % cm
width_cm = 0.24 % cm
mass_kg = t_mems*length_cm*width_cm*rho_silicon/1000 % mass in kg
f_reqd_uN = mu_s_glass_silicon*mass_kg*g*1e6
```